Applied Catalysis B: Environmental 230 (2018) 269–303

Contents lists available at ScienceDirect

Applied Catalysis B: Environmental

journal homepage: www.elsevier.com/locate/apcatb

Review

Photonic crystal-assisted visible light activated TiO_2 photocatalysis

Vlassis Likodimos

Section of Solid State Physics, Department of Physics, National and Kapodistrian University of Athens, Panepistimiopolis, 15 784, Greece

ARTICLE INFO

Keywords:
Titanium dioxide
Semiconductor photocatalysis
Photonic crystals
Slow photons
Visible light

ABSTRACT

Photonic crystals have been established as unique periodic structures to promote photon capture and control over light-matter interactions. Their application in semiconductor, mainly TiO_2, photocatalysis has emerged as a promising structural modification to boost light harvesting of photocatalytic materials by means of slow photons i.e. light propagation at reduced group velocity near the edges of the photonic band gap (PBG). In this review, the latest advances in the development of TiO_2 photonic crystal photocatalysts are highlighted, targeting primarily on the design, fabrication, structure-activity and performance evaluation of visible light activated (VLA) TiO_2 inverse opals in the degradation of water and air pollutants as well as water splitting. Up to date work demonstrating the amplification effect of PBG engineered photonic crystals on the photocatalytic and photoelectrochemical performance under UV excitation is accordingly presented. Recent developments on the combination of enhanced light trapping, mainly via slow photons, mass transport and adsorption of macro/mesoporous inverse opals with targeted compositional and electronic modifications currently pursued to promote charge separation and visible light activation, i.e. dye sensitization, non-metal and self-doping, coupling with metallic nanoparticles and plasmonic effects, heterostructuring with narrow band gap semiconductors, quantum dots and graphene as well as the use of alternative metal oxide photocatalysts beyond TiO_2 are thoroughly reviewed with respect to their potential for key improvements of the photocatalytic efficiency under visible light. Pertinent challenges and future prospects in photonic crystal-assisted VLA photocatalysts are addressed aimed at advanced photon management routes that could step up photocatalytic applications.

1. Introduction

Semiconductor and especially titanium dioxide-titania (TiO_2) photocatalysis has been attracting enormous interest as one of the most promising technologies to address global concerns over environmental pollution and meet the ever increasing energy demands by the utilization of naturally abundant, renewable sources such as solar light [1,2]. Specifically, heterogeneous TiO_2 photocatalysis has spawned a great amount of multidiscipline research as a versatile and clean technology for solar-to-chemical-energy conversion applications ranging from sustainable water and air purification [3,4] to hydrogen and chemical fuels' production by water splitting and CO_2 reduction [5] relying on environmentally benign materials and solar energy, as a standalone process or in combination with other advanced technologies [6,7]. This distinctive potential for solar powered technologies has spurred the development of TiO_2 nanomaterials with tailored structural, morphological and optoelectronic properties [8] that could effectively evade the two major limitations of the process efficiency, namely the low quantum efficiency arising from the recombination of photogenerated charge carriers (electrons and holes) [9,10] and the poor solar light harvesting resulting from the wide band gap (3.0–3.2 eV) of most titania's polymorphic phases [11].

Two key research directions are currently pursued to alleviate these detrimental effects that impair practical photocatalytic applications: those related to "extrinsic" modifications of the TiO_2 electronic properties [12], the most prominent being non-metal doping [11,13] coupling with noble metal nanoparticles (NPs) (plasmonic photocatalysis) [14,15] and heterostructuring with narrower band gap semiconductors [16,17] or carbon nanomaterials [18,19], and those relying on "self-structural" modifications of TiO_2 nanomaterials [20] that mainly involve tailoring titania's structural and morphological characteristics including phase composition, crystallinity, texture, size and shape, synergistic interfacial effects between polymorphic TiO_2 phases [21–23], as well as surface [24,25] and facet [26] engineering. As to light harvesting, (co)-doping by non-metal heteroatoms (N, C, S, P, F) [12,27], self-doping induced by hydrogenation ("black" TiO_{2-x}) [28,29] and surface modification by molecular-scale transition metal oxide nanoclusters [17,30], which effectively reduce titania's band gap via intragap states, along with the utilization of localized surface plasmon resonance of noble metal NPs [31] have been intensively pursued as the most potent approaches for the development of visible light-activated (VLA) photocatalysts [32]. Significant progress has been accordingly

E-mail address: vlikodimos@phys.uoa.gr.

https://doi.org/10.1016/j.apcatb.2018.02.039
Received 7 November 2017; Received in revised form 5 February 2018; Accepted 17 February 2018
Available online 18 February 2018
0926-3373/ © 2018 Elsevier B.V. All rights reserved.

achieved in enhancing titania's visible light photocatalytic activity, though, in several cases, at the expense of the overall photocatalytic efficiency under solar light [33]. In particular, titania's modification by lattice or surface defects that lead to effectively narrower band gap may compromise the photocatalysts' reactivity and the associated process efficiency by decreasing the thermodynamic driving force between photogenerated electron and holes [6]. Application of selected scavengers allowing the determination of reactive oxygen species (ROS) during the photocatalytic degradation of the hepatotoxin, microcystin-LR in water by N-F co-doped TiO_2 showed that the reduction of molecular oxygen by photogenerated electrons rather than hydroxyl radicals produced by oxidative reactions of photogenerated holes is the key factor in VLA photocatalysis [34] indicating that the redox potential of holes in various photocatalysts activated by visible light photons is relatively high, impairing their oxidation ability. In that case, unmodified TiO_2 photocatalysts may eventually outperform modified ones for solar light photocatalytic applications [35], indicating the necessity for further development of VLA photocatalytic materials by combining visible light harnessing with suitable structural modifications to improve photon capture and simultaneously extend the lifetime of photogenerated charge carriers for application in environmental remediation and solar to chemical energy conversion [12].

Although titania's morphological characteristics and most self-structural modifications are not directly related to visible light harvesting, judicious engineering of the semiconductor nanostructure by controlling the size, shape, facet growth and dispersion of TiO_2 nanomaterials may significantly enhance their photocatalytic performance by promoting charge separation and exploiting titania's most reactive crystallographic planes [36–38]. Among different structural and morphological modifications, mesoporous TiO_2 nanomaterials have been attracting much attention as a favorable nanostructure for the enhancement of titania's photocatalytic efficiency providing the advantages of high specific surface area, small crystal size and particle interconnectivity [39]. The underlying interconnected TiO_2 pore-network offers abundant adsorption/desorption sites for pollutant molecules and facilitates their diffusion through the pore channels during the photocatalytic reaction, while it may inhibit the aggregation of TiO_2 nanoparticles, all being important factors for the heterogeneous photocatalytic process [40]. The enhanced porosity can be further combined with compositional doping for the synthesis of mesoporous anion doped TiO_2 using the surfactant-assisted sol-gel method together with suitable surfactants and dopant precursors to simultaneously tailor titania' structural properties and implement lattice or surface doping toward high visible light-induced catalytic activity [41–46]. More importantly, structuring TiO_2 materials' porosity at different spatial scales leads to the fabrication of hierarchical porous architectures presenting multimodal pore structures that offer manifold advantages to the process efficiency [47]. In particular, recent advances in the self-assembly of nanoscopic building blocks enabled fabrication of hierarchically ordered macro/mesoporous photocatalysts with tunable inter- and intra-particle porosity [48–50]. These nanostructures featuring an interconnected network of hierarchical macro/mesopores afforded significant improvements in their photocatalytic activity by enhancing molecular diffusion kinetics as well as increasing the accessible surface area and the amount of adsorption and reactive sites (Fig. 1). Moreover, multiple reflections and scattering inside the materials' pores may effectively extend the optical path length of incident photons within the pore network and eventually enhance light harvesting that plays a pivotal role in the design of highly active photocatalysts [47].

A straightforward, though challenging approach that directly targets titania's ability to harness solar light is by shaping TiO_2 materials in the form of periodic photonic structures, where slow photon-induced amplification of light harvesting near the electronic absorption edge has been demonstrated [51]. Photonic crystals have been established as unique optical materials for controlling and manipulating the flow of light with high application perspectives in various technological fields

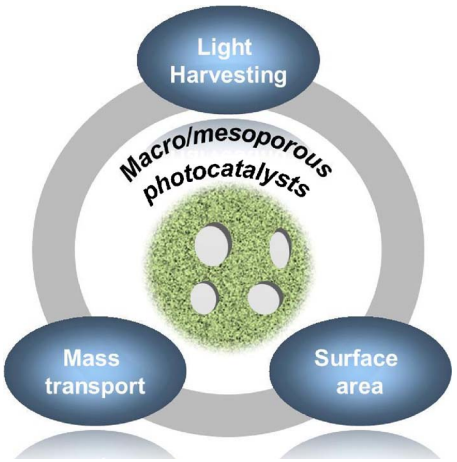

Fig. 1. Advantages of hierarchically ordered macro/mesoporous photocatalysts.

such as optoelectronics and telecommunications [52]. However, their utilization in semiconductor photocatalysis has only recently emerged as an innovative structural modification for improving light harvesting by photocatalytic nanometarials and enhancing light-matter interactions [53]. In fact, despite the great potential of photonic crystal-induced amplification of titania's photoreactivity demonstrated by the seminal work of Ozin et al. [51], the application of photonic crystals in TiO_2 photocatalysis has relatively lagged, most likely because of the inevitable delay in replacing complex and expensive top-down semiconductor fabrication techniques initially applied for photonic crystals by the more facile, versatile and low-cost bottom-up self-assembly methods, as expertly pinpointed by Freymann et al. [54]. Progress in the fabrication of metal oxide and titania photonic crystals based on colloidal self-assembly [54–58] resulted in a rapid upsurge of research activity over the last few years, reported in some excellent recent reviews in photonic nanostructures and their photo-induced applications [59–62], rendering photocatalytic photonic crystals an emerging topic of topical interest in the field of heterogeneous TiO_2 photocatalysis. However, the latter works were primarily focused on the application of photonics on solar to electrical energy conversion and photovoltaics, Li ion batteries and electrochromics [59,60,62], as well as water splitting and photocatalysis [61,62], where visible light activation was though sporadically addressed.

In this review, a timely summary of the latest advances in the development of photonic crystal photocatalysts, primarily based on titania, is provided with particular emphasis in the design, fabrication, structural and optoelectronic properties, performance and application potential of VLA photonic crystals. The prospect of photonic crystal-assisted VLA photocatalysis as an integrated approach that combines the unique advantages of photonic structures and hierarchical porous materials for enhanced light harvesting, surface area and transport kinetics [63] with expedient modifications of titania's electronic properties to boost the photocatalytic performance under visible light, is explored. To this aim, the synthetic methods and the fundamental structural and optical properties of photonic crystals are first introduced in the context of light harvesting applications. Subsequently, up to date experimental evidence for the amplification effect of photonic nanostructures on the photocatalytic performance mainly of titania and other wide band gap semiconductor under UV excitation is summarized. The application of photonic crystals in VLA photocatalysis are then thoroughly reviewed following the distinct strategies currently pursued for titania's visible light activation, i.e. dye sensitization, non-metal and self-doping, coupling with metals and plasmonic NPs, heterostructuring with visible light active nanomaterials (narrow band gap semiconductors, quantum dots and graphene) and the utilization of alternative VLA semiconductors including ternary metal oxides. The review is concluded with an outlook of pertinent challenges and

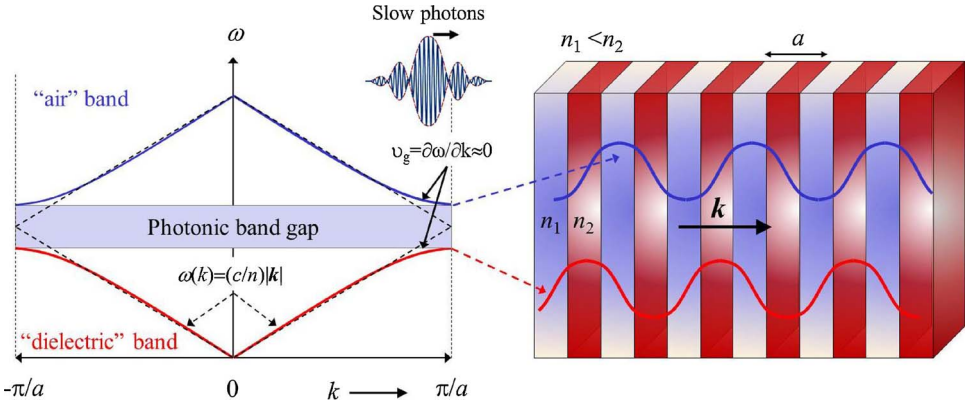

Fig. 2. Photonic band gap formation in a 1D periodic stack consisting of alternating dielectric layers with different RIs ($n_2 > n_1$).

recommendations for future research on the design of efficient VLA photonic crystals photocatalysts, intended to stimulate research and development in this emerging topic in heterogeneous photocatalysis.

2. Structural and optical properties of photonic crystals

2.1. Periodic structures and photonic band gap formation

Photonic crystals are periodically ordered structures characterized by the spatial modulation of their refractive index n (or, equivalently, dielectric function) on a length scale comparable to the wavelength of light [64,65]. The refractive index periodicity modifies radically light propagation in these heterostructures compared to their individual material constituents; likewise the periodic lattice potential modifies free electron motion in crystals. The key feature of photonic crystals enabling light manipulation is their capacity to create photonic band gaps (PBGs), wherein photons are not allowed to propagate or be emitted providing the optical analogue to the semiconductor's electronic band gap [66]. Stacks of alternating dielectric layers, introduced a century ago by Lord Rayleigh [66], constitute the prototype one-dimensional (1D) photonic crystal (Fig. 2). Interference of forward and backward propagating waves after reflection at the interfaces of these 1D heterostructures, nowadays called Bragg mirrors, results in the formation of standing waves at frequencies fulfilling the Bragg condition i.e. at the boundaries ($k = \pm \pi/a$) of the 1st Brillouin zone for the 1D stack with lattice constant a [54]. This causes the opening of a forbidden frequency (energy) range, i.e. a band gap, in the dispersion relation $\omega(k)$ between the photon frequency ω and wave vector k ($|\boldsymbol{k}| = k = 2\pi/\lambda$ with λ being the vacuum wavelength of light). In that way, the dispersion relation deviates from the regular linear behavior $\omega(k) = (c/n)|\boldsymbol{k}|$ (c = the vacuum speed of light) for light propagation in a homogeneous, isotropic material, as shown in Fig. 2. The electric field antinodes (amplitude maxima) for the two possible standing waves are accordingly localized at the high/low refractive index layers, yielding the lower/higher frequency photonic bands, conventionally called "dielectric" and "air" bands, respectively. Changing the periodicity, i.e. lattice constant and/or refractive index (RI) of the alternating layers in the 1D structure modifies the PBG spectral position and width (broadens with the increase of RI contrast), respectively.

Although PBGs are ubiquitous in any 1D dielectric stacks with non-zero RI contrast, its formation becomes more complex when extending the structural periodicity to higher dimensions. Moving to two (2D) and three (3D) dimensional photonic structures, forbidden frequency intervals may occur for different directions of light propagation, which, only under favorable conditions of sufficient RI contrast, lattice symmetry and filling factor, can merge to the same frequency range, leading to the formation of a complete, omnidirectional PBG. These partial gaps are commonly referred to as "stop" bands to be differentiated from the complete PBGs or simply gaps, where light propagation is inhibited for all possible wave vectors [54]. Although diamond and diamond-like lattices were predicted to be most amenable to the formation of complete PBG (an omnidirectional gap has been early predicted between the 2nd and 3rd photonic bands of the diamond structure for RI contrast higher than 2.8 [67]) because of their low filing factor (the atomic packing fraction of the diamond lattice is only 0.34) and weak directional anisotropy for light propagation (nearly spherical 1st Brillouin zone) [66], practical realization turned out to be rather difficult and technologically challenging (the most outstanding examples being the "Yablonovite" [68] and "Woodpile" [69] structures, mainly operated at microwave or millimeter wavelengths). Research interest has therefore moved to "natural" self-assembled structures, the most prominent being artificial opals [55], fabricated by the spontaneous organization of colloidal dielectric spheres to close packed lattices, especially the thermodynamically stable face centered cubic (*fcc*) lattice [70]. Despite their 3D ordered structure, opals that usually self-assemble with their close packed (111) planes parallel to the substrate (Fig. 3) do not afford a complete PBG, independently of the RI contrast [66]. In fact, their close packed structure permits only the formation of a pseudo-PBG (stop band) between the second and third bands for wave propagation along the ΓL-direction in reciprocal space, i.e. the [111] crystal direction in real space (L-pseudogap). This results in a characteristic dip of the transmittance (T%) spectrum for incident light normal to the (111) planes, which are parallel to the substrate surface (Fig. 3) [71].

Nevertheless, using opal colloidal crystals as sacrificial templates their replica, inverse structure can be fabricated by filling the interstitial space between the spheres with the material of choice followed by the selective template removal by calcination or chemical etching [56]. The *inverse opal* structure consists of an *fcc* lattice of air spheres within the dielectric background of the infiltrated material, and possesses a full PBG between the eighth and ninth photonic bands provided that RI contrast is higher than 2.8 and losses due to material's optical absorption are devoid [70,72].

This approach enabled large scale synthesis of Si photonic crystals with complete 3D PBG, above silicon's absorption edge, in the near-IR region (1.46 μm) by the conformal deposition of high refractive index Si (n = 3.45 at 1.5 μm) on SiO_2 opal templates by chemical vapor deposition (CVD), as shown in Fig. 4(a) [73]. Photonic band structure calculations for the Si inverse opal predicted a full PBG for 88% Si infiltration into the void space of the *fcc* opal, as shown in Fig. 4(b), which were in perfect agreement with the experimental reflection/transmission spectra that revealed two distinct maxima/minima, an intense low frequency peak at 2.5 μm corresponding to the low energy L-pseudogap and the narrow peak at 1.46 μm due to the full PBG at higher energy, depicted in Fig. 4(c). The deposition of planar, single-crystalline Si photonic crystals was later implemented by Vlasov et al. [74] combining a temperature gradient in the vertical deposition of the opal template to prevent sedimentation of micrometer sized silica spheres and low-pressure CVD infiltration. On the other hand, titania

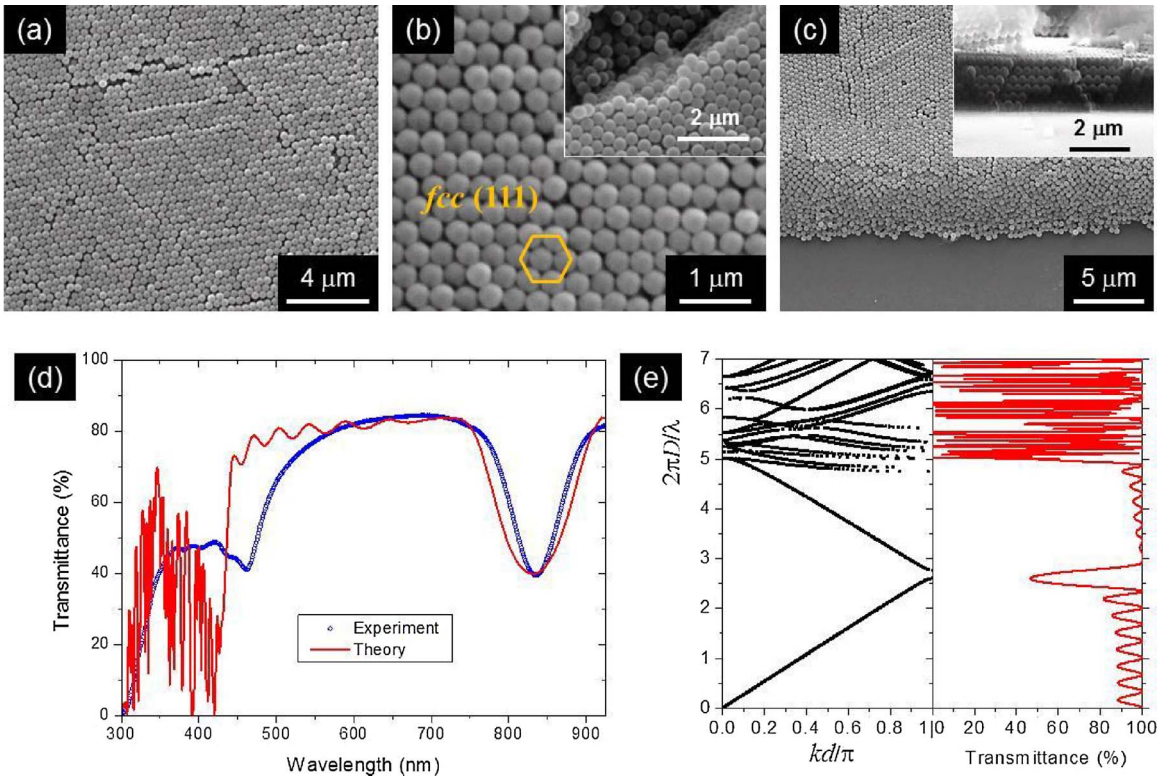

Fig. 3. (a), (b) Top and (c) side view SEM images of opal films prepared by the self-assembly of monodisperse (350 nm diameter) polystyrene spheres, at different magnifications. (d) Experimental and theoretical transmittance (T%) spectrum for a slab of 8 (111) layers on glass substrate, and (e) photonic band structure in units of normalized frequency along the [111] direction and the corresponding transmittance for a plain 8-layers thick slab [71]. Copyright © 2017 Elsevier B.V.

inverse opals were successfully fabricated by the liquid phase infiltration of sol–gel precursors that enter the interstices of the opal template by capillary forces, further assisted by suction or vacuum [75,76].

This relatively facile templating method turned out as the most prevalent for the fabrication of TiO_2 inverse opals, following the sequential scheme of Fig. 5(a) [56,77,78]: 1) opal formation by the self-assembly of colloidal polymer, usually polystyrene (PS) and PMMA or silica (most suitable for high temperature processing applications) monodisperse spheres (Fig. 5(b)–(f) typically implemented by the vertical deposition method [57], infiltration of the opal voids using wet impregnation or gas-phase deposition of liquid or vapor titania precursors, followed by the chemical/physical conversion of the precursor via e.g. the sol-gel process of hydrolysis-condensation within the opal interstices (Fig. 5(g)–(k) [54]. Finally, the template is removed, typically by calcination of the polymeric matrix that simultaneously results in the crystallization of the amorphous titania skeleton primarily to the anatase TiO_2 phase [79]. High quality titania inverse opals with interconnected macropores of tunable size can be thus fabricated from well ordered opal templates using polymer spheres of different diameters, as shown in Fig. 5 [78].

However, despite the marked progress in the colloidal template self-assembly of inverse opals, the formation of various crystal defects such as point, line and stacking defects, compact overlayers and cracks limits significantly the domain size and long range order usually down to $\leq 10\,\mu m$ [56]. In particular, volume shrinkage and cracking that occurs during liquid infiltration, drying and conversion of the sol–gel precursor compromise the films' quality, as schematically shown in Fig. 6(a) [80], and allows empirical only control over the void sphere diameter that becomes smaller (typically 20–30%) than those of the polymer opal matrix. More recently, co-assembly of the polymer colloidal spheres with hydrolyzed silicate sol-gel precursor solutions has been demonstrated by Aizenberg et al. [80] as an effective method that evades liquid infiltration into the preassembled template, as schematically shown in Fig. 6(b), and leads to robust, large-area silica inverse opal films devoid of overlayers and cracks, due to the "gluing" action of the sol-gel precursor, displayed in Fig. 6(c)–(e). This method has been successfully applied for the one-step growth of TiO_2 inverse opals by co-assembly of a water-soluble sol-gel precursor, titanium(IV)-bis-lactato-bis-ammonium dihydroxide-TiBALDH) solution and PMMA colloidal spheres. Co-deposition of binary aqueous dispersions of polymer microspheres with preformed, non-aggregated anatase TiO_2 NPs has been first applied by Meng et al. [81] leading to highly ordered porous structures, especially for ultrafine titania particles. This fabrication route was recently implemented under accelerated solvent evaporation by Seo et al. [82], enabling fast deposition of large area TiO_2 inverse opal films that presented reduced cracking and volume shrinkage, though less-ordered titania-rich bottom layers that, nonetheless, improved film adhesion to the glass substrate.

Excessive defect formation can be further mitigated at the cost of applying relatively time consuming and expensive layer-by-layer vapor phase processes such as atomic layer deposition (ALD) that enables smooth conformal coating of the opal template [83]. The fabrication of high quality TiO_2 inverse opals by low temperature ALD has been demonstrated by King et al. [84], showing the formation of highly ordered titania macropores interconnected through smaller pores formed at the contact points between adjacent spheres of the opal films along with small air pockets in the opal interstices indicative of the highly conformal ALD process, as shown in Fig. 7(a) and (b).

Furthermore, stepwise ALD infiltration enables precise control over the opal void filling fraction and tuning of the consequent L-pseudogap position, as shown by the variation of the TiO_2 inverse opals reflectivity with the ALD infiltration cycles, displayed in Fig. 7(c) and (d). In that case, the anticipated red shift (*vide infra*) of the low energy stop band (L-pseudogap) along with a higher energy peak is observed with the increase of titania's filling fraction that reached a maximum at ca. 88% infiltration after 350 ALD cycles, where the *fcc* pores are predicted to

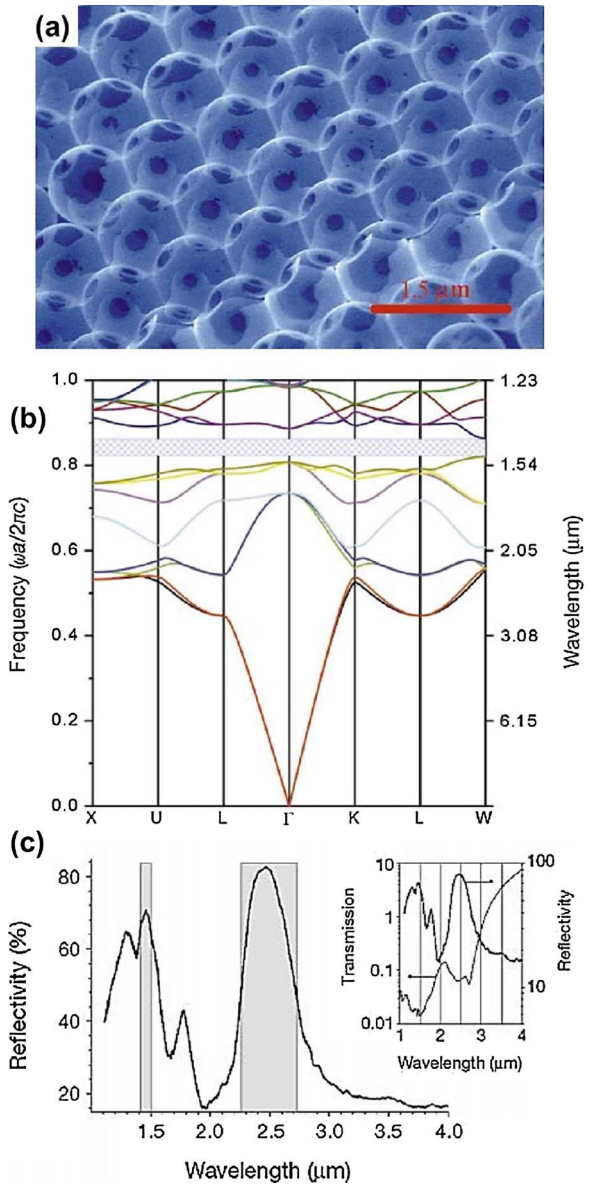

Fig. 4. (a) SEM image of the [111] facet and (b) photonic band structure of the Si inverse opal calculated for 88% silicon infiltration. The complete PBG is shown by the cross-hatched region. (c) Experimental refection spectrum where shaded regions at 2.5 and 1.5 mm show the calculated positions of the first stop band and the complete PBG, respectively. The inset shows the corresponding transmission spectrum on a logarithmic scale, where the narrow feature at 2.7 mm is due to water absorption [73]. Copyright © 2000 Nature Publishing Group.

close.

2.2. Bragg diffraction and slow photon management

Despite the sizable refractive index of bulk titania (2.6–2.9 at 500 nm) [85,86], the corresponding RI contrast of the nanocrystalline TiO_2 skeleton in the *fcc* inverse opal lattice [87] remains marginally below the threshold of 2.8 predicted for full PBG formation at the visible range and above titania's electronic absorption edge ($\lambda > 390$ nm), especially for the anatase TiO_2 that is the most stable phase under confined sol-gel growth within the opal interstices [79]. On the other hand, the stop band due to the L-pseudogap persists for light propagation along the [111] crystal direction for well-ordered titania inverse opals [84]. Its frequency can be varied within the UV–vis-NIR range depending on the final void sphere diameter [Fig. 5(k)] as well as the RI contrast between the inorganic frame and the medium filling the void space (air, water or other solvent) and titania's filling fraction [51,77,78,88]. For frequencies within the L-pseudogap, the associated wave vector attains imaginary values and light propagating along the [111] direction is exponentially attenuated, leading to enhanced stop band reflection. The stop band can be accordingly identified in the transmission and reflection spectra as regions of low (high) transmission (reflection) signal at normal incidence to the film surface that is parallel to the (111) planes of the *fcc* inverse opals. Although rigorous band structure calculations are required to accurately fit the experimental optical spectra [89,90], the stop band spectral position can be analytically approximated by Bragg's condition of constructive interference, alike diffraction of X-rays by a periodic crystal lattice, provided that Snell's law of refraction is taken into account [91], as shown in Fig. 8.

The modified Bragg's law for first order diffraction from the (111) planes, takes the form:

$$\lambda = 2d_{111}\sqrt{n_{eff}^2 - \sin^2\theta}$$

where λ is the wavelength of the stop band minimum/maximum, $d_{111} = a/\sqrt{3} = \sqrt{2/3}D$ is the interplanar spacing of the (111) planes with a being the cubic lattice constant and D the sphere diameter, n_{eff} is the volume-weighted average of the refractive indexes of the constituent spheres n_{sphere} and the material occupying the interstitial voids n_{void} defined as $n_{\text{eff}}^2 = n_{\text{sphere}}^2 f + n_{\text{void}}^2(1-f)$ with f the filling fraction ($f = 0.74$ for the *fcc* lattice), and θ is the angle between the incident beam and the plane normal. The photonic crystal is accordingly considered as a homogeneous medium with effective refractive index n_{eff} and thickness $t = Nd_{111}$,where N is the number of sphere layers. It should be noted that this definition of n_{eff} is essentially the simplest approach among the *effective medium approximations* to the RI of the composite photonic structure using its average dielectric constant $\varepsilon_{avg} = \varepsilon_{sphere} f + \varepsilon_{\text{void}}(1-f) \Rightarrow n_{eff} = \sqrt{n_{\text{sphere}}^2 f + n_{\text{void}}^2(1-f)}$. However, despite its simplicity, this approach is quite accurate for low dielectric constants ($\varepsilon < 6$), while a better approximation can be obtained by applying the Maxwell–Garnett model, where the local field within the composite structure is taken into account [92].

At normal incidence $\theta = 0^\circ$, first order diffraction from the (111) planes assumes the simple form $\lambda = \frac{2\sqrt{2}}{\sqrt{3}} n_{\text{eff}} D$, which shows that the stop band varies linearly with the sphere diameter D for constant RI. Moreover, this simple analytical approach based on modified Bragg´s law in combination with angle and solvent dependent transmittance/reflectance measurements of the stop band frequencies can be used to determine independently the void sphere size and titania's filling fraction in the inverse opal structure that commonly falls short of the theoretical value 0.26 for the *fcc* lattice due to its nanocrystalline nature and the accompanying porosity [88,91,93].

Nevertheless, the enhanced stop band reflection in titania inverse opals at frequencies within the L-pseudogap is a rather adverse effect for the photocatalytic process, as light absorption is diminished at these frequencies. The distinctive feature of photonic crystals that underlies their potential to amplify light harvesting and photocatalysis, lies in their ability to retard light propagation and thus extend the path length of incident photons within the periodically structured TiO_2 network. This unique effect is caused by the strong reduction of the group velocity v_g for photons propagating with energies at the edges of the stop band, which are accordingly called **slow photons**. In the simple case of 1D photonic crystals, the group velocity of light v_g i.e. the velocity at which a pulse propagates within a medium defined by the derivative $v_g = d\omega/dk$, becomes extremely low at frequencies near the edges of the L-pseudogap [94], as the dispersion relation $\omega(k)$ progressively flattens (Fig. 2) and ideally should vanish within the band gap, where standing (non-propagating) waves develop for a perfect infinite photonic crystal [95]. At frequencies approaching the stop band from the long wavelengths (red edge) side, light tends to form a standing wave that is

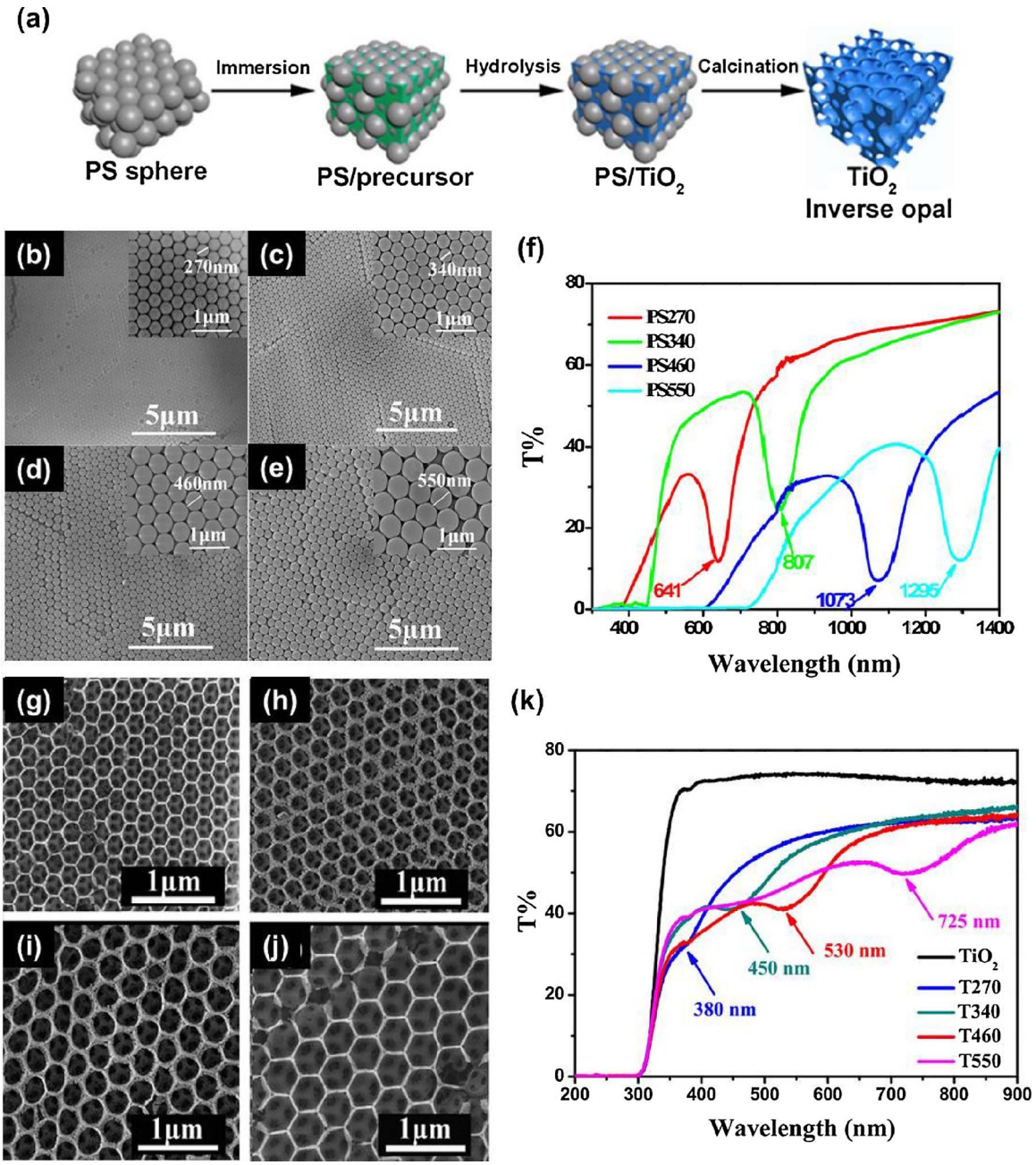

Fig. 5. (a) Synthesis process of TiO_2 inverse opals [77]. (b)–(e) SEM images of colloidal opal templates assembled from 270, 340, 460, and 550 nm PS spheres and (f) the corresponding transmittance spetra in air with arrows depicting the stop band positions. (g)–(j) SEM images of the corrsponding TiO_2 inverse opals after succesive infiltration and calcination, and (k) transmittance spetra in air showing the size dependent stop bands [78]. Copyright © 2013 American Chemical Society.

mainly localized in the high RI (*dielectric band*) part of the photonic crystal, i.e. the titania frame of the inverse opal structure. At short wavelengths (blue edge), the light standing wave is primarily localized in the low RI (*air band*) region of the photonic crystal. These photons are accordingly called *red*- and *blue*-edge slow photons. This distinct effect that enables structural manipulation of light propagation has been applied for the first time in 2003 by Mallouk et al. [94], to enhance the photocurrent of dye-sensitized solar cells by depositing a TiO_2 inverse opal film on a conventional porous nanoparticulate titania photoelectrode, by means of both the back reflection of light in the stop band region of the photonic crystal that acts as a dielectric mirror and the excitation of localized slow photon modes within the nanocrystalline absorbing layer [96–98].

Slow photons have been directly identified by time resolved experiments using ultra short laser pulses [99] and more recently white light-interferometry [100,101] in polystyrene (PS) and silica opal photonic crystals. Thereby, the dispersion relation $\omega(k)$ could be experimentally determined over a large spectral range around the opal L-pseudogap and by calculating its first derivative, the spectral response of v_g or equivalently the group index defined by the inverse group velocity normalized to the vacuum speed of light $n_g = c/v_g$ could be measured. Increasing the thickness of the opal films results in the appearance of two distinct n_g peaks at frequencies close to the pseudogap edges along with a region of low n_g in between, indicative of the bending of the photonic bands and the concomitant deviation of $\omega(k)$ from linearity that leads to the suppression of group velocity v_g at the edges of the L-pseudogap in the opal *fcc* lattice [100,101]. This is seen in Fig. 9 depicting the photonic band structure calculated by Galisteo-López et al. [101], the specular reflectance R and transmittance T, the diffuse intensity derived as D = 1-T-R (for zero absorbance) for a 42

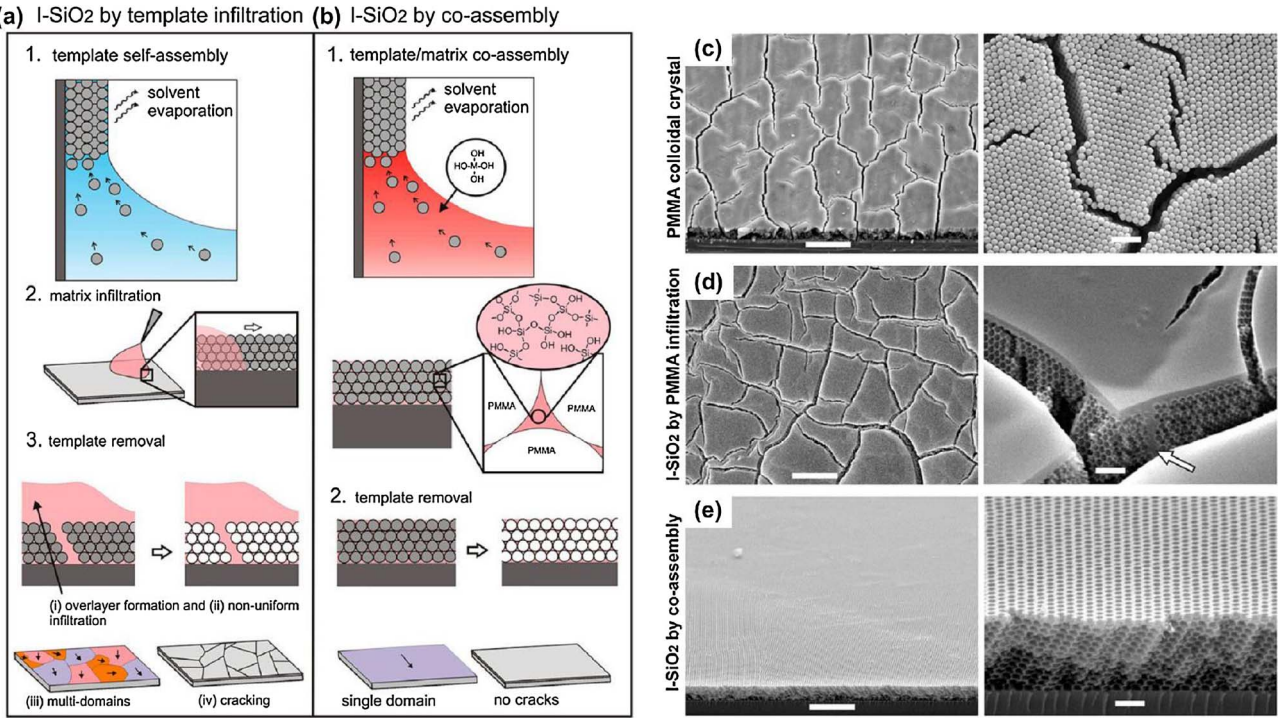

Fig. 6. Schemes of (a) "conventional" colloidal template self-assembly and (b) co-assembly of colloids with a soluble precursor for the synthesis of silica inverse opals (I-SiO_2). SEM images at two different magnifications (left scale bars = 10 μm, right scale bars = 1 μm) of (c) PMMA colloidal crystal film showing cracks propagating along the close-packed {111} planes, (d) I-SiO_2 inverse opal film by sol-gel infiltration showing cracking, overlayer coating and a region of SiO_2 infiltration into a preexisting template defect, and (e) I-SiO_2 film by PMMA/sol-gel co-assembly, showing highly uniform films [80].Copyright © 2010 National Academy of Sciences/Proceedings (Freely available online through the PNAS open access option).

layers thick PS opal along the ΓL direction [102] in comparison with the measured n_g variation for a 40 layer thick film. In the latter case, the group index reaches a maximum value of 2.5 corresponding to ca. 40% slower v_g at the high-energy edge of the stop band, though considerably lower n_g was observed at the low energy edge. Comparison with the diffuse optical spectrum shows that the slowing effect is closely related to an increase in diffuse intensity that becomes enhanced at the edges of the L-pseudogap. This behavior could be rationalized as slow photons experience a longer optical path, which thus increase the probability for light scattering by lattice defects and leads to the diffuse intensity enhancement at the stop band edges, contrary to frequencies close to the pseudogap center, where the suppressed penetration depth of light

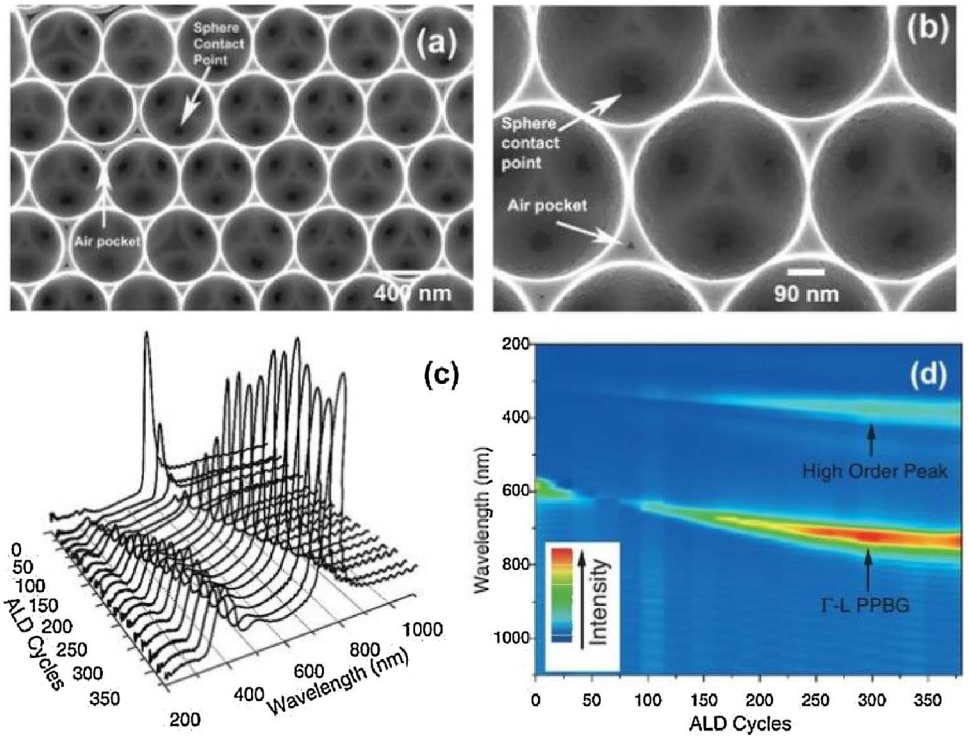

Fig. 7. (a), (b) SEM images of a TiO_2 inverse opal fabricated by ALD infiltration of a 466 nm sacrificial SiO_2 opal template, showing clearly the intermediate pores formed at the sphere contact points before template removal and the air pockets at the opal interstices. (c) Specular reflectivity of a stepwise TiO_2 infiltrated 266 nm SiO_2 opal and (d) the interpolated intensity plot of wavelength vs. ALD cycles indicating the evolution of the L-pseudogap position [84]. Copyright © 2005 John Wiley & Sons, Inc.

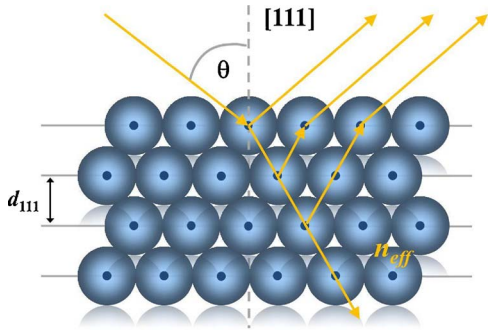

Fig. 8. Bragg diffraction of light incident on the (111) *fcc* crystal planes of an opal at angle θ modified by refraction within the composite medium with n_{eff} refractive index.

inhibits diffuse scattering.

Another interesting spectral feature, though not related to the photonic crystals per se, is the presence of secondary interference fringes on the reflectance and transmittance spectra at frequencies outside the stop band range (Fig. 9). These oscillations stem from Fabry-Pérot resonances due to interference of the light reflected at the free surfaces of the photonic films. Although rigorous calculations are needed for their accurate description, Fabry-Pérot fringes provide a good Fig. of merit for the film quality and particularly for the thickness uniformity of the photonic crystal domains, as inhomogeneities lead to the smearing of their intensity, while they can be also used to deduce the effective RI of the films [102,103].

3. Slow photon-assisted TiO_2 photocatalysis under UV–vis light

Slow photon-induced amplification of titania's photocatalytic reaction rate has been put forward by Ozin et al. [51], by tuning the L-pseudogap of TiO_2 inverse opals within titania's electronic band gap so that the consequent stop band reflection is largely suppressed by the strong TiO_2 electronic absorption, while slow photons at the red edge of the stop band enhance the relatively weak optical absorption of titania near its absorption edge. Pertinent results on photonic crystal-assisted semiconductor photocatalysis under UV light are summarized in Table 1.

In their seminal work, Chen et al. [51] demonstrated a marked improvement of titania's photocatalytic efficiency on dye sensitized anatase TiO_2 inverse opal films with methylene blue (MB) as model pollutant, under both monochromatic UVA and white light irradiation. The photocatalytic activity was evaluated by implementing "solid-state" (dry) photodegradation experiments on the MB sensitized films to avoid contributions from molecular diffusion in the pore network and ensure the high RI constant of the photonic crystals. Stop band reflectance of the anatase inverse opals was continuously varied from the visible to the UVA range by infiltrating PS opal templates with sphere diameters from 380 down to 130 nm with titanium butoxide, as shown in Fig. 7(a)–(d). Illumination with narrowband UVA light at 370 ± 10 nm i.e. within the electronic band gap of anatase, resulted in a pronounced non-monotonous variation of the MB degradation rate with the stop band frequency, which could be further adjusted by changing the irradiation incidence angle, as displayed in Fig. 7(e). A two-fold enhancement of the MB degradation rate was thus achieved in comparison with conventional nanocrystalline TiO_2 (nc-TiO_2) films for the photonic crystals with stop band at ~350 nm either at normal or 20° off-normal light incidence on the (111) planes that shifted the stop band to the same wavelength according to modified Bragg's law. For these best performing inverse opals, the monochromatic UVA excitation matched closely the red edge of the corresponding stop band, where slow photons are expected to localize in the high RI part of the photonic crystal (titania skeleton), leading to the increase of the optical path length and the acceleration of reaction kinetics (Fig. 10).

On the other hand, the optimal stop band frequency for dry MB phtodegradation under white light illumination (Xe lamp with cutoff filter at $\lambda < 300$ nm) was blue shifted to 300 nm, where the detrimental effect of stop band reflection could be most effectively diminished by the strong electronic absorption of TiO_2. Control over the two competing photonic effects i.e. slow photons and the spectrally broader stop band reflectance by fine tuning the L-pseudogap position at energies well within TiO_2 electronic band gap to minimize reflective losses, has been accordingly inferred as the key factor for the improvement of photocatalytic performance under polychromatic illumination conditions.

The impact of structural disorder was subsequently investigated by Chen et al. [104] introducing different fractions of guest spheres of various sizes into the opal templates, especially those assembled from the 150 nm diameter PS spheres that produced the TiO_2 inverse opals with best photocatalytic performance (stop band at 300 nm) under white light. The inverse opal structures based on the (1-*x*)150-*x*180 binary template retained short-range order of the *fcc* closed-packed (111) planes for the whole compositional range with the 150 nm domain size decreasing with *x* [Fig. 11(a)]. On the other hand, phase segregation and significant disruption of the void packing was detected for the $(1-x)150-x210$ system, already from low *x* values, leading to the collapse of structural order at $x = 0.35$, where unoccupied interstitial space between the spherical voids was observed, as shown in Fig.11(b). The compositional variation of the stop band reflectance

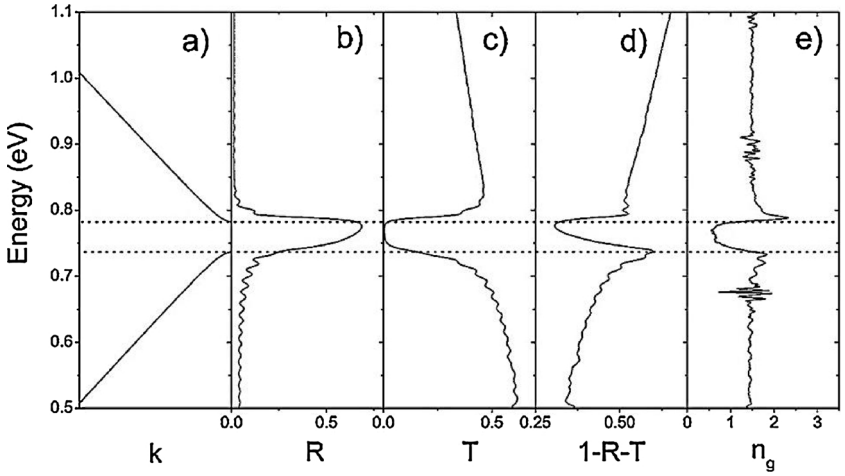

Fig. 9. (a) Band structure for a PS opal along the ΓL direction. (b) Reflectance, (c) transmittance, and (d) diffuse intensity for a 42 layers thick sample. (e) Group index n_g for a 40 layers thick sample [101]. Copyright ©2006 The American Physical Society.

Table 1
Photonic crystal photocatalysts for pollutant degradation under UV irradiation.

Photonic crystal	Porous template	Pseudo PBG	Photocatalytic evaluation	Irradiation conditions	Performance	Ref.
TiO_2 io films	130, 150, 180, 210, 240, 300, and 380 nm PS opals	280, 300, 325, 345, 370, 430, and 500 nm (air)	MB (s)	180 W Xe monochromatic 370(10) nm	EF ~ 2.4 345 nm stop band	[51]
			7×10^{-6} M pH = 8	120 W Xe λ > 300 nm	EF ~ 2.2 300 nm stop band	
TiO_2 io films	Binary PS opals 130, 150, 180, 210 and 240 nm	385–395 nm (air)	MB (s)	Xe lamp	EF ~ 1.5 at $x = 0.4$ for $(1 - x)$ 150 − x180 binary TiO_2 io	[104]
			7×10^{-6} M pH = 8	(40 mW/cm^2) λ > 300 nm		
TiO_2-SiO_2 io films	240, 270, 300, 420 nm P (St-MMA-AA) opals and P123	350, 365, 386, and 512-600 nm (air)	RhB (s) 10^{-4} M	UV lamp monochromatic 365(15) nm	EF ~ 2.0 vs. TiO_2 io EF ~ 15.6 vs. nc TiO_2	[105]
TiF_6^{-2} post treated TiO_2 io films	130, 150, 180, 210 nm PS opals	300–370 nm	MB (aq) 7×10^{-6} M pH = 8	Xe lamp λ > 300 nm	EF ~ 1.3 for 0.5 filling fraction	[106]
TiO_2 io films	Carboxyl-modified PS, "sandwich" vs dropwise sol-gel infiltration	320 nm	MO (aq) 10^{-3} M 50 ml	250 W Hg, 365 nm	NA	[107]
TiO_2 io powder	0.5 and 1.0 μm PS opals	NA	MB (aq) 4.45×10^{-6} M 0.1 g/1 L	8 W Hg lamp 254 nm	0.042 min^{-1} (0.5 μm) 0.034 min^{-1} (1.0 μm) 0.025 min^{-1} (P25)	[108]
TiO_2 io powder	250, 350, 480, 550 nm PS opals Calcination at 550, 700, 900 °C	NA	RhB (aq) 10^{-5} M 0.05 g/50 mL	UV lamp 370 nm	0.39 min^{-1} for 370 pore size at 700 °C vs 0.23 min^{-1} for P25	[109]
TiO_2 io powder	125 nm PMMA opal	270–280 nm (air)	Phenol (aq)	TL K05 UVA (×5), 365 nm	EF ~ 2 at 365 nm	[110]
		320–330 nm (water)	10^{-4} M, pH = 3 5 ml	TUV PL-S 254 nm	EF ~ 1 at 254 nm	
TiO_2 io films	250 nm PS opal Calcination at 700, 800 °C	426, 392 nm (water, 0°)	RhB (aq) 10^{-5} M, 10 mL	300 W Xe 250–780 nm 0°, 20°, 45° incidence	EF ~ 2.0 (0° and 700 °C) EF ~ 1.9 (45° and 800 °C)	[112]
TiO_2 io films	250 nm PS opal	448, 426, 392, 375, 369 nm (water, 0°)	RhB (aq)	300 W Xe	EF ~ 1.9 (20°–550 °C)	[113]
	Calcination at 550, 700, 800, 900, 1000 °C		10^{-5} M, pH = 9.5	250–800 nm 0°, 20°, 45° incidence	EF ~ 2.0 (0°–700 °C) EF ~ 1.8 (45°, 800 °C)	
TiO_2 io coating	120 nm PS opals on quartz rod	~350 nm (air)	1,2-Dichloro benzene (g) 436 mL min^{-1}	UVA lamp 300–380 nm 116 mW cm^{-2}	EF = 3.48 vs P25 coating	[115]
TiO_2 io powders -films	180, 215, 270, 310, 375, 450 nm PMMA opals	300–692 nm (air)	Ethanol (g) 0.33 μmol/ml	100 UVA 365 nm 6.5 mW cm^{-2}	EF = 1.9–2.1 red edge slow photons	[93]
TiO_2 io films	124, 196, 264 nm PS opals	< 350 nm, 455 nm (water)	Acetaldehyde (g) ISO 22197-2:2011 5 L min^{-1}, 5 ppm	15 W UVA 365 nm, 1.0 mW cm^{-2}	Constant photonic efficiency (EF ~ 1)	[116]
Bilayer nc-TiO_2/SnO_2 io films	PS opal	350 nm	MO (aq) 10 ppm, 3 mL	150 W Xe lamp 3.5 mW cm^{-2}	EF ~ 1.4	[118]
Bilayer nc-TiO_2/SnO_2 io	PS opals	370, 415, 525 nm	RhB (s) 10^{-3} M	150 W Xe lamp 2 mW cm^{-2}	EF ~ 2	[119]
Bilayer nc-TiO_2/SiO_2 opals	188 nm SiO2 opal 6-48 layers thick	380 nm	Acetaldehyde (g) 8.93 μmol L^{-1}	500 W Xe monochromatic 380 nm 1.2 mW cm^{-2}	EF = 1.92 at 48 SiO_2 layers	[120]
Trilayer TiO_2 io films	175 and 230 nm PS opals	346 and 432 nm (water)	RhB (aq) 10^{-5} M, 10 ml	300 W Xe 150 mW cm^{-2}	EF = 6.4 vs single layer io films	[121]
ZnO io films	270, 295, 351 nm carboxyl modified PS opals	410 nm, 450 nm and 530 nm	MO (aq) 5 ppm 4-CP (aq) 4 ppm	500 W Xe lamp 300–800 nm 130 mW cm^{-2}	EF = 2.2 (MO) EF = 1.9 (4-CP) Photostability	[124]
ZnO io films	260, 470 nm P(St-MMA-SPMAP) opals	467, 815 nm (423 nm 2nd order)	RhB (aq) 10^{-5} M, 10 ml, pH = 9.5	300 W Xe 250–780 nm 0°, 20°, 40° incidence angles	EF = 5.5 at 40° ZnO-470 nm (13.7 × 10^{-3} min^{-1}) Photoinduced wetting	[125]
β-Ga_2O_3 io films	180, 226, 357, 405 nm PS opals	260, 290, 425, 500 nm	MO 1.5 × 10^{-5} M RhB 1.5 × 10^{-5} M BA 4.1 × 10^{-5} M (aq)	UVC lamp (×3) TUV 4W/G4 T5 254 nm	EF = 1.4 (MO) E = 1.6 (RhB) EF = 1.3 (BA) β-Ga_2O_3 io-180 m	[127]

(*continued on next page*)

Table 1 (*continued*)

Photonic crystal	Porous template	Pseudo PBG	Photocatalytic evaluation	Irradiation conditions	Performance	Ref.
$ZnGa_2O_4$ io films	190, 240, 300, 380 nm PS opals	295, 390, 470, 590 nm	MO (aq) 1.5×10^{-5} M 10 ml	UVC lamp (×2) TUV 4W/G4 T5 254 nm	96% MO removal 47.5% TOC 75 min for io-240 nm	[128]

io: inverse opals; EF: enhancement factor; (s) solid state; (aq) aqueous phase; (g) gas phase; NA: not available.

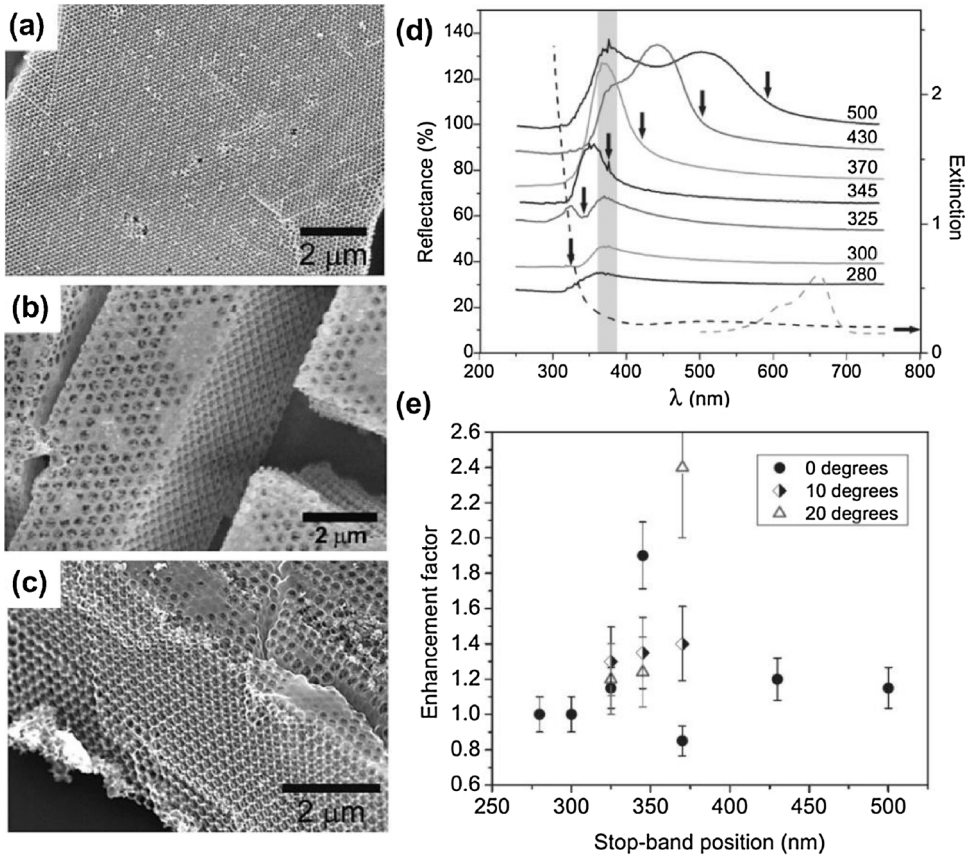

Fig. 10. SEM images of TiO_2 inverse opals obtained from (a) 150 (b) 210 and (c) 300 nm PS sphere templates. (d) Reflectance spectra (solid lines) of the inverse opals with stop bands in the range of 280–500 nm together with the extinction spectra of nc-TiO_2 and MB (black and gray dashed lines). The shaded band indicates the narrowband UVA spectral range. (e) Photocatalytic enhancement factor for the TiO_2 inverse opals as a fucntion of stop band position and incidenec angle of the monochromatic UVA irradiation [51]. Copyright © 2006 John Wiley & Sons, Inc.

could be only monitored for the less disordered $(1-x)150-x180$ inverse opals in water (due to the lower RI contrast that caused a red shift of the L-pseudogap) rather than air to evade overlap with the anatase absorption edge [Fig. 11(c)]. On the other hand, no stop band reflectance could be traced for any composition of the $(1-x)150-x210$ mixtures in air or water due to extensive disorder. Photocatalytic evaluation of the binary inverse opal systems by dry MB photodegradation experiments under polychromatic (white) light showed that for the less disordered binary system, a significant part (50%) of the performance enhancement could be retained for x up to 0.4 [Fig. 11(d)], indicating that a substantial amount of structural disorder and imperfection could be tolerated by the inverse opal structure with respect to practical photocatalytic applications.

The photocatalytic activity could be further augmented by Liu et al. [105] that implemented hierarchical macro/mesoporous TiO_2-SiO_2 (Ti-Si oxide) inverse opals by means of double-template synthesis combining core-shell P(St-MMA-AA) colloidal crystals as macro-templates and the Pluronic P123 amphiphilic triblock copolymer as mesopore directing agent with titanium isopropoxide (TTIP) and tetraethyl orthodilicate (TEOS) sol gel precursors, as shown in Fig. 12(a). The presence of 6 nm mesopores in the broader titania walls could be thus tailored through the "gluing" effect of silica that linked the anatase nanoparticles together to a thermally stable mesostructured framework withstanding short time (4 h) calcination at 650 °C, in contrast to prolonged thermal treatment (24 h) that inhibits mesopore formation due to the enlarged titania nanocrystallites, as shown in Fig. 12(b) and (c). Tuning the red edge slow photons of the Ti-Si oxide inverse opals to titania's electronic absorption by varying the crystal colloidal diameter, resulted in marked enhancement of the solid state photodegradation of the rhodamine B (RhB) dye under monochromatic 365 nm irradiation. Enhancement factors of 2.0 and 15.6 were identified for the RhB degradation rates with respect to plain TiO_2 inverse opals of similar stop bands and nc-TiO_2 films, respectively, attributed to the synergy of slow photons and high surface area of the mesostructured photonic crystals.

However, aqueous phase photocatalytic experiments under polychromatic light ($\lambda > 300$ nm) illumination by Chen et al. [106] showed that the pronounced slow photon amplified reactivity of the titania inverse opals under dry conditions was substantially moderated due to the reduced RI contrast of TiO_2 with water ($n = 1.335$ at 500 nm) that fills the spherical void space of the inverse structure and leads to the effective increase of group velocity that impairs slow photon enhancement. The latter could be, however, reinforced by increasing titania's filling fraction by post-deposition of TiF_6^{-2} using liquid phase infiltration of the TiO_2 inverse opals for different durations, followed by post thermal treatment to crystallize the additional TiO_2, as shown in Fig. 13(a)–(c). By increasing the TiO_2 content in the inverse opal prepared from the 130 nm PS template, the stop band reflection, which was completely suppressed in water by the strong TiO_2 electronic

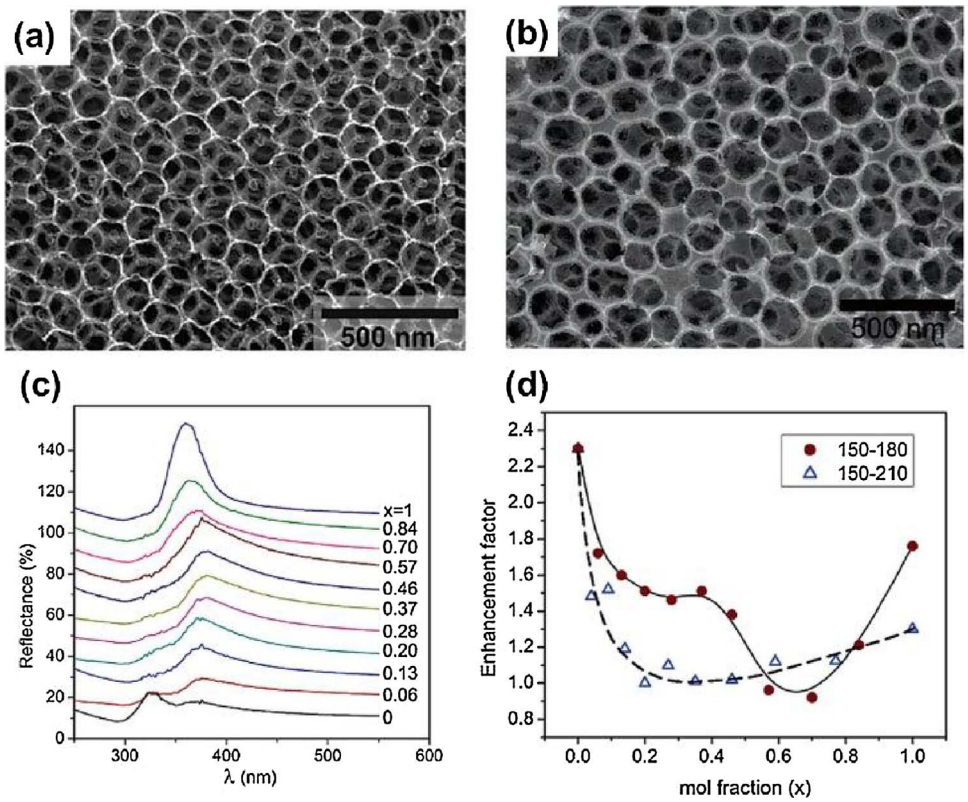

Fig. 11. SEM images of (a) $(1-x)150-x180$ and (b) $(1-x)150-x210$ TiO_2 inverse opals with x of 0.37 and 0.35, respectively. (c) Reflectance spectra of $(1-x)150-x180$ templated titania films in water. (d) Enhancement factor of the photocatalytic efficiency for the binary TiO_2 inverse opals as a function of composition (x). The solid and dashed lines are guides to the eye. [104]. Copyright © 2007 American Chemical Society.

absorption, red-shifted and a small peak emerged at 330 nm with increasing intensity with the deposition time, as shown in Fig. 13(d). Comparative photocatalytic evaluation for MB degradation with non-photonic films indicated that the higher filling fraction of TiO_2 results in ca. 30% enhancement of liquid phase photocatalysis by slow photons [Fig. 13(e)], where surface area and molecular diffusion were also concluded to be major aspects for the process efficiency.

The aqueous phase photocatalytic activity of TiO_2 inverse opal films with stop band reflection at 320 nm could be further enhanced for methyl orange (MO) degradation under UVA irradiation by optimization of sol-gel infiltration employing a "sandwich" method that inhibits the formation of compact overlayers and improves the reusability of the photonic films [107]. Subsequent work on powder samples of titania inverse opals supported the beneficial effects of the photonic structure on the degradation of different water pollutants, namely MB [108], RhB [109] and phenol [110] under UV irradiation. Thereby, photocatalytic experiments carried out in aqueous suspensions, alike conventional titania slurries, allowed performance comparison with the benchmark Aeroxide® P25 nanopowder catalyst and crushed or disordered specimens lacking long range periodicity as well as investigation of the influence of opal template diameter [108], calcination temperature [109], UV irradiation wavelength (254 vs 365 nm) [110] with respect to the stop band position in the UVA range and residual sulfate impurities from PS synthesis [111]. The latter, however, could be barely traced in the corresponding transmittance or reflectance spectra due to the polycrystalline state of the inverse opals and the random orientation of (111) domains with respect to the incident light. The resultant averaging effect combined with the strong contribution of TiO_2 electronic absorption attenuated the stop band reflectance obstructing unambiguous discrimination of slow photon effects from other factors like

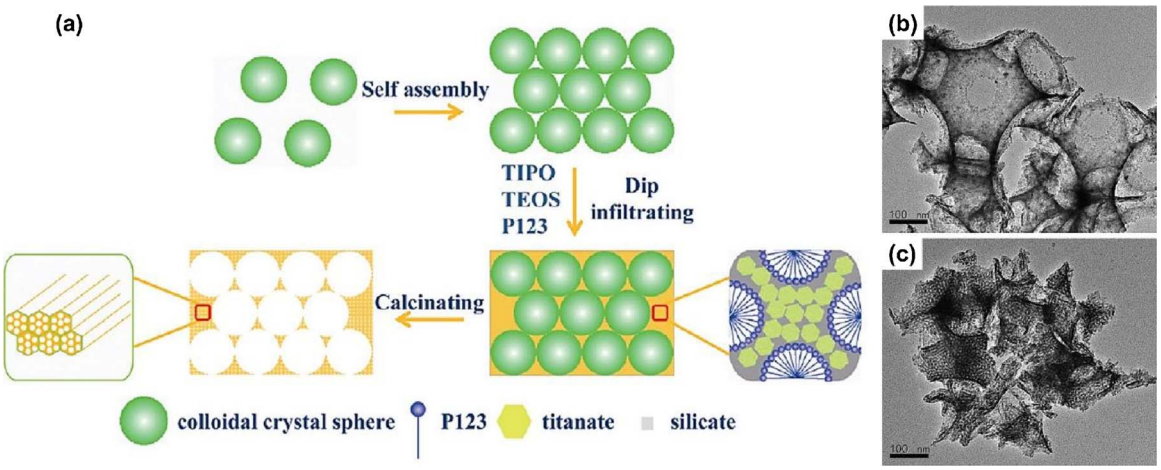

Fig. 12. (a) Double-template synthesis scheme of macro/mesoporous Ti-Si oxide inverse opals. Transmission electron microscopy (TEM) images of Ti-Si inverse opals calcined at (b) 450 °C, 24 h and (c) 650 °C, 4 h [105]. Copyright © 2009 American Chemical Society.

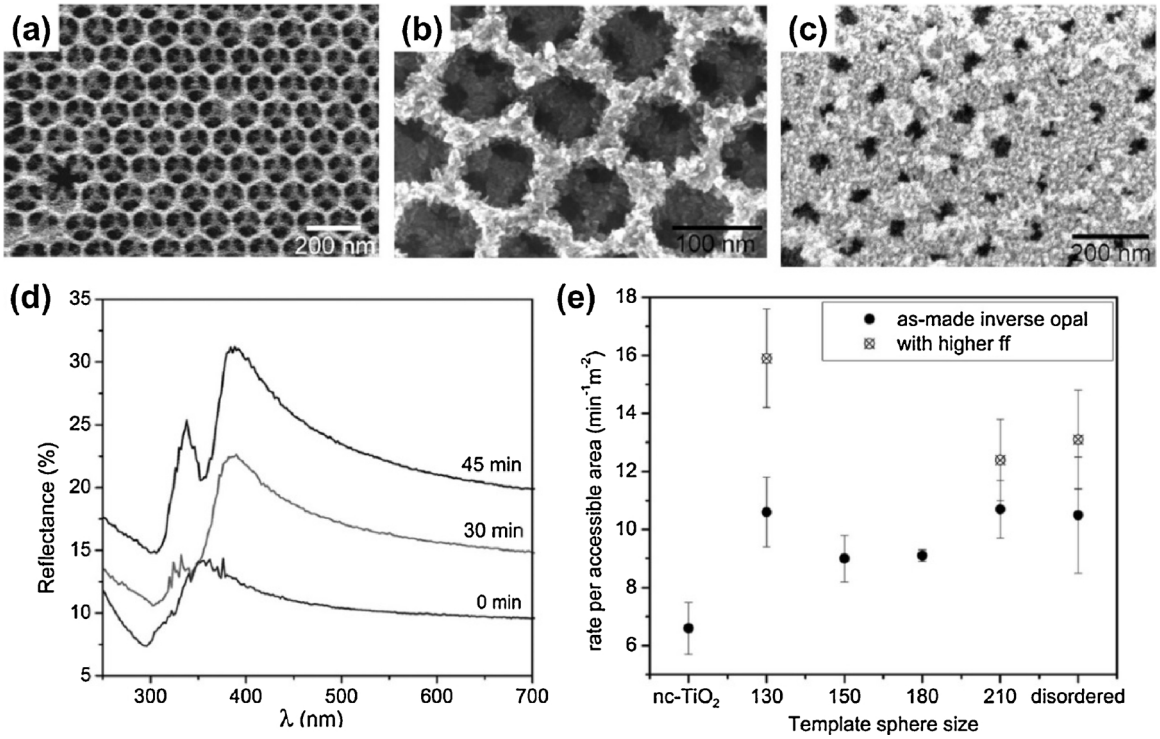

Fig. 13. SEM images of TiO_2 inverse opals (a) as-prepared, and after (b) 30 and (c) 45 min of TiF_6^{-2} treatment. (c) Reflectance spectra (in water) of the TiO_2 inverse opals after variable duration TiF_6^{-2} treatment. (d) Normalized first-order decay rate constants of solution MB photocatalysis of the inverse opals (as-made and after TiF_6^{2-} treatment) in comparison to disordered and nc-TiO_2 films [106]. Copyright © 2009 The Royal Society of Chemistry.

crystallinity or molecular diffusion.

Firm evidence for slow photon effects in aqueous phase TiO_2 photocatalysis under UV band gap excitation were recently provided by systematic investigations of Su et al. [112,113] on the correlation between morphological, structural and optical properties of TiO_2 inverse opal films and their photocatalytic activity on the degradation of RhB aqueous solutions under broadband UV–vis (250–800 nm) irradiation. Specifically, the titania photonic films' stop band was varied in 250 nm PS opal templates by calcination in the range of 550–1000 °C together with angle-dependent (incidence angles of 0, 20 and 45°) photocatalytic experiments, as shown by representative SEM images in Fig. 14(a)–(c) and angle dependent reflectance spectra [Fig. 14(d)–(f)]. The best photocatalytic performance was obtained for the inverse opal films calcined at 700 °C (185 nm void diameter) with stop band reflection at 425 nm under normal incidence [Fig. 14(g)], followed closely by films calcined at 500 and 800 °C with 195 and 165 nm void diameters, respectively, for light incidence at angles of 20 and 45° presenting stop bands at 430 and 366 nm, respectively. Significant slow photon enhancement was evidenced when either the red or even the blue edge of the L-pseudogap matched the films' electronic absorption edge at 396 nm, challenging common consensus that light confinement and slow photons at the high RI skeleton of the TiO_2 inverse opals i.e. the red edge of the stop band are most relevant for enhanced light harvesting.

This was further corroborated by recent theoretical analysis [114] revealing that although slow photons under blue edge tuning are mostly concentrated in the low dielectric part of the inverse opal (air voids), the corresponding field intensity overlaps appreciably the TiO_2 skeleton due to its extremely small, sub-wavelength wall thickness leading to resonantly enhanced modes that may cause even higher enhancement factors than the red edge.

Slow photon amplification has been further explored on the gas-phase TiO_2 photocatalysis of air pollutants, though to a lesser extent. The first study by Ren et al. [115] showed that coating an inverse opal TiO_2 thin film on a quartz rod that was incorporated in a photocatalytic gas reactor afforded a 248% enhancement of the degradation rate for 1,2-dichlorobenzene under UVA (300–380 nm) irradiation (the photonic stop band was identified at ~350 nm) with respect to highly reactive P25 coatings. Later, Jovic et al. [93] provided a systematic study of gas-phase ethanol oxidation under UV light using a series of powder TiO_2 inverse opals fabricated from monodisperse PMMA colloidal templates with well defined optical properties according to both transmittance/reflectance measurements and photonic band structure calculations yielding stop bands within the UV–vis range (280–690 nm), as shown in Fig. 15(a). In that case, a two-fold enhancement of the ethanol photo-oxidation rate was recorded for the inverse opal with L-pseudogap at 345 nm due to the favorable overlap of the slow photon regime with titania's (anatase) absorption edge [Fig. 15(b)], despite the random orientation of the powder sample that reduces the fraction of properly oriented (111) domains with respect to the incident beam. On the other hand, very recent experiments on the gas phase photocatalytic degradation of acetaldehyde under UV irradiation (365 nm) and ISO standard conditions by Curti et al. [116] revealed practically constant photonic efficiencies for different TiO_2 inverse opal films with void diameters of 124, 196 and 264 nm and stop bands below 400 nm in air. The contribution of confined diffusion and size dependent transport of the pollutant molecules within the interconnected inverse opal network [63,117] was concluded as major factors underlying the photocatalytic process especially in aqueous systems with respect to gaseous ones, which has been barely investigated thus far.

Inspired by the application of photonic crystals as dielectric mirrors for mesoporous titania photoelectrodes in dye sensitized solar cells [94,96,97], Chen et al. investigated bilayer structures consisting of SnO_2 inverse opals coated with a nc-TiO_2 thin film as the photocatalytically active layer, as shown in Fig. 16(a), thereby spatially separating light harvesting from the photocatalytic process [118,119]. Tin oxide was selected due to its large electronic band gap (3.8 eV) rendering it transparent over a sufficient spectral range for TiO_2 electronic band gap excitation (≥3.2 eV).

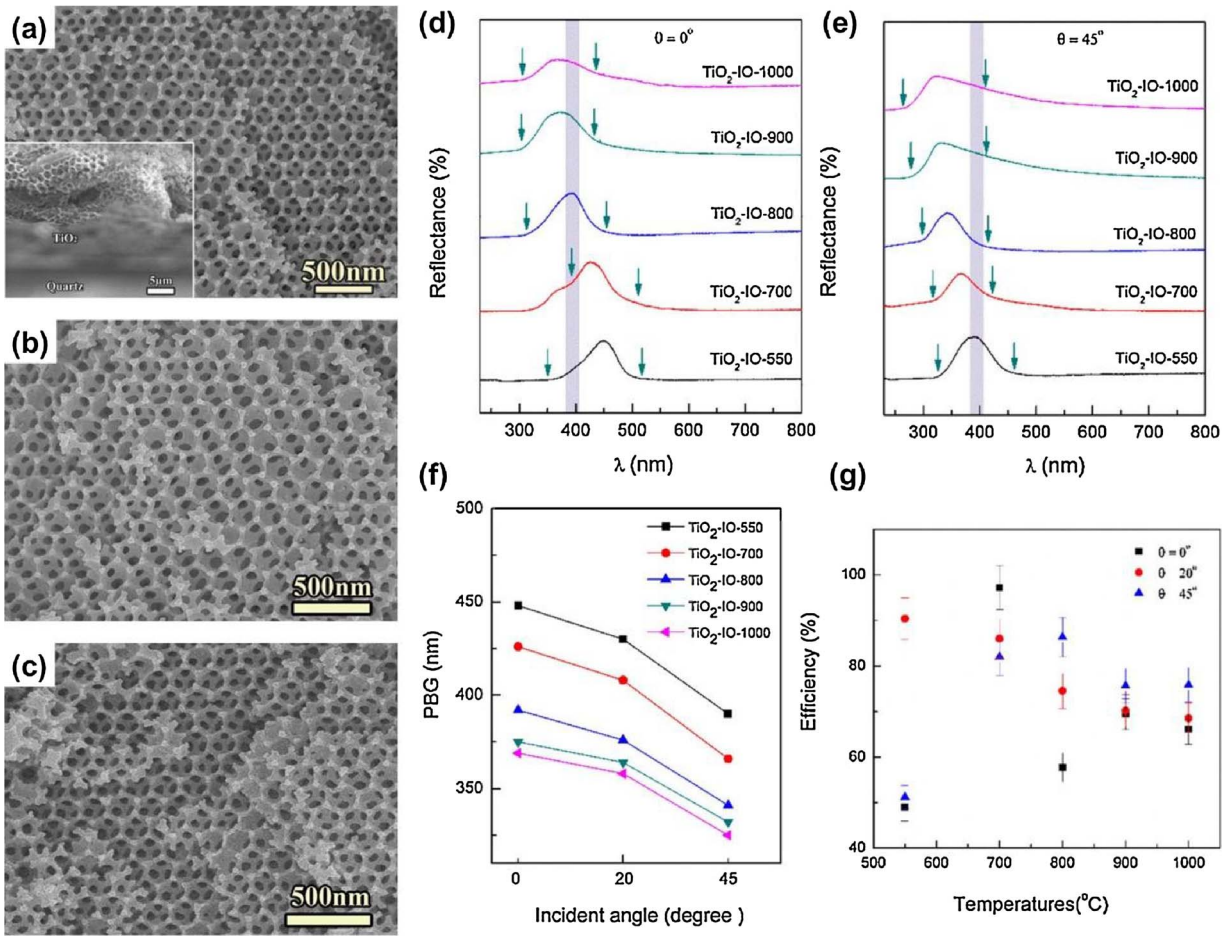

Fig. 14. SEM images of TiO_2 inverse opals (TiO_2-IO) calcined at (a) 550, (b) 700 and (c) 900 °C. Reflectance spectra of the TiO_2-IO films in water at light incidence angles of (c) 0° and (d) 45°. (e) Stop band and (f) RhB photodegradation efficiency variation with calcination temperature and light incidence angles [113]. Copyright © 2013 Elsevier B.V.

Comparative performance evaluation of composite ≈1 μm thick nc-TiO_2/SnO_2 inverse opal films was performed for three different inverse opal underlayers with stop bands at 370, 415 and 525 nm [Fig. 16(b)] as well as plain nanocrystalline and inverse opal TiO_2 films on the solid state photodegradation of RhB under UV–vis light. Best results were obtained for the composites whose stop band reflection matched the onset of the TiO_2 electronic absorption at 370 nm [Fig. 16(c)], indicative of photonic backscattering at the TiO_2/SnO_2 interface that leads to the excitation of localized resonant modes within the absorbing TiO_2 coating [97]. More recently, the influence of the underlayer photonic crystal thickness and its spatial separation from the photocatalytic TiO_2 coating was thoroughly investigated on bilayers consisting of a thin (~500 nm) nc-TiO_2 coating on SiO_2 opal films of 188 nm diameter [120]. In the former case, controlling the thickness of the silica opals from 6 to 48 layers, as shown in Fig. 16(d), resulted in continuous increase of stop band reflectance at 380 nm toward saturation above 35 layers [Fig. 16(e)], where the L-pseudogap of the opal structure fully develops approaching the infinite crystal limit [102]. This resulted in an analogous increase of the photocatalytic efficiency reaching a two-fold enhancement, evaluated on the gas phase degradation of acetaldehyde under monochromatic UVA illumination at 370 nm [Fig. 17(f)]. On the other hand, introduction of a SiO_2 spacer layer of controlled thickness between the TiO_2 coating and the opal photonic crystal gradually diminished the stop band reflectance and the concomitant photocatalytic enhancement supporting interfacial photon localization up to a critical thickness of 2.9 μm. Further research on the effects of the titania absorbing layer thickness and/or porosity would be of value for the design and development of bilayer photonic structures targeting mainly thin film photocatalytic applications.

Very recently, an unconventional Fabry–Pérot resonator configuration was demonstrated by Eftekhari et al. [121] using a sandwich (trilayer) TiO_2 photonic structure consisting of identical top and bottom titania inverse opal layers with ca. 140 nm pore size and a middle inverse opal with ca.180 nm pores, whose red (R) and blue (B) stop band edges overlapped with the TiO_2 electronic absorption at 380 nm, respectively. This innovative structural design enabled light trapping between the top and bottom layers acting as mirrors (Fig. 17) and promoted interfacial scattering and charge separation that led to marked improvements of the photocatalytic activity and photocurrent intensity over the corresponding single and bilayer structures, corroborating the unprecedented prospects of slow photon management on light harvesting.

Slow photon amplification of heterogeneous photocatalysis has been further pursued for other technologically relevant, wide band gap semiconductors. The most prominent is zinc oxide (ZnO) with an electronic band gap of 3.37 eV, because of its excellent optoelectronic properties [122] and high photocatalytic activity, especially for the degradation of organic dye contaminants [123]. Highly-ordered ZnO inverse opals have been fabricated by the auto-forced impregnation of zinc nitrate water-ethanol solutions in colloidal templates of carboxyl modified PS (270, 295 and 351 nm) by Meng et al. [124] and poly (styrene-methyl methacrylate-3-sulfopropyl methacrylate potassium), P (St-MMA-SPMAP) (260 and 470 nm) spheres by Liu et al. [125] exhibiting well defined stop bands in the UV–vis range, depending on the pore diameter and the inverse opal filling fraction. Aqueous phase photocatalytic evaluation under broadband UV–vis illumination (250–800 nm), showed, in the former work, the best performance for the 351 nm templated ZnO inverse opal (stop band at 530 nm) for both

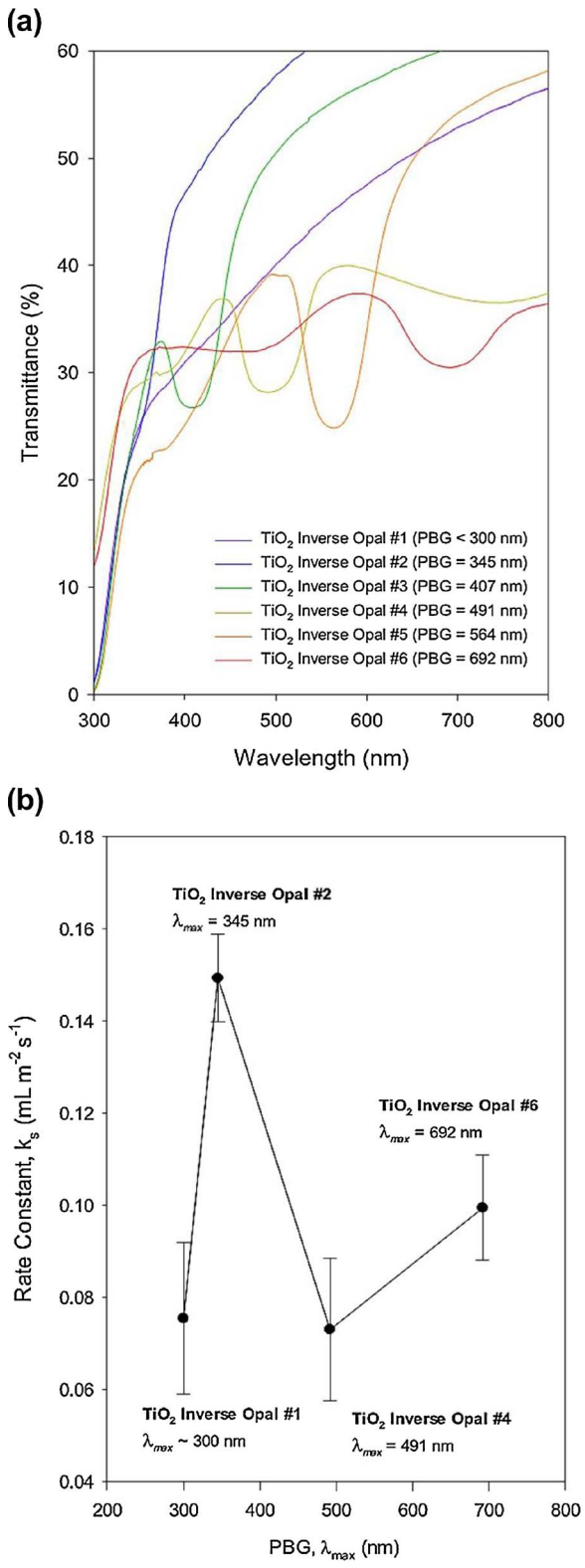

Fig. 15. (a) Transmittance spectra for the TiO_2 inverse opals powder samples along the [111] direction in air. (b) Normalized ethanol photo-oxidation rate constants with respect to the photocatalysts surface area vs stop band position [93]. Copyright © 2016 Elsevier B.V.

colored (MO) and colorless 4-chlorophenol (4-CP) photodegradation compared to porous and nanoparticulate ZnO reference films, whereas, in the latter work, the highest photocatalytic activity was detected for the 470 nm templated ZnO inverse opal (first and second order stop band Bragg reflections at 815 and 423 nm, respectively) for RhB degradation at 40° incidence angle of the irradiation beam. In that case, first evidence for the slow photon effect were provided by angle dependent measurements that allowed identifying the overlap of the red edge of the second order stop band reflection with ZnO's electronic absorption edge. Moreover, ZnO inverse opals exhibited a distinct photo-induced surface wettability conversion (from superhydrophobic to hydrophilic) under UV–vis illumination that is most favorable for the pollutant adsorption to the photocatalytic surface [125] as well as a marked inhibition of ZnO photocorrosion [124] that greatly impedes its application in aqueous phase photocatalysis. Relying on electron spin resonance (ESR) spin trap experiments under UV–vis light and photoelectrochemical (PEC) measurements [124], the high photostability of the ZnO inverse opals was attributed to the enhanced reactivity and transfer of photoinduced carriers to the solution, in agreement with previous photoelectrochemical study of TiO_2 inverse opals indicating faster electron transfer to the oxygen present in the aqueous solution [126]. In addition, wider band gap semiconductors, namely β-Ga_2O_3 and ternary oxide $ZnGa_2O_4$ photonic crystals were successfully fabricated by Li and coworkers [127,128] and were explored as efficient photocatalysts under UVC irradiation. In particular, inverse opal films of β-Ga_2O_3 and $ZnGa_2O_4$ were prepared from colloidal PS opals impregnated by acetylacetone-complexed metal ion precursors with electronic band gap energies of 4.8 and 4.2 eV (270 and 298 nm, respectively) and variable void sphere sizes of 135, 179, 258, and 288 nm for β-Ga_2O_3 and 145, 180, 225 and 280 nm for $ZnGa_2O_4$, resulting in tunable stop band reflections at 260, 290, 425, 500 nm and 295, 390, 470 590 nm [Fig. 18(a)], respectively.

Systematic photocatalytic activity tests were carried out in the aqueous phase on the degradation of MO, RhB and benzoic acid (BA) for β-Ga_2O_3 and MO for $ZnGa_2O_4$ under UVC irradiation at 254 nm. Slow photon enhancement was identified at the red edge of the β-Ga_2O_3 inverse opals with stop band at 260 nm, whereas blue edge slow photon amplification was detected for $ZnGa_2O_4$ with stop band reflection at 390 nm, leading to the highest photocatalytic reaction rates that were also found to be comparable or even higher than the benchmark P25 films, as shown in Fig. 18(b).

4. Slow photon-assisted TiO_2 photocatalysis under visible light

Although further work may be in order to unveil the interplay of slow photons with light scattering, porosity and surface area effects, the presented results (Table 1) provide ample evidence for the amplification effect of photonic crystals on titania's and other wide band gap semiconductors photocatalytic performance under UV band gap excitation. The fundamental mechanism relies on the optimal overlap of the slow photon energy with the spectral region, where the photocatalyst' absorbance and light-matter interactions are to be enhanced, while avoiding stop band reflection losses most prominent under broadband UV–vis irradiation required for most practical applications. This operation principle has been further explored to enhance VLA photocatalysis by photonic crystal structuring in combination with the different strategies that are being applied to extend titania's photocatalytic response under visible light. Recent progress in this field is reviewed in the following section and relevant works are summarized in Table 2.

4.1. Dye sensitization

Dye sensitization has been one of the most established and efficient strategies to induce visible light activated TiO_2 photocatalysis [129,130]. The process involves photon absorption under visible-light irradiation by "sensitizer" molecules grafted on the semiconductor surface, commonly organic dyes or transition metal complexes, followed by the fast electron injection from the dye excited state to the lower lying conduction band of TiO_2, which in the presence of a

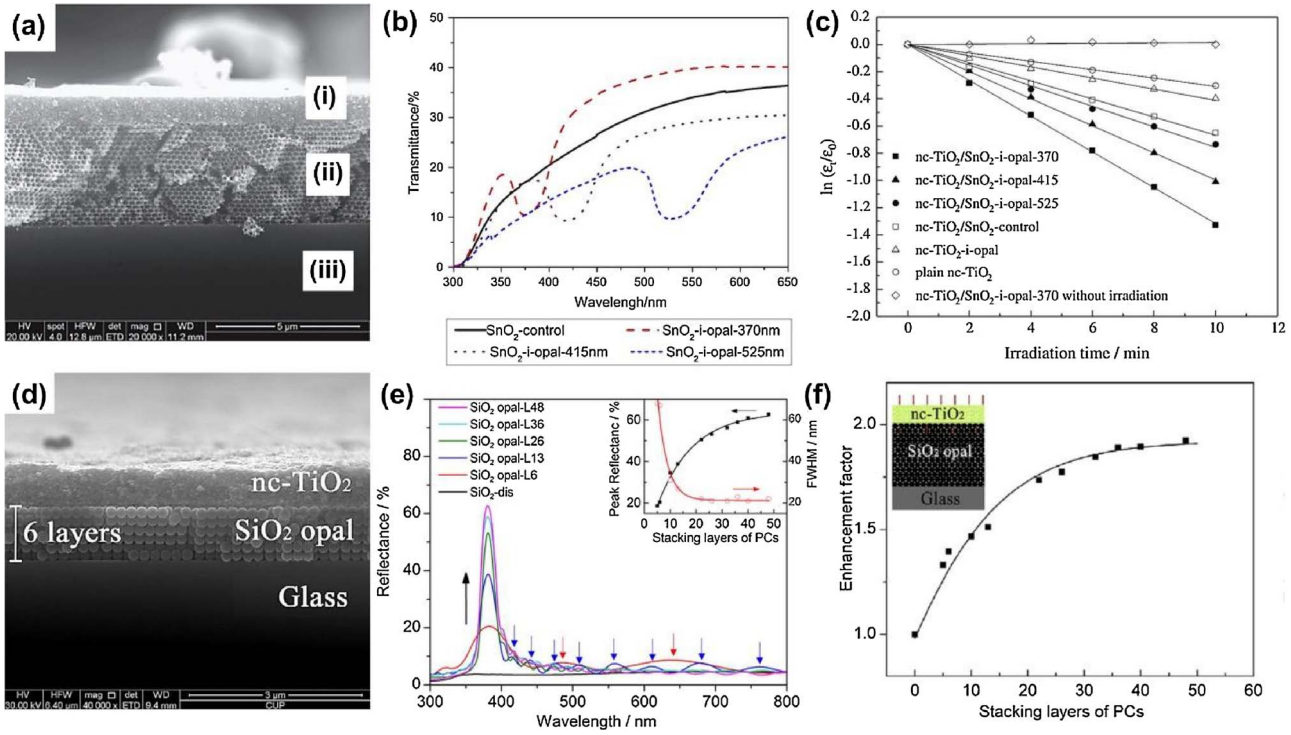

Fig. 16. (a) Cross section SEM image of nc-TiO_2/SnO_2 inverse opal. Roman letters (i), (ii) and (iii) designate the nc-TiO_2, SnO_2 and quartz layers, respectively. (b) Transmittance of the SnO_2 inverse opals compared with a disordered porous film. (c) Photocatalytic RhB degradation kinetics in comparison to inverse opal and nc-TiO_2 films [119]. (d) Cross section SEM image of a thin nc-TiO_2 film on 6 layer thick SiO_2 opal. (e) Reflectance spectra of SiO_2 opals with increasing layers (arrows indicate Fabry–Perot fringes). The inset shows the variation of the stop band intensity and width with the number of stacking layers. (f) Photocatalytic enhancement factor as a function of the SiO_2 stacking layers [120]. Copyright © 2014–2015 Elsevier B.V.

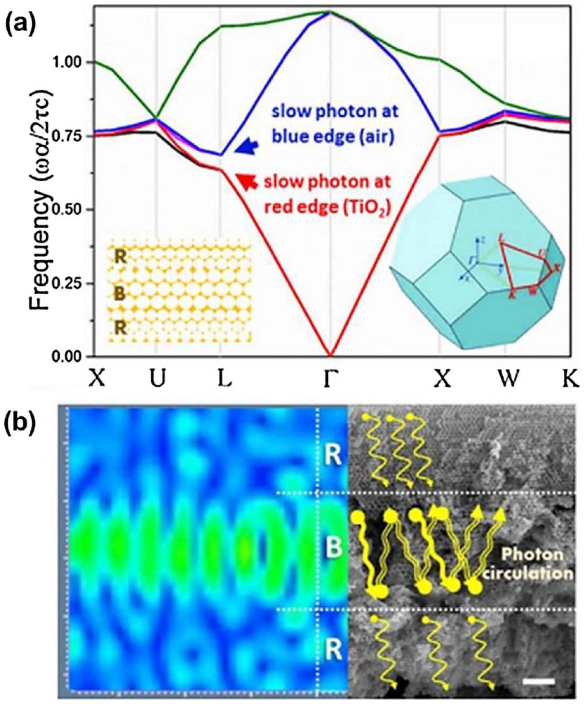

Fig. 17. (a) Photonic band structure of the sandwich-structured R-B-R inverse opal, whose red (R) and blue (B) stop band edges overlapped with the TiO_2 electronic absorption. (b) Simulated electric field intensity pattern and schematic of slow photon circulation superimposed on the cross sectional SEM image of the trilayer photonic film [121]. Copyright © 2017 The Royal Society of Chemistry.

suitable regenerating redox couple has been prolifically exploited in the dye sensitized solar cells technology [131]. In the absence of regeneration, the sensitizer itself undergoes oxidative degradation, a process widely applied for the self-sensitized degradation of colored water pollutants, especially textile dyes, on titania's or other semiconductors surface [132]. The self-sensitized photocatalytic oxidation is based on the scavenging of TiO_2 conduction band electrons by O_2 molecules in the reaction medium, inducing the formation of reactive oxygen species (ROS) such as superoxide or hydroperoxide radicals, which in turn attack on-site the dye molecules, degrading them to non-toxic, harmless end products.

Slow photon amplification in dye sensitized TiO_2 photocatalysis under visible light has been thoroughly investigated by Li and coworkers for both TiO_2 [78] and ZnO [133] inverse opal films, as shown in Fig. 19. Highly ordered TiO_2 inverse opals, designated as T270, T340, T460 and T550 after the PS sphere diameters used in the colloidal templates, with tailored stop bands in the visible range (Fig. 5) were fabricated and their reactivity was evaluated in aqueous phase photocatalysis selecting four different probe molecules, i.e. the MO, RhB and MB dyes along with the non-colored BA, as target pollutants of different sensitizing ability, under both UV–vis ($320 < \lambda < 800$ nm) and visible ($420 < \lambda < 800$ nm) light. Matching the stop bands of the TiO_2 photonic films (430, 550, 660 and 910 nm in water for the T270, T340, T460 and T550 films, respectively) to the dye absorption bands [Fig. 19(a) and (c)] resulted in a distinct rise of the photodegradation rates under both visible [Fig. 19(b)] and UV–vis [Fig. 19(d)] light, compared to the corresponding ones over BA degradation or those obtained under UV light ($320 < \lambda < 400$ nm) lacking any photonic effects. In the latter case, the UV activity followed closely the pore size increment of the inverse opals that enhances mass transfer of pollutant molecules. Slow photon effects were clearly verified by visible light photocatalytic tests, where the T340 and T460 inverse opals presented the best performances on the degradation of the cationic RhB and MB dyes that adsorb strongly to the negatively charged TiO_2 surface, in contrast to the weakly adsorbing anionic MO dye and the non-visible

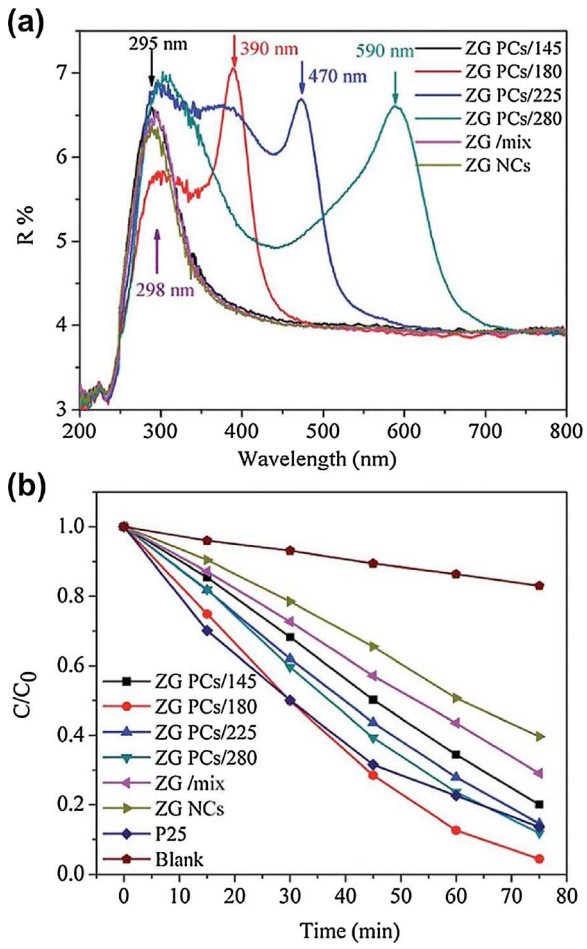

Fig. 18. (a) Reflectane spectra of the $ZnGa_2O_4$ photonic crystals (ZG PCs) of 145, 180, 225 and 280 nm pore diameters. (b) Photocatalytic activities of the $ZnGa_2O_4$ inverse opals on MO degradation under UVC irradiation of 254 nm [128]. Copyright © 2014 The Royal Society of Chemistry.

light absorbing BA molecules that do not qualify for the dye sensitized photocatalytic mechanism. Slow photons at both the red- (primarily localized on the TiO_2 skeleton) and blue- (mainly localized in air) edges of the stop bands appeared to amplify the photocatalytic degradation of the dye molecules grafted at the interface of the high (TiO_2) and low (air) dielectric media, similar to the slow photon amplification of photo-isomerization of azobenzene [134] anchored on silica opals [135].

Similar results were obtained on ZnO inverse opal films with tuned stop band reflections in the visible range at 510, 600 and 720 nm in water, whose photocatalytic activity was evaluated in the aqueous phase photodegrdadation of the MO, RhB and MB dyes in comparison with 4-CP under UV–vis and visible light. Slow photon effects were likewise identified for the visible light self-degradation of the RhB and MB dyes, though at different footings for the red and blue-stop band edges rationalized by the different adsorption capacity of the two dyes [133]. Substantial enhancement of the dye photodegradation activity was earlier demonstrated by Li et al. [136] for 3D ordered TiO_2 hollow-sphere films with stop bands tuned by the template PS sphere diameter and the titania shell thickness from 547 to 930 nm. In that case, the optical absorbance and solid state photodegradation of crystal violet (CV) under visible and solar light were significantly increased for the photonic films, whose stop band red edge approached the dye absorption peak further assisted by multiple scattering effects in the periodic structure. The optimal titania inverse opals for RhB degradation (Fig. 19) fabricated by the 340 nm PS sphere template [78] were later exploited for the solar light photoelectrocatalytic RhB removal [137]. Under an appropriate bias that assists electron-hole separation, the TiO_2 inverse opal films deposited on conductive FTO glass substrates presented a marked enhancement of the RhB degradation rate compared to plain photocatalysis (ca. four-fold increase). Systematic experiments on ROS determination by active scavengers, ESR spin trapping and OH-trapping photoluminescence indicated that photogenerated electron transfer to the Pt electrode under the action of the electric field promoted the formation of superoxide $\cdot O_2^-$ radicals compared to the photocatalytic process for RhB decomposition as schematically shown in Fig. 20, leading to a large enhancement factor of ~3.1 over non-structured nc-TiO_2 films (Table 2).

Very recently, direct evidence for slow photons that amplify the interaction of visible light with the adsorbed dye molecules were provided by Toumazatou et al. [71] comparing the solid state MB photodegradation under UVA and monochromatic laser light on PBG engineered TiO_2 inverse opal films with stop band at 450 nm by micro-Raman spectroscopy (Fig. 21). In contrast to UVA, where no photonic effect could be traced, significant enhancement of visible light-induced MB sensitized TiO_2 photocatalysis was evidenced under monochromatic light of 514 nm due to red edge slow photons, outperforming (five-fold increase) the benchmark mesoporous Aeroxide® P25 TiO_2 films (Fig. 21).

This was corroborated by a systematic study of Curti et al. [116] on the photocatalytic degradation of MB aqueous solutions under monochromatic royal blue LED (450 ± 10 nm) illumination in TiO_2 inverse opals with long-range ordered (111) domains prepared by the capillary deposition method of PS templates with 124, 196, and 264 nm sphere diameters. Controlling the photonic films stop band reflection by varying the lattice parameter and irradiation incident angle allowed discriminating the amplification effect of the red edge stop band tail on MB self-degradation, though consecutive photocatalytic degradation cycles indicated rather poor mechanical stability of the inverse opal films, possibly caused by the light induced particle de-aggregation effect [138].

4.2. Non metal and self-doping

Doping and more recently co-doping of TiO_2 by non-metal elements (N, C, F, S etc), especially nitrogen, has been established as one of the most competent methods for the development of efficient VLA TiO_2 photocatalysts relying on titania's chemical modification [12]. Among non-metals dopants, nitrogen and its combinations with other elements has been attracting most interest from both fundamental and applied perspective regarding VLA photocatalytic applications [13]. Structuring nitrogen doped TiO_2 in the form of inverse opals was first investigated by Li and Shang in 2008 [139], as a promising means to enhance its relatively poor visible light absorbance that is the major limitation for such catalysts. N-TiO_2 inverse opal films were prepared by infiltration of 400 nm PS opal templates using tetramethylammonium hydroxide as nitrogen source in the sol-gel precursor. A stop band at 540–600 nm was identified by reflectance and transmittance measurements, leading to substantial improvements of the MB degradation rates under visible light, namely ~68% compared to non-structured sol-gel N-TiO_2 films and ~26% over mixed inverse opals, attributed to N-doping together with photonic structure effects. However, slow photon effects on the N-TiO_2 absorption edge could not be discriminated from those on the MB dye absorption band, according to the dye sensitization mechanism discussed in the preceding section. Advanced fabrication of ordered arrays of N-doped mesoporous titania spheres [140] and more recently N-doped TiO_2 mesoporous inverse opals [141] were implemented based on the combination of PMMA inverse opal with Pluronic P123 copolymer templates and sub-100 nm PS colloidal crystal templates, respectively. These structures afforded significant improvements on visible light dye photodegradation over their undoped or unstructured analogues, though identification of stop band formation and its interplay with surface area, molecular transfer and/or multiple scattering

Table 2
Visible light activated photonic crystal photocatalysts and their application in the degradation of organic pollutants and water splitting.

Photonic crystal	Pore template	Photocatalytic application	Irradiation conditions	Performance	Ref.
TiO_2 io films	270, 340, 460, 550 nm PS opals	Water pollutant degradation BA, MO, RhB, MB (aq)	500 W Xe Vis (420–800 nm) UV (320–400 nm) UV–vis (320–800 nm)	(MO) $EF_{UV-vis} \sim 2.1$ (RhB) $EF_{UV-vis} \sim 1.8$ $EF_{vis} \sim 2.7$ (MB) $EF_{UV-vis} \sim 1.6$ $EF_{vis} \sim 2.1$	[78]
ZnO io films	270, 300, 350 nm PS opals	Water pollutant degradation MO, RhB, MB, 4-CP (aq)	500 W Xe Vis (420–800 nm) UV (320–400 nm)	(RhB) $EF_{vis} \sim 1.9$ (MB) $EF_{vis} \sim 1.7$	[133]
TiO_2 hollow-sphere films	202, 356, 548 nm PS opals	Water pollutant degradation CV (s)	Solar AM 1.5 $\lambda > 400$ nm	EF ~ 1.22 vs nc TiO_2	
TiO_2 io films	350 nm PS opals	Photoelectrocatalytic RhB degradation (aq)	500 W Xe 320–800 nm	EF ~ 3.1 vs nc TiO_2	[137]
TiO_2 io films	350 nm PS opals	Water pollutant degradation MB (s)	Laser diode 514 nm Micro-Raman detection	(io) 0.112(4) min^{-1} (P25) 0.023(2) min^{-1} EF ~ 5.0	[71]
TiO_2 io films	124, 196, 264 nm PS opals	Water pollutant degradation MB (aq)	Royal blue LED 3 W, 450(10) nm	EF ~ 1.2 vs dis-TiO_2	[116]
N-TiO_2 io films	400 nm PS opal	Water pollutant degradation MB (aq)	Halogen lamp $\lambda > 400$ nm	EF ~ 1.7 vs nc-TiO_2 EF ~ 1.26 vs dis-TiO_2	[139]
Mesoporous N-TiO_2 spheres	290 nm silica opal, PMMA inverse opal, Pluronic P123	Water pollutant degradation RhB (aq)	300 W Xe lamp $\lambda > 400$ nm	EF ~ 4.0 vs meso-TiO_2 spheres EF ~ 2.0 vs N-TiO_2 spheres	[140]
Mesoporous N-TiO_2 io films	80 and 300 nm PS opals	Water pollutant degradation MB (aq)	Xe lamp AM 1.5G 100 mW cm^{-2} (400–600 nm)	EF ~ 4.9 vs meso TiO_2 io EF ~ 1.8 vs macro-TiO_2 io	[141]
N-TiO_2 io films	Co-assembly 450 nm PS spheres and TiBALDH	Water pollutant degradation MB and TC (aq)	300 W Xe lamp $\lambda > 400$ nm	(MB) EF ~ 13.9 (TC) EF ~ 6.1 vs conventional TiO_2 io	[142]
Meso-macroporous NF-TiO_2 io films	201, 228, 315 nm silica spheres, LPD	Water pollutant degradation MB (aq)	20 W fluorescent lamp (400–760 nm) 20 W UV lamp (254 nm)	$EF_{vis} \sim 7.4$ vs porous NF-TiO_2 $EF_{vis} \sim 1.1$ vs dis-NF-TiO_2 io	[143]
NF-TiO_2 io films	215 and 460 nm PS opals	Water pollutant degradation RhB (s)	Xe lamp, AM 1.5G Natural sunlight	EF ~ 1.6 vs nc NF-TiO_2 (direct solar)	[145]
Ti^{3+} doped TiO_2 io films-powders	170, 265, 355 nm PS opals	Water pollutant degradation AO7 (aq)	500 W halogen lamp Hg lamp	EF ~ 2.5 vs TiO_2 io EF ~ 3.0 vs V-TiO_2	[146]
"Black" hydrogenated TiO_2 io films	360 nm PS opals, 2 h under H_2 at 500 °C	Water pollutant degradation MB (aq)	300 W Xe lamp $\lambda > 400$ nm	EF ~ 1.35 vs white TiO_2 io) EF ~ 2.0 vs P25 films	[147]
Pt-TiO_2 io films	185 nm PS opals	Water pollutant degradation AO7 (s)	120 W Xe $\lambda > 300$ nm	EF = 3.5-4.0 > 2 wt % Pt	[149]
Cu-TiO_2 io coatings	120 nm PS opals on quartz fibers	CO_2 conversion to CH_3OH	500 W lamp (310–380 nm)	EF ~ 13.5 vs nc Cu-TiO_2	[150]
TiO_2/Pt io films on Ti	120, 140, 193, 225 nm PS opals	Water pollutant degradation phenol (aq)	300 W Hg lamp 365 nm, 2.0 mW cm^{-2}	EF ~ 3.3 vs nc-TiO_2 EF ~ 1.5 vs mixed TiO_2/Pt	[151]
Pt-TiO_2 io films-powders	180, 190, 210, 240, 420 nm P(St-MMA-AA) opals	PEC water splitting H_2 generation 20% (v/v) CH_3OH	300 W Xe lamp	EF ~ 2.5 vs nc Pt-TiO_2 Quantum yield QY = 11.9%	[152]
Pt-TiO_2 io powders	PS and PMMA opals	PEC water splitting H_2 generation 0.1 M HCOONa	UVA 365 nm 78 W m^{-2} UVC 254 nm, 2.3 W	EF ~ 2.0 at 365 nm vs mesoporous Pt-TiO_2	[153]
Au-TiO_2 io powders	235 and 372 nm PMMA opals	PEC water splitting H_2 generation 0.5 vol % CH_3CH_2OH	100 W UV 1–1.2 mW cm – 2 Sunlight 0.3–0.4 mW cm – 2	EF ~ 5.0 vs nc Au-TiO_2	[154]
Au-TiO_2 io films	Co-assembly 170 225, 257, 326, 398 nm PS, $HAuCl_4$, TiBALDH	Water pollutant degradation BA (aq)	300 W Hg lamp (340 nm)	EF ~ 5.4 vs nc-TiO_2 EF ~ 2.0 vs TiO_2 io	[155]
Au-TiO_2 io films	193 and 240 nm PS opals	Water pollutant degradation 2,4-DCP (aq)	500 W Xe lamp $\lambda > 420$ nm 100 mW cm^{-2}	EF ~ 2.3 vs Au-nc TiO_2 EF ~ 3.0 vs TiO_2 io	[159]
Au-TiO_2 io films	130, 350, 600 nm PS PEO-PPO-PEO triblock copolymer	PEC water splitting H_2 generation Photocurrent-IPCE 0.24 M Na_2S/0.35 M Na_2SO_3	Solar simulator AM 1.5 G	EF ~ 2.9 vs TiO_2 io 0.8 mA cm^{-2} at 0.5 V vs Ag/AgCl	[160]
Bilayer Au TiO_2 io-rutile nanorod (NR) arrays	260, ~300, 360 nm PS opals	PEC water splitting H_2 generation 1 M KOH aqueous solution (pH = 13.5)	300 W Xe lamp AM 1.5 G 100 mW cm^{-2} $\lambda > 420$ nm	η = 0.71% at 0.64 V vs. RHE 0.47 mA cm^{-2} $\lambda > 420$ nm, EF ~ 2.0	[161]
Ag-TiO_2 io films	315 nm SiO_2 spheres	Water pollutant degradation MB (aq)	UV 254 nm Vis 400–760 nm	$EF_{UV} \sim 1.5$ $EF_{Vis} \sim 4.5$	[162]
Au-ZnO io films	182, 222, and 277 nm carboxyl-modified PS	Water pollutant degradation RhB and 4-CP (aq)	500 W Xe lamp $\lambda > 420$ nm	$EF_{RhB} \sim 5.6$ vs N-TiO_2 $EF_{RhB} \sim 2.8$ $EF_{4-CP} \sim 4.2$ vs Au/ZnO porous	[163]

(*continued on next page*)

Table 2 (*continued*)

Photonic crystal	Pore template	Photocatalytic application	Irradiation conditions	Performance	Ref.
CdS-TiO_2 io films	288, 510, and 900 nm PS opals	PEC water splitting Photocurrent-IPCE 0.25 M Na_2S/0.35 M Na_2SO_3 pH = 9.5	150 W Xe lamp AM 1.5 G 100 mW cm^{-2}	4.84 mA cm^{-2} at 0 V vs Ag/AgCl η = 2.62%, IPCE ~30% (288 PS)	[164]
CdS-Au-TiO_2 io powder	PS opals	PEC water splitting H_2 generation 0.1 M Na_2S/0.1 M Na_2SO_3	300 W Xe 420–780 nm (158 mW cm^{-2})	EF ~ 1.3 vs nc CdS-Au-TiO_2 EF ~ 10 vs io CdS-TiO_2	[165]
CdSe/CdS-TiO_2 mesoporous io films	99 nm PS opals	PEC water splitting Photocurrent-IPCE 0.25 M Na_2S/0.35 M Na_2SO_3 pH = 9.5	150 W Xe lamp AM 1.5 G 100 mW cm^{-2}	13.67 mA cm^{-2} at 0 V vs Ag/AgCl EF ~ 2.3 vs CdSe/CdS-TiO_2 macro-io	[166]
CdS-ZrO_2 io powders	260, 400, 430, 500 nm PS opals	PEC water splitting H_2 generation 0.25 M Na_2S/0.35 M Na_2SO_3	300 W Xe lamp 900 mW cm^{-2} > 400 nm	1083 μmol g^{-1} h^{-1} EF ~ 4.7 vs non-io CdS-ZrO_2	[167]
CdS-SnO_2 io films	190 nm PS opals	Water pollutant degradation CBZ (aq) 0.6 V (vs. SCE) Photocurrent- η 0.1 M Na_2SO_4	300 W Xe lamp 420–600 nm 2 mW cm^{-2}	η = 11.8% at 0.6 V vs SCE EF ~ 16.8 vs SnO_2 film k_{CBZ} = 4.04 × 10^{-4} s^{-1} EF_{CBZ} ~ 54 vs SnO_2 film	[168]
CdS-Au- ZnO io films	~300 nm PS opals	PEC water splitting Photocurrent-IPCE 0.25 M Na_2S/0.35 Na_2SO_3 pH = 12	150 W Xe lamp AM 1.5 G 100 mW cm^{-2}	5.7 mA cm^{-2} at 0 V vs Ag/AgCl EF ~ 6.7 vs Au-ZnO io EF ~ 2.3 vs CdS-ZnO io	[169]
CdS-Au-$SrTiO_3$ io powders	200, 300, 400 nm PMMA opals	PEC water splitting H_2 generation 0.1 M Na_2S/0.1 M Na_2SO_3	300 W Xe λ > 420 nm	5.46 mmol g^{-1} h^{-1} Apparent QE = 42.2% at 420 nm after Pt deposition	[170]
Cu_2O-TiO_2 io films	260 and 193 nm PS opals	Water pollutant RhB and BPA degradation (aq)	300 W Xe 320–780 nm 200 mW cm^{-2}	EF_{RhB} ~ 2.9, EF_{BPA} ~ 4.9 vs Cu_2O-TiO_2 NP	[172]
ZnO-TiO_2 io films	300 nm PS opals	Water pollutant MO degradation (aq)	500 W Xe 320–800 nm	EF ~ 1.9 vs ZnO-TiO_2 NP	[173]
ZnO QDs-TiO_2 io powder	370 nm PS opals	Water pollutant RhB degradation (aq)	18 W Ne lamp λ < 400 nm	EF ~ 2.1 vs TiO_2 io EF ~ 1.8 vs ZnO-TiO_2 EF ~ 5.7 vs P25	[174]
CdS-ZnO nanowires-TiO_2 io films	200, 250, 288 nm carboxylate modified PS opals	PEC water splitting Photocurrent-IPCE 0.25 M Na_2S/0.35 M Na_2SO_3	150 W Xe lamp AM 1.5 G 100 mW cm^{-2}	5 mA cm^{-2} at +0.75 V vs Ag/AgCl	[175]
rGO-TiO_2 io films	240 and 300 nm PS opals, Pluronic P123	Water pollutant MB degradation (aq)	24 W UV lamp 365 nm	EF ~ 15 vs meso rGO-TiO_2 EF = 1.6–2.0 vs TiO_2-io	[180]
α-Fe_2O_3/graphene io films	350 nm PS opals	PEC water splitting Photocurrent-IPCE 1.0 M NaOH	Simulated solar AM 1.5 G	1.62 mA cm^{-2} at 1.5 V vs RHE EF ~ 1.4 vs α-Fe_2O_3	[181]
Au-rGO-TiO_2 io films	620 nm PS opals	PEC water splitting Photocurrent-IPCE H_2 generation 0.5 M Na_2SO_4 (pH ≈ 6.5)	Simulated solar AM 1.5 G 100 mW cm^{-2} Visible light λ > 420 nm	1.29 mA cm^{-2} at 1.23 V vs RHE, EF_{solar} ~ 2.1 vs TiO_2 0.3 mA cm^{-2} at 1.23 V vs RHE, EF_{Vis} ~ 14 vs TiO_2 17.8 μmol cm^{-2} EF ~ 2.5 vs TiO_2	[182]
Carbon TiO_2 io films	740 nm PS opals	Water pollutant MB degradation (aq, viscous 0.5 or 1 wt % polyacrylamide) Photocurrent	1000 W Xe lamp AM 1.5 G 100 mW cm^{-2} 495–700 nm	EF ~ 7.86 vs TiO_2 io EF ~ 1.64 vs low C TiO_2 io	[183]
P3HT-TiO_2 NP/io bilayer films	192 and 365 nm PS opals	Water pollutant MB degradation (aq) Photocurrent 0.04 M KHP/0.1 M KSCN	150 W Xe lamp λ > 400 nm, 50 mW/cm^{-2} 500 W Xe lamp 70 mW/cm^{-2}	EF_{MB} ~ 2.08 EF_{ph} ~ 2.76 vs P3HT-TiO_2 NP EF_{MB} ~ 1.76 vs P3HT-dis TiO_2 io	[184]
α-Fe_2O_3 io films	356 nm PS opal	Water pollutant CV degradation (aq) (s)	500 W Xe lamp λ > 400 nm 550(5) nm	EF_{vis} ~ 2.4 $EF_{550\,nm}$ (45°) ~ 1.63 vs α-Fe_2O_3 nc films	[185]
WO_3 io powders	492, 253, 181 and 86 nm PMMA opals	Gaseous acetic acid decomposition (g)	300 W Xe lamp λ > 400 nm	EF ~ 30 vs non-porous WO_3	[186]
WO_3 io films	200, 260 and 360 nm PS opals	Photocurrent-IPCE 0.1 M Na_2SO_4	500 W Xe 300–800 nm 250 mW cm^{-2} λ > 400 nm	EF ~ 2 vs dis porous WO_3	[187]
β-Bi_2O_3 io films	300 and 380 nm PS opals	Water pollutant MO, RhB degradation (aq) Photocurrent 0.1 M Na_2SO_4	500 W Xe lamp 420–800 nm Monochromatic 420–500 nm	EF_{MO} ~ 2.5 EF_{RhB} ~ 1.5 vs porous β-Bi_2O_3	[188]

(*continued on next page*)

Table 2 (*continued*)

Photonic crystal	Pore template	Photocatalytic application	Irradiation conditions	Performance	Ref.
Ag_3PO_4-WO_3 io powders	150, 270, 420 nm PMMA opals	Water pollutant phenol, BPA, RhB, MB, MG degradation (aq) PEC water splitting, O_2 evolution	210 W Xe lamp λ > 420 nm 300 W Xe lamp λ > 420 nm	EF_{RhB} ~ 13 $EF(O_2)$ ~ 1.2 (> 3 h) vs Ag_3PO_4 EF_{RhBl} ~ 6 vs Ag_3PO_4/WO_3 rod	[191]
Ag_3PO_4-Ag-$SrTiO_3$ io powders	200, 300, 400 nm PMMA opals	Water pollutant RhB, MB, phenol degradation (aq) Photocurrent 0.1 M Na_2SO_4	300 W Xe lamp λ > 420 nm	EF_{RhB} ~ 4.33 $EF_{photocurrent}$ ~ 3.0 vs Ag_3PO_4 EF_{RhB} ~ 3.25 vs dis Ag_3PO_4-Ag-$SrTiO_3$	[194]
Bi_2WO_6 io films	460 nm PS opals	Water pollutant MB, SA degradation (aq) PEC water splitting Photocurrent 1 M Na_2SO_4	1000 W Xe lamp λ > 420 nm 100 mW cm^{-2} 450 W Xe lamp λ > 400 nm 15 mW cm^{-2}	EF_{MB} ~ 2.6 EF_{SA} ~ 2.4 vs nc-Bi_2WO_6 η = 0.13% at 0.46 V vs Ag/AgCl, EF ~ 3.2	[196]
Mo-$BiVO_4$ io films	200 nm PS opals	PEC water splitting Photocurrent-IPCE H_2 generation 0.5 M Na_2SO_4 (pH = 6.6)	500 W Xe lamp AM 1.5 G	2.0 mA cm^{-2} at 1 V vs Ag/AgCl EF_{η} ~ 4.1 vs dis-porous Mo:$BiVO_4$ film	[197]
Au-Mo-$BiVO_4$ io films	260 and 320 nm PS opals	PEC water splitting H_2/O_2 generation Photocurrent-IPCE 0.1 M phosphate pH= 7, Co-Pi co-catalyst	150 W Xe lamp AM 1.5 G 100 mW cm^{-2}	3.1 mA cm^{-2} at 1.23 V vs RHE EF ~ 4.1 vs planar Mo-$BiVO_4$	[198]
(Pt, Au, Pd) -AgBr-$BiVO_4$ io powders	300 nm PMMA opals	Water pollutant 4-CP degradation (aq)	300 W Xe lamp λ > 400 nm	Complete 4-CP degradation within 150 min	[200]
Ag-$BiVO_4$ io films	255 nm PS opals	Water pollutant MB degradation (aq) Photocurrent-IPCE 0.1 M Na_2SO_4 pH = 7	300 W Hg lamp λ > 420 nm 300 W Xe lamp λ > 420 nm 100 mW cm^{-2}	EF_{MB} ~ 1.8, EFph ~ 2.4 vs Ag-dis $BiVO_4$ EF_{MB} ~ 2.2, EFph ~ 2.9 vs $BiVO_4$ io	[201]
Carbon QDs- $BiVO_4$ io films	260 nm PS opals	PEC water splitting H_2/O_2 generation Photocurrent-IPCE 0.1 M Na_2SO_4 pH = 7	300 W Xe lamp	η = 0.35% at 0.87 V vs. RHE, EF ~ 5. 18.8 μmol h^{-1} EF ~ 3.2 8vs nc $BiVO_4$ films	[202]
$BiVO_4$-TiO_2 io powders	350 nm PS opals	Water pollutant RhB degradation (aq)	18 W Ne lamp 400–800 nm	EF ~ 4.1 0.08 $BiVO_4$-TiO_2 vs TiO_2 io powders	[203]
$BiVO_4$-TiO_2 io powders	350 nm PS opals	Water pollutant RhB degradation (aq)	18 W Ne lamp 400–800 nm	EF ~ 6.1 0.2 $BiVO_4$-TiO_2 vs TiO_2 io powders	[204]
Cr_2O_3-$InVO_4$ io powders	300 nm PMMA opals	Water pollutant RhB degradation (aq)	300 W Xe lamp λ > 420 nm	99% RhB removal vs 47% for $InVO_4$ io after 200 min of visible-light illumination	[205]
(Au, Ag, Pd, Pt)- $BiVO_4$-$InVO_4$ io powders	300 nm PMMA opals	Water pollutant RhB, MB degradation (aq)	300 W Xe lamp λ > 400 nm	EF_{MB} ~ 2.6 EF_{RhB} ~ 6.9 vs porous $BiVO_4$-$InVO_4$	[206]
$InVO_4$ io powders	300 nm PMMA opals	Water pollutant MB degradation (aq)	300 W Xe lamp λ > 400 nm	98% MB removal vs 24% for bulk $InVO_4$ after 60 min of visible-light illumination	[207]
Fe_2O_3-$BiVO_4$ io powders	300 nm PMMA opals	Water pollutant 4-NP degradation (aq)	300 W Xe lamp λ > 400 nm	EF ~ 4.1 vs $BiVO_4$ io powder	[208]
Al-doped ZnO- $BiVO_4$ io films	320 nm PS opals	PEC water splitting Photocurrent-IPCE 0.1 M phosphate pH = 7	150 W Xe lamp AM 1.5 G 100 mW cm^{-2}	1.5 mA cm^{-2} at 1.23 V vs. RHE EF ~ 1.9 vs planar $BiVO_4$	[209]
$BiVO_4$-TiO_2-FTO io films	408 nm PS opals	PEC water splitting Photocurrent-IPCE 0.5 M $Na_2SO_4/0.1_2SO_3$	150 W Xe lamp AM 1.5 G 100 mW cm^{-2}	4.11 mA cm^{-2} at 1.23 V vs RHE IPCE of 60–80% 350–450 nm	[210]
$BiVO_4/WO_3$ io films	408 nm PS opals	PEC water splitting Photocurrent-IPCE 0.5 M Na_2SO_4 pH = 6.8 Co-Pi co catalyst	150 W Xe lamp AM 1.5 G 100 mW cm^{-2}	4.5 mA cm^{-2} at 1.4 V vs Ag/AgCl	[211]

io: inverse opal; EF: enhancement factor; nc: nanocrystalline; dis: disordered; η:photon-to-hydrogen conversion efficiency.

effects in the porous networks was not reported. Moreover, optimization of the co-assembly method [80] for the one-step fabrication of titania inverse opals by PS colloidal spheres combined with the water-soluble TiBALDH precursor by Hu et al. [142], showed that highly ordered photonic N-TiO_2 films could be prepared by the simultaneous action of TiBALDH as nitrogen source at an optimum calcination temperature of 400 °C. The N-TiO_2 inverse opals exhibited high photocatalytic activity on the aqueous phase degradation of both the RhB dye and the colorless tetracycline (TC) hydrochloride water pollutant under visible light, though stop band formation and slow photon effects were not identified.

Photonic effects were earlier explored by Xu et al. [143] on meso/

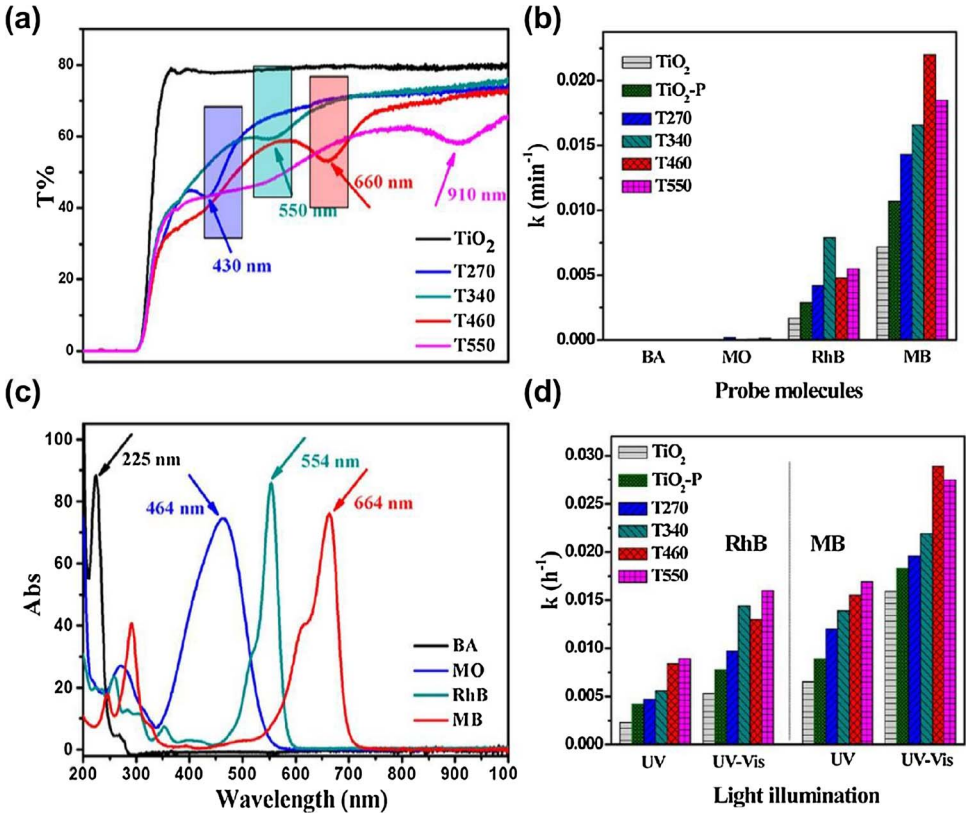

Fig. 19. (a) Transmittance spectra of the TiO_2 inverse opals in water and (c) optical absorption of probe molecules. (b) Kinetic constants (k) of for the photocatalytic degradation of BA, MO, RhB, MB probe molecules under visible light (420–800 nm), and (d) simulated solar light irradiation (320–800 nm) for RhB and MB dyes [78]. Copyright © 2013 American Chemical Society.

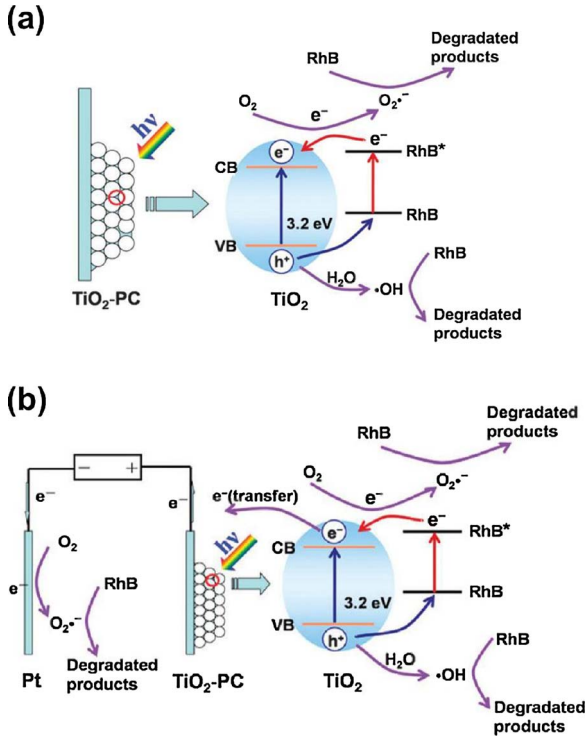

Fig. 20. Possible mechanisms of (a) photocatalytic and (b) photoelectrocatalytic RhB degradation on the TiO_2 inverse opals film under solar light irradiation [137]. Copyright © 2014 Owner Societies.

macroporous N-F co-doped TiO_2 inverse opals prepared by the liquid phase deposition (LPD) using for the first time silica colloidal crystal templates at low calcination temperatures of 250 °C. Well defined stop bands were observed at 433, 487 and 671 nm for the NF-TiO_2 inverse opals prepared by the 201, 228, or 315 nm silica colloidal spheres, leading to significant (~7 fold) enhancement of the MB visible-light photodegradation rate compared to non-structured porous NF-TiO_2 films as well as singly F doped inverse opals obtained at higher calcination temperature of 350 °C, indicative of the beneficial synergistic effects of NF co-doping in the visible light activity [42,144]. However, NF-TiO_2 films prepared by a mixture of silica colloidal spheres with different diameters presented comparable, though lower, MB degradation rates to the periodically ordered films indicating that the macroporous structure and multiple scattering effects are also important for the enhanced photocatalytic activity.

The contribution of slow photon amplification was corroborated by Rahul et al. [145] on a recent study of N-F co-doped TiO_2 inverse opals prepared by PS opal templates of two different diameters (215 and 460 nm) using nitric and trifluoroacetic acids as anion sources. After calcination at 400 °C, the corresponding 2.5–3 μm thick NF-TiO_2 photonic films presented stop band reflections at 336 and 695 nm, respectively (corresponding pore diameters at 144 and 274 nm) and apparent electronic absorption edges at 484 (2.56 eV) and 470 nm (2.64 eV) in the visible range due to N–F co-doping. In that case, the NF-TiO_2 inverse opal with stop band at ~340 nm, where reflection losses are moderated by the strong UVA titania's absorbance [51], presented the highest reaction rate on solid state RhB photodegradation under high intensity, direct or simulated solar light. This was attributed to red edge slow photons at ~400 nm that approach the broad electronic absorption edge at 480 nm. Nevertheless, the nearly two-fold performance enhancement on RhB photodegradation was reached in comparison with nanocrystalline spin coated NF-TiO_2 films of high pore volume though lower surface area, rather than disordered porous films from mixed colloidal templates to exclude enhanced scattering or mass transfer effects derived from the porous network.

The synergy of slow photons and Ti^{3+} self-doping for enhancing VLA photocatalysis was recently explored by Qi et al. [146] applying vacuum activation on TiO_2 inverse opals with tunable pore sizes, fabricated from PS opals with 170, 265 and 355 nm diameters, and stop

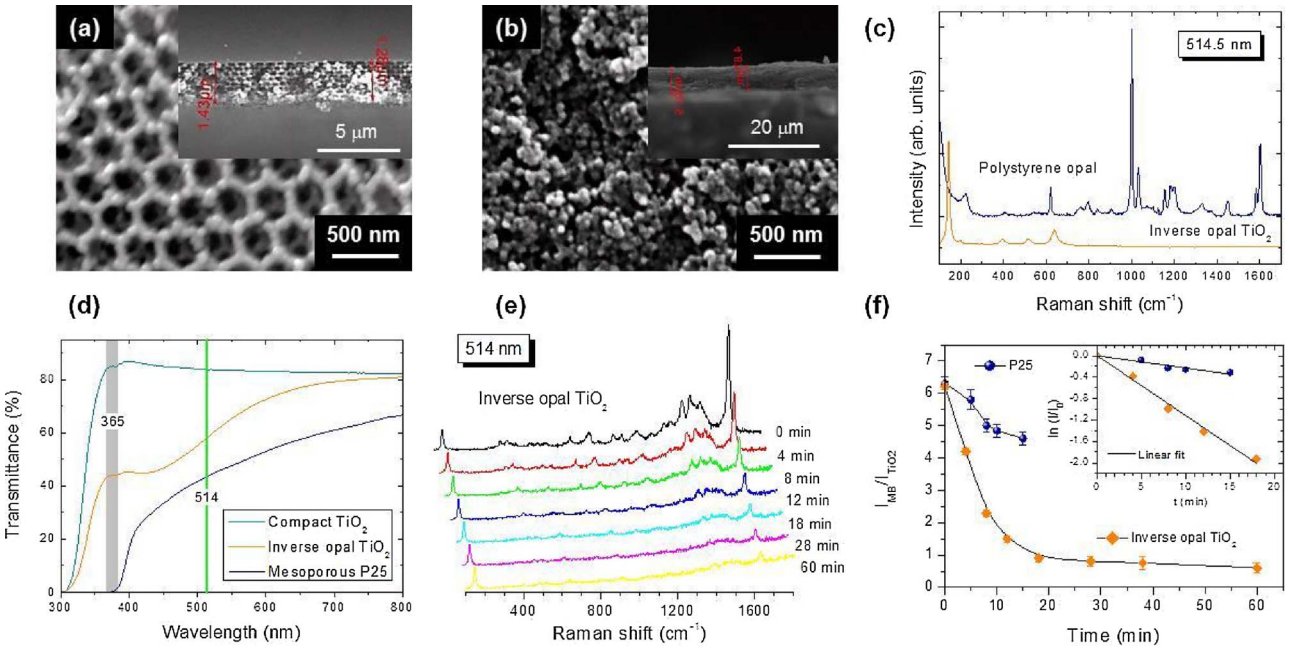

Fig. 21. Top view and cross section (insets) SEM images of the (a) inverse opal TiO_2 and (b) mesoporous P25 films. (c) Raman spectra of the PS template and the inverse opal TiO_2 at 514 nm. (d) Transmittance spectra of the TiO_2 inverse opal in comparison to P25 and compact nc-TiO_2 films. (e) Temporal evolution of the Raman spectra for the MB sensitized inverse opal under 514 nm illumination. (f) Time dependence of the integrated Raman intensity ratio I_{MB}/I_{TiO2} for the inverse opal TiO_2 and P25 films. The inset shows the plot of the normalized intensity ratio at t = 0 min, $\ln(I/I_0)$ vs t and the corresponding linear fits [71]. Copyright © 2017 Elsevier B.V.

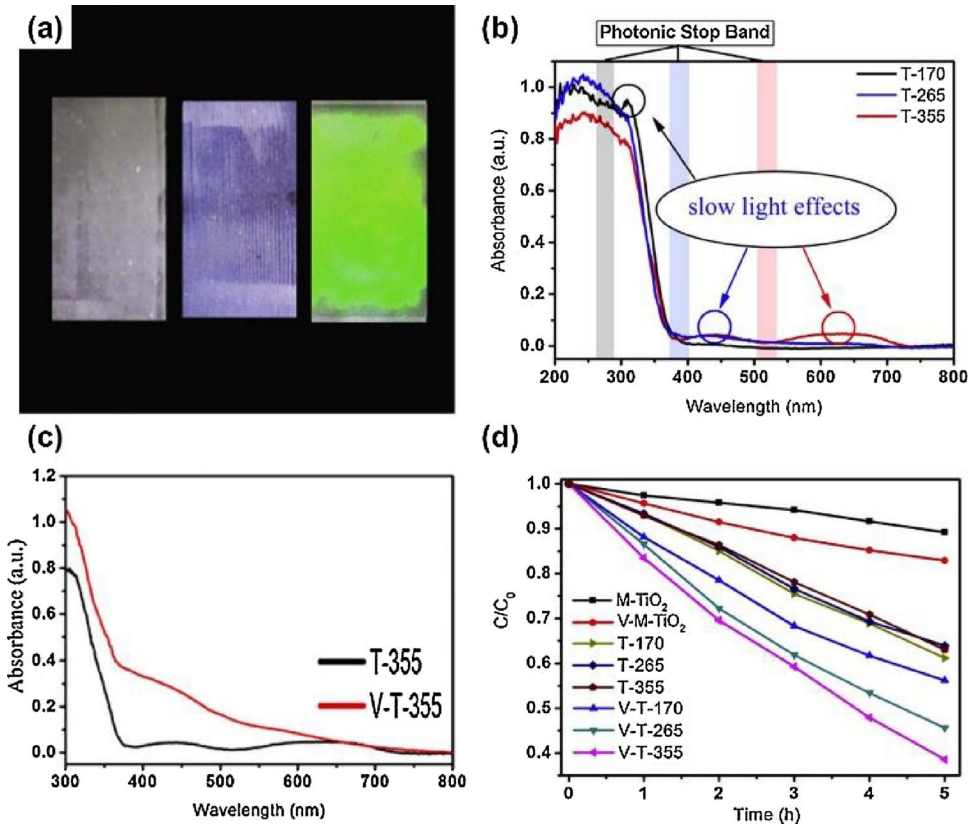

Fig. 22. (a) Optical photographs and (b) UV–vis spectra of the TiO_2 inverse opal films T-170, T-265 and T-355. (c) UV–vis spectra of the inverse opals obtained from 355 nm PS spheres before (T-355) and after vacuum treatment (V-T-355). (d) Comparative AO7 photodegradation kinetics for the inverse opal and mesoporous TiO_2 films (M-TiO_2) under visible light [146]. Copyright © 2014 Elsevier B.V.

bands at 270, 390 and 520 nm, as shown in Fig. 22(a) and (b). Titania's reduction by vacuum heat treatment resulted in the formation of oxygen vacancies and Ti^{3+} species that extended the optical absorbance of the TiO_2 inverse opals in the visible range [Fig. 22(c)]. The accompanying Ti^{3+} self-doping resulted in significant enhancement of the aqueous phase photocatalysis of acid orange 7 (AO7) under broadband visible light illumination with optimal performance for the inverse opals with 520 nm stop band, in contrast to UV irradiation for the untreated photonic crystals, where the maximum AO7 degradation was obtained for the inverse opal with its stop band red edge at the UVA range [Fig. 22(d)].

More recently, "black" TiO_2 inverse opals (BTIOs) were fabricated

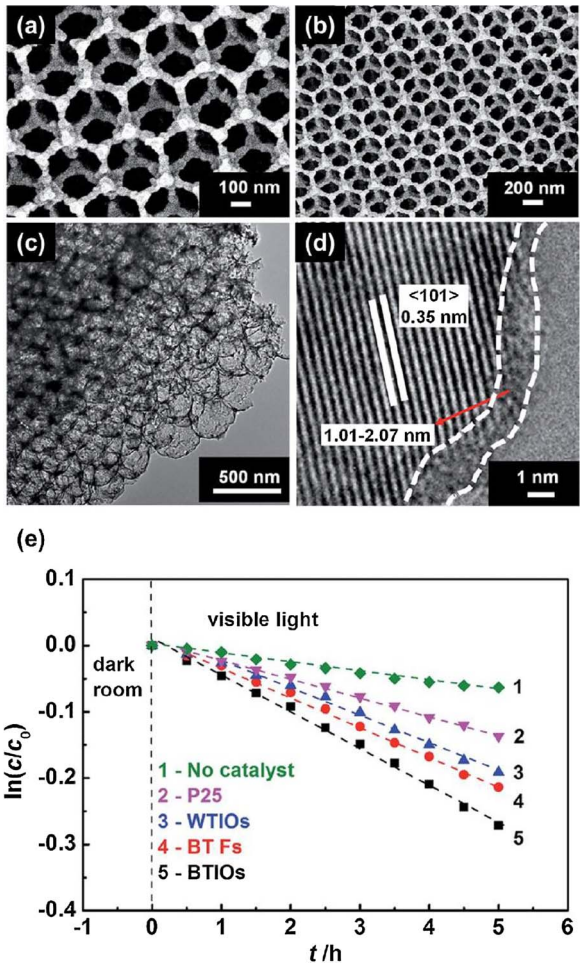

Fig. 23. (a), (b) SEM, (c) TEM and (d) high resolution TEM images of BTIOs obtained after hydrogenation. Dashed lines in (d) delineate a surface disordered layer with thickness of 1.01–2.07 nm. (e) MB degradation kinetics over BTIOs, WTIOs, BT Fs and P25 films under visiblel light [147]. Copyright © 2015 The Royal Society of Chemistry.

by Xin et al. [147] employing post-hydrogenation of regular "white" TiO_2 inverse opals (WTIOs) of 290 nm void diameter at 500 °C. The combination of hydrogenation and the concomitant electronic band gap narrowing of TiO_2 at 2.77 eV with the well-ordered inverse opal structure that remained intact after H_2 reduction [Fig. 23(a)–(d)], resulted in significant improvement of the films' photocatalytic activity on MB degradation over their scraped fragments (BT Fs) as well as the isostructural pristine inverse opals and P25 under visible light, as shown in Fig. 23(e). However, the interplay of photonic effects compared to the increase surface area were not determined, indicating the need for further development and validation studies of chemically doped TiO_2 photonic crystals for VLA photocatalytic applications, which despite their promising results, remain rather limited.

4.3. Surface modification by noble metals- plasmonic effects

Surface loading of titania nanomaterials by noble metals such as Au, Ag, Pt, and Pd has been long regarded as an efficient extrinsic modification to enhance charge separation of TiO_2 photocatalysts [148]. Since the Fermi levels of noble metals are commonly lower than that of *n*-type TiO_2, which is located closer to titania's conduction band (the noble metal work function is accordingly higher than that of *n*-type TiO_2), their equilibration upon contact in the composite structure causes the bending of titania's energy bands and the formation of a Schottky barrier (the highest occurring for Pt) at the metal-semiconductor interfacial region, which further drives photogenerated electrons from the TiO_2 conduction band to the metal particles. The electron scavenging ability of metal co-catalyst surface deposits on TiO_2 has been fruitfully exploited to reduce electron-hole recombination in noble metal modified titania, the most effective being Pt and Au [32], which under optimal loading conditions accelerate electron transfer to dissolved oxygen molecules and enhance the quantum yield of photocatalytic reactions.

The synergy of slow photon amplification with metal loading has been implemented for the first time by Chen et al. [149], using Pt loaded TiO_2 inverse opals with minimal refection losses due to the matching of the stop band reflection with titania's UVA absorption at 354 nm, leading to a four-fold increase in the solid state photodegradation rate of acid orange under broadband UV–vis illumination. This principle has been further applied by Ren et al. [150] for improving UV light utilization and quantum efficiency for CO_2 conversion to CH_3OH by fabricating Cu-modified TiO_2 inverse opals on quartz optical fibers used both as light conductor and catalyst support in a gas phase photocatalytic reactor. The beneficial Schottky junction effect in UV-induced charge separation has been demonstrated by Chen et al. [151] employing liquid phase deposition of a TiO_2 layer on electrodeposited Pt inverse opals on Ti substrates with variable stop band reflection in the UV–vis range (280–550 nm). The synergistic effect of slow photons and metal deposition in promoting light harvesting together with charge generation and separation under UVA light, has been amply confirmed and applied for the enhancement of hydrogen generation by photocatalytic water splitting over Pt [152,153] and Au [154] loaded TiO_2 inverse opals in powder form by tuning the stop band position with respect to the TiO_2 electronic band gap [152,153] and UV irradiation wavelength [154]. Significant progress has been recently achieved by Cai et al. [155] implementing the co-assembly of PS colloids, chloroauric acid and TiBALDH sol precursor into large area Au-loaded TiO_2 inverse opals without overlayer formation, as shown in Fig. 24(a) and (b). A 5.4-fold photocatalytic enhancement on BA degradation under UVA light has been realized for stop band reflection at 308 nm in water compensated by the strong electronic absorption of TiO_2, as shown in Fig. 24(c) and (d).

Despite these major developments, amplification of the photocatalytic performance in metal loaded TiO_2 photonic crystals relied solely on Schottky junctions that extend the lifetime of photogenerated charge carriers, limiting improvements of the process efficacy to UVA excitation. The other distinct feature of noble metal NPs is their unique capacity for strong light absorption through the excitation of localized surface plasmon resonance (LSPR) arising from the resonant photon-induced collective oscillation of metal valence electrons [31], which can be tailored in the UV–vis spectral range by changing the composition, size, shape and dielectric environments of the plasmonic nanostructures [14]. Plasmonic photocatalysts [156] involving mainly Ag and Au nanoparticles loaded on TiO_2, can efficiently absorb visible light through appropriately tuned LSPR, whose radiative and non-radiative decay may lead to distinct charge/energy transfer processes such as energetic (hot) electron injection (Fig. 25) [157] and resonance energy transfer or even plasmon-induced radiative energy transfer [158]. This unique mechanism that enables electron-hole generation in titania and visible light activation in the absence of band gap excitation, underlies plasmonic photocatalysis that has become a burgeoning research field for solar-to-chemical-energy conversion applications [31].

The synergistic effect of LSPR and slow photons has been demonstrated for the first time by Lu et al. [159] utilizing the uniform infiltration and grafting of Au NPs (average diameter of 15 nm) on TiO_2 inverse opals deposited by LPD in PS opals (193 and 240 nm diameters) by in-situ hydrothermal reduction of chloroauric acid [Fig. 26(a)]. Matching the blue edge of the stop band reflection at 560 nm with the LSPR of Au NPs [Fig. 26(b)] resulted in a distinct improvement of the aqueous phase photodegradation rate of 2,4-dichlorophenol (2,4-DCP) under visible light, as shown in Fig. 26(c). Scavenging and ESR spin-trapping experiments indicated that •OH radicals stemming from the

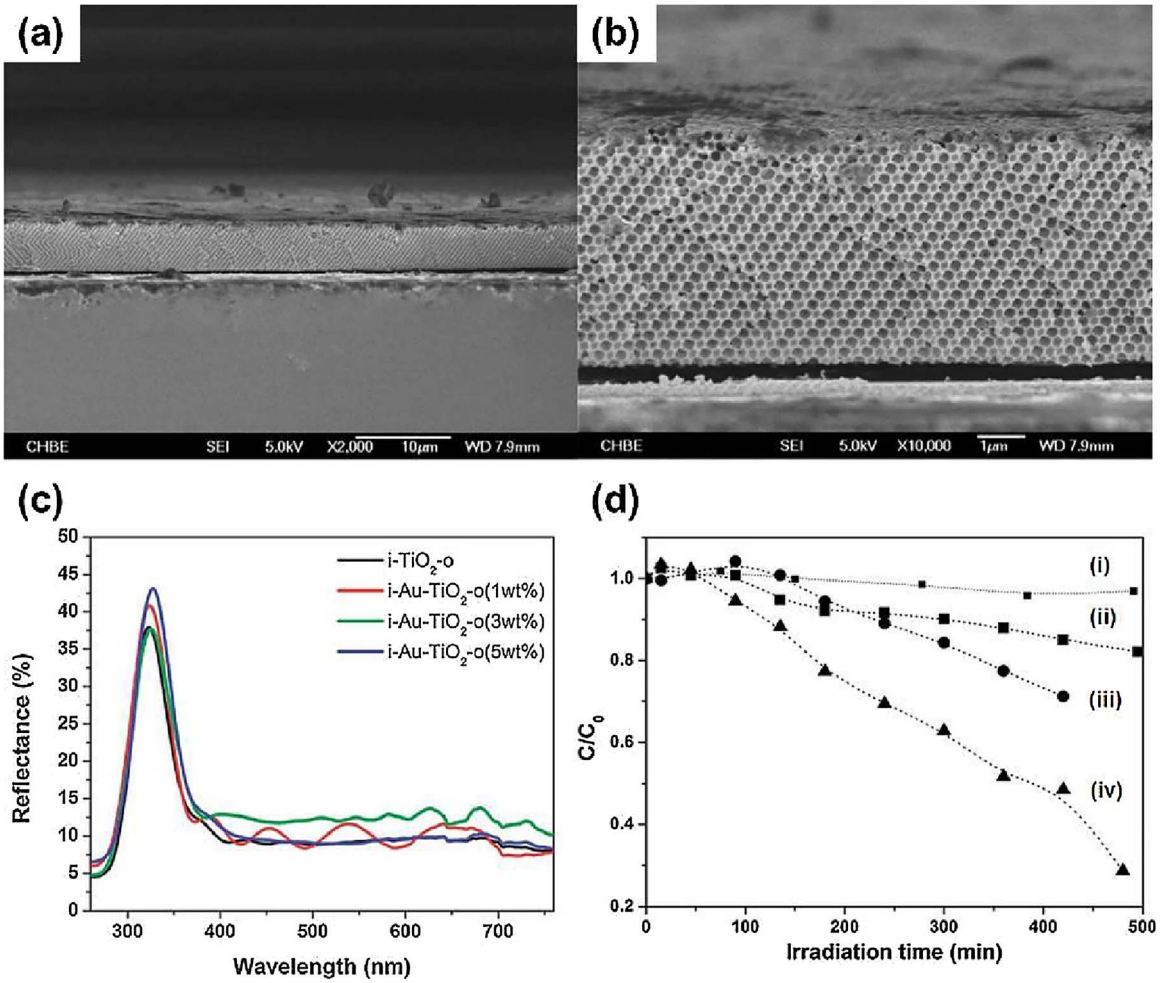

Fig. 24. (a) and (b) cross sectional SEM images of inverse Au loaded TiO_2 opal (i-Au-TiO_2-o) films obtained from 398 nm PS colloidal opal templates at different magnifications. (c) Reflectance spectra of i-TiO_2-o and i-Au-TiO_2-o films fabricated from 170 nm PS spheres with various Au loadings in water. Aqueous phase BA photocatalytic degradation over (i) i-AuTiO_2-o without UV irradiation, (ii) nc-TiO_2, (iii) i-TiO2-o, and (iv) i-Au-TiO_2-o (170 nm PS opal) under UV irradiation [155]. Copyright © 2014 The Royal Society of Chemistry.

reduction of dissolved O_2 by electrons was the main ROS for pollutant degradation, corroborating the increased yield of electron injection in TiO_2 by the cooperatively enhanced excitation of the Au surface plasmons by slow photons under visible light.

Coupling the LSPR of Au NPs with slow photons has been further applied to improve photoelectrochemical (PEC) water splitting and hydrogen generation under visible light on Au loaded surface-textured TiO_2 inverse opals [160] and more recently on bilayer photoanodes consisting of a anatase TiO_2 inverse opal deposited on top of a rutile TiO_2 nanorod array layer [161]. In the former case, although the stop band reflectance could not be identified on the textured titania photonic films, their high surface area resulted in broad diffuse reflectance spectra over the visible range that in combination with the broad LSPR of Au NPs at 540 nm enhanced the photocurrent density by 2.58 times compared to conventional P25 photoelectrodes. In the latter case, two-fold enhancement of PEC water splitting efficiency was achieved under visible light when slow photons at the stop band red edge (518 nm) were intentionally tuned to overlap with the LSPR at 536 nm of the 10 nm Au NPs. High photoconversion efficiency of 0.71% under simulated solar light (AM 1.5 G) was thus achieved, further assisted by the photoelectrode design supporting large amounts of active Au NPs and extensive Au/TiO_2 interfaces without greatly compromising the charge-carrier collection efficiency in the vertically oriented TiO_2 nanorod underlayer.

Plasmonic effects were earlier investigated by [162] in Ag loaded TiO_2 inverse opal films of constant (290 nm) pore diameter prepared by silica colloidal crystal templates and a facile wet chemical route using $AgNO_3$ to deposit silver NPs on the titania photonic crystal at different loadings. Photocatalytic evaluation revealed significant enhancements, 1.5 and 4.5-fold, of the MB degradation rate constants in aqueous solution under UV (254 nm) and Vis (400–760 nm) irradiation at different Ag loadings, though the interplay of slow photons at the edges of the 605 nm stop band reflection with the LSPR of Ag NPs identified at 435 nm were not resolved.

Besides titania, plasmonic and photonic amplification effects have been thoroughly explored by Meng et al. [163] in Au loaded ZnO inverse opals of variable stop bands (182, 222 and 277 nm carboxyl-modified PS opal templates), where Au NPs with a mean diameter of ca. 3.4 nm were uniformly deposited by magnetron sputtering. Matching the blue edge slow photon energy with the LSPR of Au NPs at 540 nm [Fig. 27(a) and (b)] resulted in a prominent increase of the photocatalytic activity on the aqueous phase RhB and 4-CP degradation under visible light with the kinetic constant being ca. 5.6-fold higher than the corresponding one obtained by conventional N doped TiO_2 VLA photocatalysts and nearly 25-fold higher than that of commercial ZnO NPs, as shown in Fig. 27(c) and (d). Determination of ROS and H_2O_2 produced during the photocatalytic reaction indicated that superoxide $\cdot O_2^-$ and hydroxyl $\cdot$OH radicals formed via the O_2 reduction pathway by photoinduced electrons generated from the visible light activated Au LSPR or even RhB are responsible for the photocatalytic degradation reaction, likewise Au loaded TiO_2 inverse opals [159].

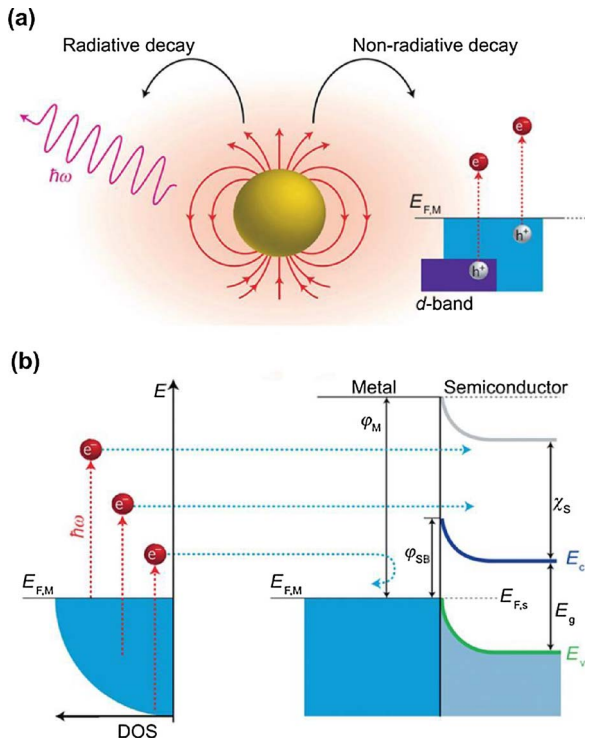

Fig. 25. (a) Localized surface plasmons can decay radiatively via photon emission or non-radiatively leading to hot electron generation that can occur through the excitation of intra- or higher energy interband transitions. (b) Plasmonic energy conversion in metal-semiconductor junctions: hot electrons from occupied energy levels are excited above the aligned Fermi levels $E_{F,M}$ and $E_{F,S}$ of the metal and the semiconductor, respectively. Hot electrons with energy higher than the interface Schottky barrier $\varphi_{SB} = \varphi_M - \chi_S$, where φ_M is the metal's work function and χ_S is the semiconductor's electron affity can be injected into the conduction band E_c of the semiconductor with band gap E_g [157]. Copyright © 2014 Macmillan Publishers Limited.

4.4. Heterostructuring

Coupling TiO_2 with narrow band gap semiconductors like metal oxides and chalcogenides, especially metal sulfides and selenides, has been a promising approach to simultaneously enable visible light excitation and improve charge separation by means of interfacial electron transfer in judiciously designed heterostructured VLA photocatalysts. Uniform deposition of CdS nanocrystals (7–8 nm) in titania photonic crystals was first implemented by Cheng et al. [164] utilizing the successive ionic layer adsorption and reaction (SILAR) method in TiO_2 inverse opals fabricated via ALD in PS opal templates with stop bands in the vis-NIR range. Significant enhancement for PEC water splitting was thereby reported, quantified by the increase of the photocurrent density and the incident photon-to-electron conversion efficiency (IPCE) of the CdS sensitized films in the range of 300–650 nm under simulated solar light. More recently, Su et al. [165] reported the development of a highly efficient ternary CdS/Au/TiO_2 photocatalyst by the successive infiltration of 30 nm Au NPs and chemical bath deposition (CBD) of CdS QDs in titania inverse opal powders, as shown in Fig. 28. The resulting photonic crystals presented multifold improvements in the photocatalytic H_2 generation under visible light compared to the corresponding CdS/TiO_2 and Au/TiO_2 binary structures, attributed to the synergy of Au LSPR and CdS narrow band gap activation at ~550 nm for enhanced charge generation and separation. Bilayer CdSe/CdS QD co-sensitization of mesoscopic TiO_2 inverse opals with roughly 80 nm pore diameter was further investigated by Lee et al. [166] using sequential SILAR and CBD coatings, which resulted in extended visible light absorption up to 680 nm as well as increased photocurrent density and IPCE values under solar light for PEC water splitting applications.

Slow photon effects were explicitly investigated in CdS-sensitized

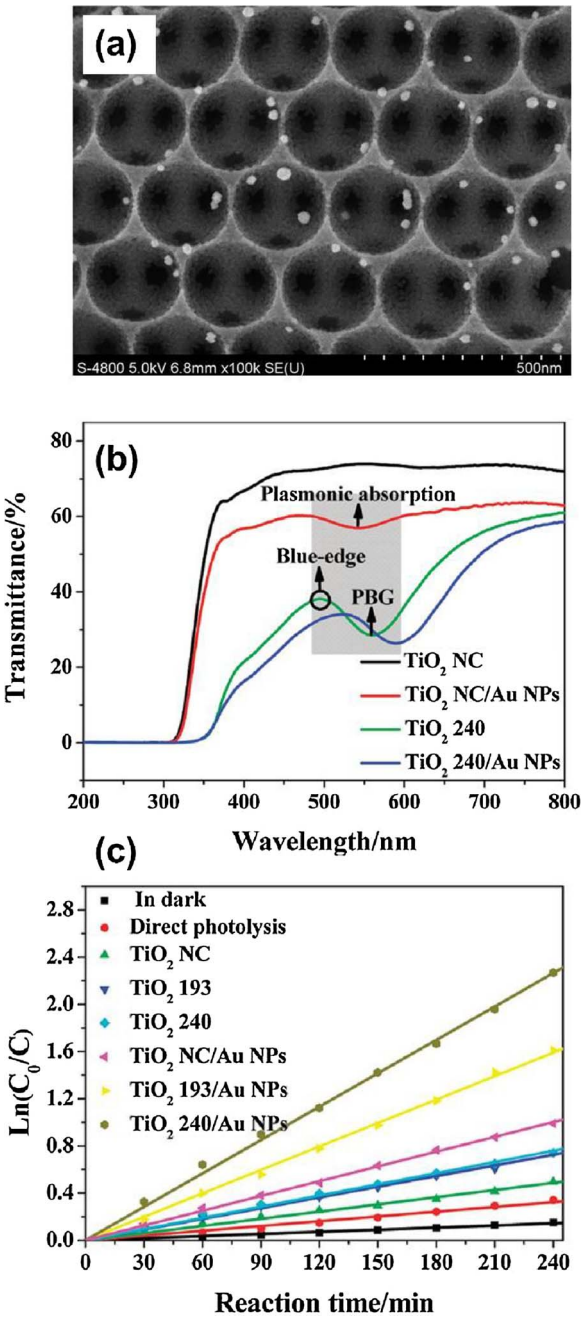

Fig. 26. (a) SEM image and (b) transmittance spectra of Au-TiO_2 inverse opals made from PS opals of 240 nm (TiO_2 240/Au NPs) in comparison with unmodified inverse opal (TiO_2 240) and nc-TiO_2 films. The shaded region indicates the overlap between the stop band and its blue edge with the Au LSPR. (c) 2,4-DCP photodegradation kinetics for the different photocatalysts under visible light ($\lambda > 420$ nm) [159]. Copyright © 2012 American Chemical Society.

wide band gap semiconductor inverse opals, namely ZrO_2 [167] and SnO_2 [168] used as non-absorbing but optically active macroporous supports in the form of powder and films, respectively, so as to independently optimize sensitized visible light harvesting and photochemical performance. In the former case, a pronounced 4.7 fold enhancement of hydrogen evolution was derived for CdS/ZrO_2 inverse opal under visible light in comparison to a non-photonic support, when the CdS absorption edge at 520 nm partially overlapped with the blue edge of the photonic stop band of the photocatalytically inert ZrO_2 support. In the latter case, SnO_2 photonic crystals fabricated by LPD on FTO glass substrates and decorated with CdS NPs (5–10 nm) by CBD presented markedly improved photocurrent density and aqueous phase

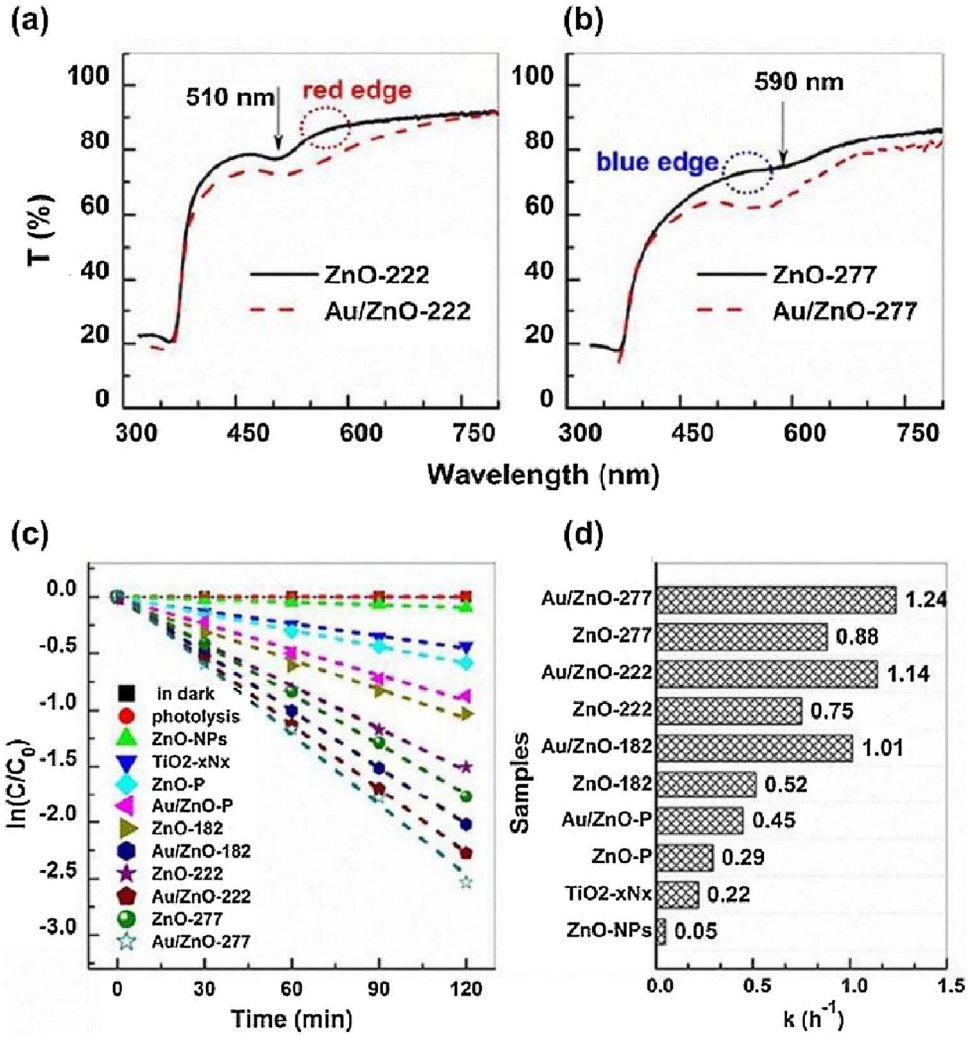

Fig. 27. Transmittance spectra of Au loaded ZnO inverse opals in comparison to the homologous unmodified films fabricated by (a) 222 nm and (b) 277 nm colloidal sphere templates. Arrows depict the stop band positions. (c) RhB photodegradation kinetics and (d) the corresponding kinetic constants for the different photocatalysts under visible light ($\lambda > 420$ nm) [163]. Copyright © 2015 The Royal Society of Chemistry.

photocatalytic degradation rates for carbamazepine removal under visible light combined with appreciable photostability and weak Cd^{2+} leaching (Fig. 29). These features were associated with the strong CdS-SnO_2 interfacial coupling and the close match of CdS electronic absorption to the SnO_2 stop band at 490 nm. Control experiments using different scavengers and ESR spin traps indicated that electrons and $\cdot O_2^-$ radicals generated by O_2 reduction were the dominant ROS during the photocatalytic process, as schematically shown in Fig. 29(e), similar

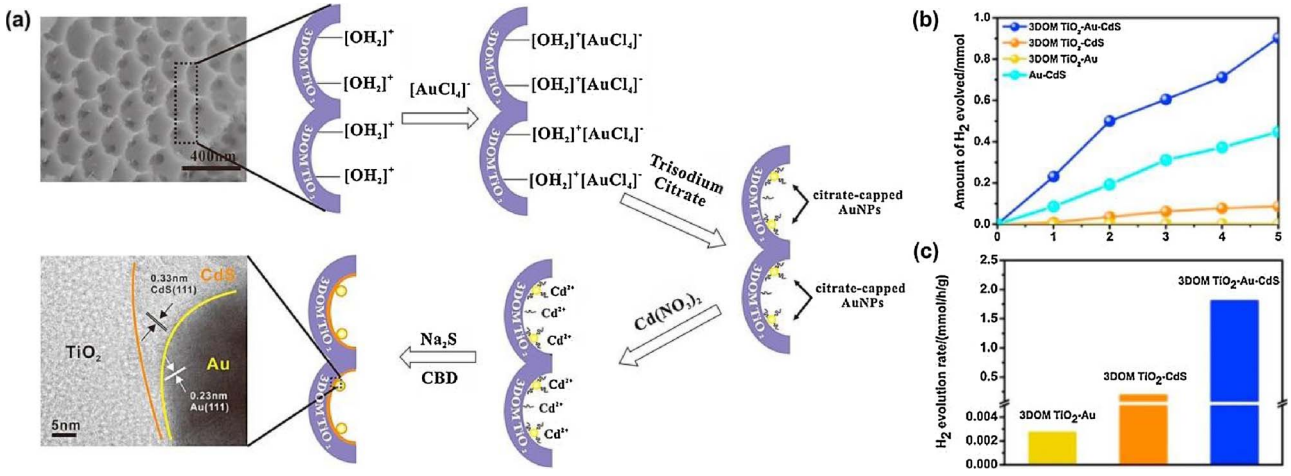

Fig. 28. (a) Scheme of CdS/Au/TiO_2 inverse opal fabrication process. (b) Photocatalytic hydrogen evolution for the 3D ordered macroporous (3DOM) samples and (c) H_2 evolution rates under visible light irradiation [165]. Copyright © 2015 Elsevier B.V.

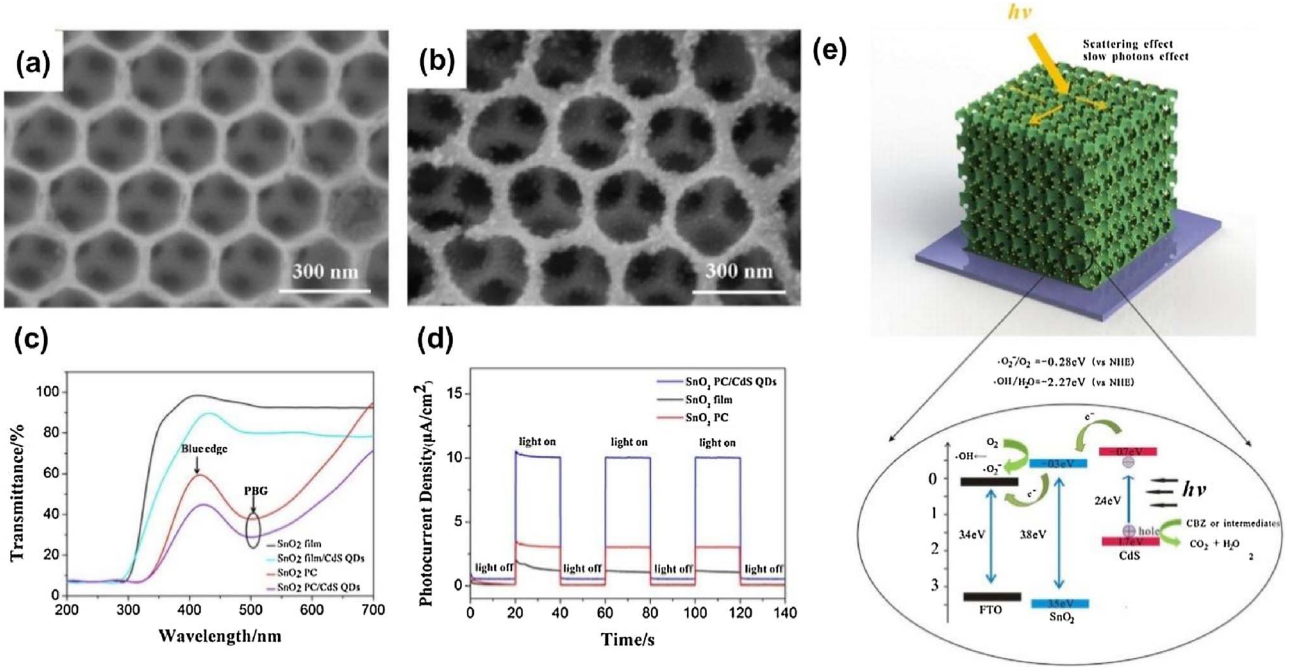

Fig. 29. SEM images of (a) SnO_2 and (b) CdS/SnO_2 inverse opals. (c) Transmittance spectra and (d) photocurrent densities ($\lambda > 400$ nm) of the SnO_2 and CdS/SnO_2 inverse opals and films. (e) Schematic of the pollutant degradation mechanism by CdS/SnO_2 inverse opals under visible light [168]. Copyright © 2014 Elsevier Ltd.

to plasmonic NP loaded photonic crystals [159].

Quantum dot sensitization was further combined with Au loading by Li et al. [169] in the design of a sandwich structured ZnO/Au/CdS inverse opal electrode by the combination of ALD and SILAR methods for enhanced PEC hydrogen production. Significant increase of the AM 1.5 photocurrent density and IPCE in the visible range were demonstrated for the composite structure, mainly related to the enhanced visible light harvesting by CdS QDs (525 nm absorption edge) and Au LSPR (600 nm) together with the improved charge transfer between ZnO and CdS via the intermediate Au NP layer. Very recently, ternary CdS/Au/SrTiO3 composites were prepared by the successive deposition of Au and CdS NPs in $SrTiO_3$ inverse opals of variable void diameters and they were applied for hydrogen evolution under visible light irradiation [170]. Matching the broad slow photon region of the SrTiO3 inverse opal powders with the composite's optical absorption in the visible range [171] resulted in a remarkably high hydrogen evolution rate that was further augmented to 5.46 mmol g^{-1} h^{-1} combined with an apparent quantum efficiency of 42.2% at 420 nm by the post-photodeposition of Pt NPs as co-catalyst on the optimal photonic crystal, due to the synergy of efficient charge separation, Au LSPR and slow photons (Fig. 30).

Heterostructuring TiO_2 photonic crystals with VLA metal oxides has been pursued by Geng et al. [172] through the infiltration of Cu_2O nanocrystals (10 nm) in TiO_2 inverse opals by a hydrothermal reduction method. Engineering the photonic band gap at ca. 580 nm that matched the visible light absorption of Cu_2O NPs resulted in a significant acceleration of the aqueous phase photocatalytic degradation rates of RhB and Bisphenol A (BPA) under UV–vis irradiation (320–780 nm), related to the slow photon enhanced light harvesting and charge separation in the heterojunctions between n-type TiO_2 and p-type Cu_2O.

The development of photonic crystal heterostructured metal oxide nanocomposites was also investigated for ZnO and TiO_2 [173]. In that case, tuning the stop band reflection to the MO absorption band at 470 nm (Section 4.1), leaded to improved dye degradation rates under simulated solar light surpassing those attained by the individual metal oxide nanoparticulate or inverse opal films as well as benchmark Aeroxide® P25 TiO_2 films due to the enhanced charge separation in the ZnO-TiO_2 heterojunction. The underlying interfacial charge transfer has been further explored by Zalfani et al. [174] in ZnO QD sensitized TiO_2 photonic crystals, where the relative positions of ZnO to TiO_2 energy bands could be shifted to promote charge transfer between the constituent wide band gap semiconductors via quantum size effects leading to markedly improved RhB photocatalytic degradation under UV light. Earlier, ZnO-TiO_2 bilayer photoanodes were demonstrated by Karuturi et al. [175] through hydrothermal growth of ZnO nanowire arrays atop ALD fabricated TiO_2 inverse opals that upon further CdS sensitization by SILAR resulted in enhanced PEC performance.

Compositing titania with graphene and its derivatives, has been considered as a promising route to improve charge separation and light harvesting in TiO_2 photocatalysts relying on graphene's exceptional electron acceptor action and charge transport properties together with its unique 2D morphology and broadband light absorption [176–178]. Among them graphene oxide (GO), the solution processable graphene precursor, has been attracting particular attention because of GO's rich surface chemistry and reactivity derived by its lamellar structure consisting of graphene sheets with randomly distributed oxygen functional groups that provide abundant anchoring sites for semiconductor NPs and thus an ideal scaffold for GO-TiO_2 composites' fabrication [179]. Hierarchically ordered macro/mesoporous graphene/TiO_2 inverse opals films were first reported by Du et al. [180] by the incorporation of GO and Pluronic P123 surfactant in the titania sol-gel precursor infiltrated in PS opal templates (240 and 300 nm) followed by in situ GO reduction and calcination. Order of magnitude enhancement of the MB photocatalytic degradation in aqueous solution has been reported in comparison to mesoporous TiO_2 films with and without graphene, 17 to 11-fold, respectively, though photonic effects were not identified. The development of graphene inverse opal electrodes was recently reported by Yoon et al. [181] by direct CVD growth of graphene on Ni inverse opals templates fabricated by electrodeposition of 350 nm PS opal films, as shown in Fig. 31(a). Hematite (α-Fe_2O_3) NPs were then decorated onto the 3D graphene nanostructure via a hydrothermal method leading to α-Fe_2O_3/graphene inverse opal photoelectrodes [Fig. 31(b)–(d)] that showed enhanced visible light absorbance and photocurrent density compared to bare hematite NP films.

Very recently, plasmon-sensitized graphene-TiO_2 photonic crystals were developed by Boppella et al. [182] employing sequential

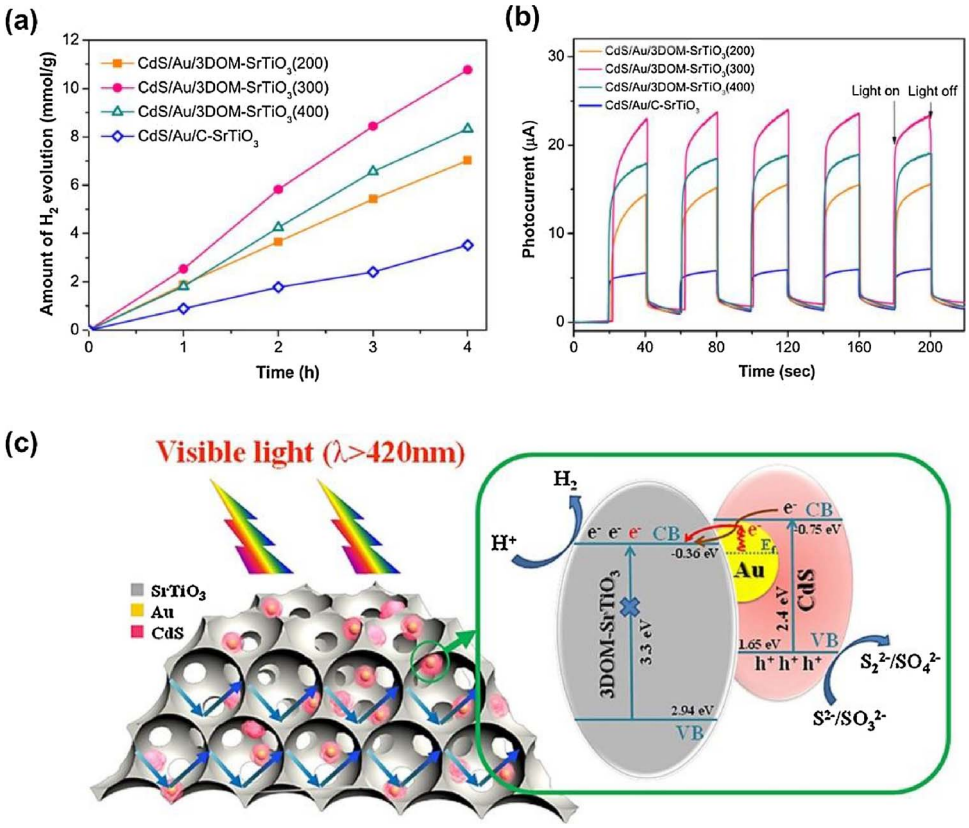

Fig. 30. (a) Hydrogen evolution and (b) photocurrent-time (I–t) curves for the ternary CdS/Au/$SrTiO_3$ inverse opals of different diameters compared to samples prepared by commercial $SrTiO_3$ (CdS/Au/C-$SrTiO_3$). (c) Schematic of the photogenerated charge transfer mechanism for under visible light [170]. Copyright © 2017 Elsevier B.V.

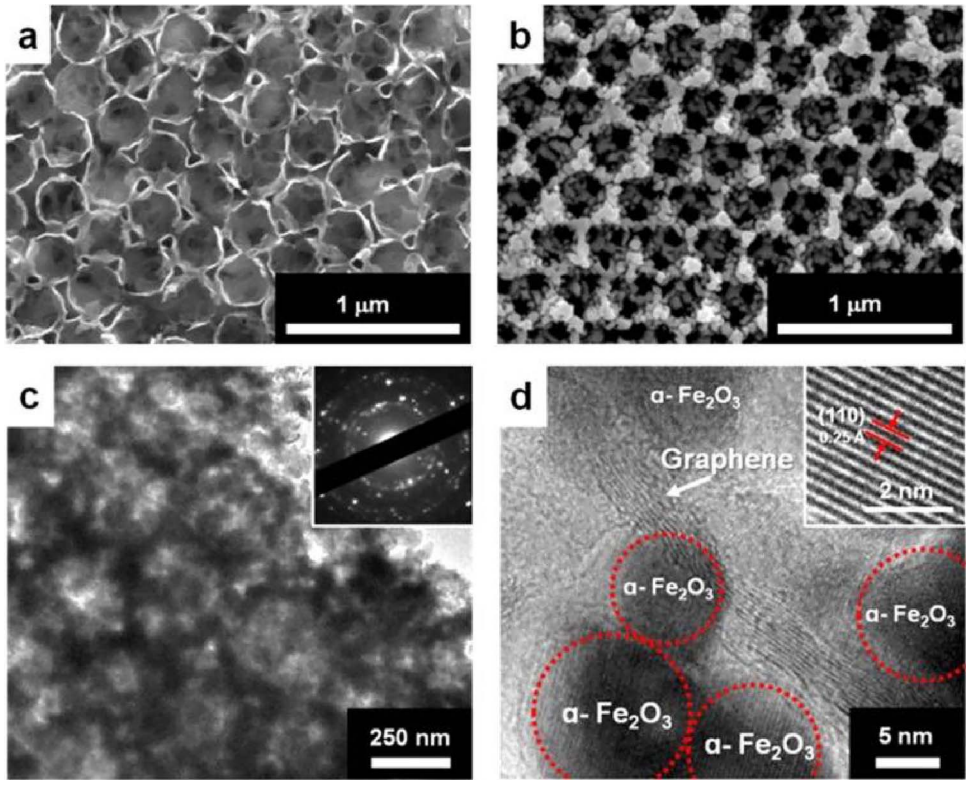

Fig. 31. SEM images of (a) graphene and (b) α-Fe_2O_3/graphene inverse opal photoelectrodes. (c) and (d) TEM images of α-Fe_2O_3/graphene inverse opal. The insets in (c) and (d) depict the selected area electron diffraction pattern (SAED) and the (110) plane of hematite, respectively [181]. Copyright © 2014 American Chemical Society.

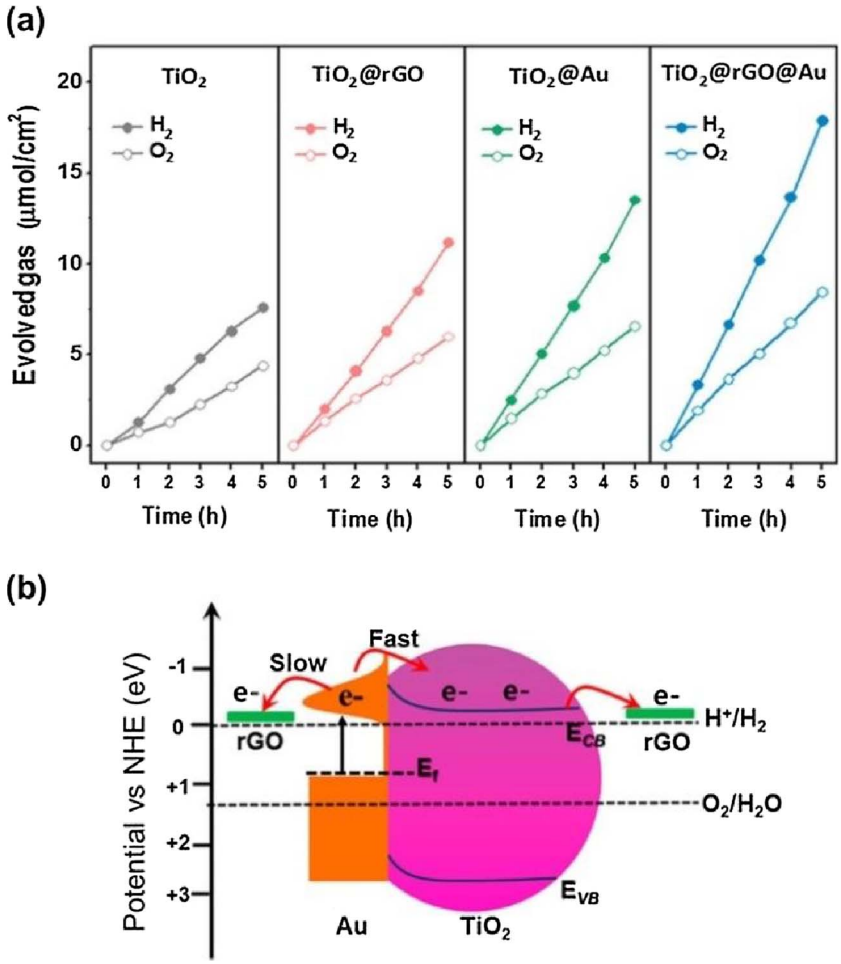

Fig. 32. (a) H_2 and O_2 evolution kinetics under simulated solar light at 1.23 V vs RHE for TiO_2, rGO/TiO_2, Au/TiO_2, and Au/rGO/TiO_2 inverse opal photoelectrodes. (b) Schematic representation of the photoinduced charge separation mechanism in the heterostructured photoelectrode [182]. Copyright © 2017 American Chemical Society.

deposition of reduced graphene oxide (rGO) and Au NPs (15 nm) into 500 nm diameter TiO_2 inverse opals films (stop band anticipated at ca. 1200 nm) for PEC water-splitting applications. A marked rise in the H_2 evolution rate was observed for the Au/rGO/TiO_2 inverse opals compared to unmodified titania photoelectrodes especially under visible light [Fig. 32(a)], attributed to the synergy of Au LSPR (520 nm) and rGO-mediated charge separation/transportation, according to the scheme of Fig. 32(b). Besides graphene, carbon-deposited TiO_2 photonic crystals have been fabricated as highly efficient VLA photocatalysts by Lee at al. [183] via high-temperature pyrolysis of phloroglucinol/formaldehyde resol coatings onto large macropore (500 nm) titania inverse opals. High rates of MB degradation were thus demonstrated in both aqueous and viscous polymeric solutions for high carbon loadings under visible light (495–700 nm) due to the formation of a carbon layer together with C-doping at the carbon-TiO_2 interface, which synergistically enhanced visible light absorption.

Poly(3-hexylthiophene) (P3HT) conductive polymer was earlier applied by Liao et al. [184] as visible light sensitizer of a titania bilayered heterostructure comprising a TiO_2 NP film on top of an inverse opal underlayer with 150 nm void diameter and stop band at 410 nm. The composite photonic structure showed significantly improved aqueous phase photocatalytic MB degradation under visible light ($\lambda > 400$ nm). This was related to both the enhanced visible light absorption owing to the cooperative effect of stop band backscattering towards the top NP layer at ca. 400 nm and slow photons effect at the red edge (ca. 550 nm) matching the P3HT electronic absorption together with the facilitated separation of photogenerated carriers owing to the P3HT-TiO_2 heterojunction.

4.5. Metal oxide photocatalysts beyond TiO_2

Photonic crystal-assisted enhancement of visible light harvesting has been further pursued for narrower band gap semiconductors like hematite (a-Fe_2O_3) [185], tungsten (WO_3) [186,187] and bismuth (Bi_2O_3) [188] trioxides, as alternatives to modified titania VLA photocatalysts. Specifically, despite the favorable electronic band gaps of these simple binary metal oxides in the range of 2.2–2.7 eV, their visible light induced photoresponse is significantly impaired by fast recombination kinetics and the concomitant short diffusion length of charge carriers, especially for a-Fe_2O_3 [189,190] as well as thermodynamic limitations imposed by their relatively low conduction band potential to drive single-electron O_2 reduction, as shown in Fig. 33 [47], posing the need for light harvesting improvements.

Nanocrystalline hematite inverse opal films with 3D-ordered interconnected macropores of 340 nm diameter were fabricated by Xie et al. [185] using layer-by-layer deposition and hydrolysis of $FeCl_3$ in PS opal templates (356 nm). The a-Fe_2O_3 photonic crystal presented a 2.4-fold amplification of the crystal violet (CV) photodegradation rate in aqueous solutions under visible light, compared to nanocrystalline reference films, which was largely associated with multiple light scattering and efficient mass transport effects in the macroporous structure. Slow photon enhancement was nevertheless identified by angle dependent solid state photodegradation experiments under monochromatic (550 nm) light irradiation at 45° incidence, when the red edge of the stop band (631 nm at normal incidence in air) approached hematite's electronic bandgap.

Surface modification of WO_3 inverse opals was recently

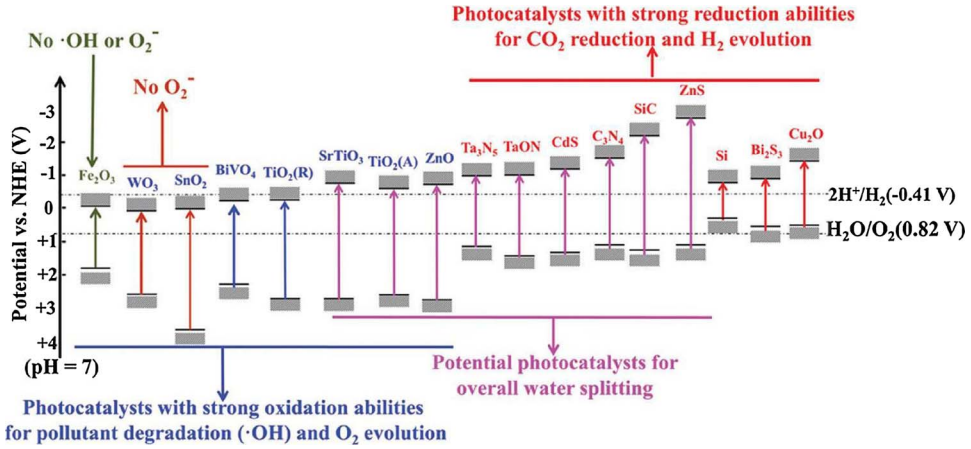

Fig. 33. (a) Band positions of selected semiconductor photocatalysts at pH = 7 aqueous solutions and their application potential [47]. Copyright © 2016 The Royal Society of Chemistry.

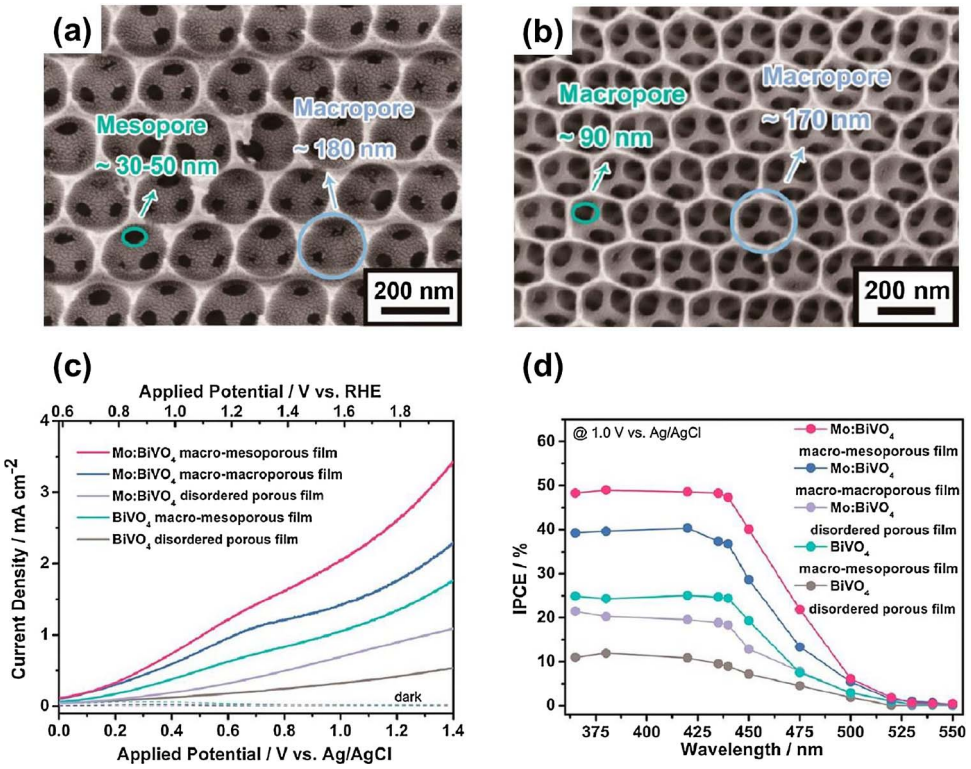

Fig. 34. SEM images of the (a) meso- and (b) macro-macroporous Mo:$BiVO_4$ photonic films. (c) Photocurrent density-potential curves and (d) IPCE spectra of the different macroporous inverse opals compared to disordered porous films [197]. Copyright © 2014 American Chemical Society.

implemented by Chang et al. [191] with silver orthophosphate (Ag_3PO_4) a highly competent VLA photocatalyst [192] for O_2 evolution from water and organic pollutant decomposition provided that corrosion from photogenerated electrons is effectively evaded [193]. Optimization of both Ag_3PO_4 loading and macropore diameter of the WO_3 photonic crystals so that the slow photon frequency approached the composites' broad absorption edge at 460–550 nm, resulted in a notable acceleration of visible light degradation of phenol, BPA, RhB, MB and malachite green (MG) organic contaminants and water splitting for O_2 evolution along with enhanced stability. Silver orthophosphate was further applied by Zhang et al. [194] as visible light sensitizer on $SrTiO_3$ inverse opals powders leading to ternary Ag_3PO_4/Ag/$SrTiO_3$ heterostructured photonic crystals. Likewise, tuning the loading and $SrTiO_3$ void diameter resulted in markedly enhanced photocatalytic performance on RhB, MB and phenol degradation under visible light, mostly related to the Z-scheme charge transfer mechanism assisted by photonic effects that also inhibited the accumulation of photogenerated electrons in Ag_3PO_4 and its photocorrosion under UV–vis irradiation.

Ternary metal oxides including bismuth tungstate (Bi_2WO_6) layered perovskites (Aurivillius phase) as well as bismuth ($BiVO_4$) and indium ($InVO_4$) vanadates have been recently attracting particular attention as promising alternatives to traditional TiO_2-based VLA photocatalysts, especially as photoanodes enabling efficient harvesting of the blue portion of solar light for water splitting and H_2 generation applications [195]. Well crystallized Bi_2WO_6 inverse opals were developed for the first time by Zhang et al. [196] at relatively low calcination temperatures (450–550 °C) using a complex aqueous precursor produced via complexation of Bi^{3+} and W^{+6} from metal salts and oxides, i.e. bismuth nitrate and ammonium tungsten oxide hydrate with diethylene-triamine-pentaacetic acid, that was infiltrated to 460 nm diameter PS opal templates. Significant enhancements of the photonic efficiencies for the VLA photocatalytic degradation of both the colored MB dye and the

colorless salicylicic acid (SA) water pollutants were achieved, compared to conventional Bi_2WO_6 films (the enhancement factors being 2.6 and 2.4, respectively), while the corresponding photon-to-hydrogen conversion efficiency for PEC water splitting under visible light exhibited a three-fold increase. These marked improvements were mostly derived from multiple light scattering and improved molecular transfer within the Bi_2WO_6 inverse opal porous structure, whereas the contribution of slow photons was resolved by angle dependent MB photodegradation under visible-light at 55° incidence angle when the stop band of the large pore inverse opal blue-shifted to 440 nm, so that its red edge overlapped the electronic absorption edge of Bi_2WO_6 at 470 nm.

Following a similar innovative approach, Mo-doped $BiVO_4$ inverse opal photoelectrodes were fabricated by Zhou et al. [197] utilizing a metal salt precursor that was infiltrated in opal templates consisting of 200 nm PS spheres. The latter were subjected to short time (3 and 10 min) post heating at 110 °C to increase their contact area and thereby enlarge the interconnecting mesopores of 30–50 nm in the inverse structure to 90–150 nm macropores after template removal, as shown in Fig. 34(a) and (b). Among the different hierarchically porous Mo:$BiVO_4$ photonic films, the meso-macroporous ones presented the highest PEC performance for water splitting [Fig. 34(c) and (d)] as well as the longest carrier lifetimes, which were mainly related to the synergy of low contact resistance at the electrolyte/electrode interface and the enhanced conductivity of the Mo:$BiVO_4$ electrode.

Highly efficient bismuth vanadate VLA photoanodes for water splitting were tailor designed by Zhang et al. [198] based on the synergy of photonic engineering with LSPR in Mo:$BiVO_4$ inverse opals prepared from of PS colloidal crystal templates, assembled on top of a thin (150 nm) compact Mo:$BiVO_4$ film to minimize reflection losses. Surface modification of the photonic crystals with 20 nm Au NPs resulted in superior photocurrent density reaching 3.1(1) mA cm^{-2} at 1.23 V versus reversible hydrogen electrode (RHE) under AM 1.5G solar light for the Au/Mo:$BiVO_4$ inverse opals with stop band reflection at 513 nm (macropore size of ca. 200 nm) matching closely the electronic band gap $BiVO_4$ and Au LSPR leading to a marked enhancement of light harvesting reflected in the corresponding IPCE spectra (Fig. 35).

Combined surface modification of $BiVO_4$ inverse opal powders fabricated by the ascorbic acid-assisted PMMA-templating method employing bismuth nitrate ($Bi(NO_3)_3{\cdot}5H_2O$) and ammonium metavanadate (NH_4VO_3) as metal sources [199] was demonstrated by Ji et al. [200] using silver bromide (AgBr) along with Pt, Au or Pd noble metal NPs at various loadings as co-catalysts. The ternary composite 0.17 wt% Pd /AgBr/$BiVO_4$ presented the highest performance on the degradation of 4-CP under visible-light, related to the beneficial synergy of visible light harvesting, transport and separation of photogenerated charges. Improvement of metal NPs' dispersion and bonding in $BiVO_4$ photonic crystals was recently investigated by Fang et al. [201] using pulsed current electrodeposition from $AgNO_3/NaNO_3$ aqueous solution for the fabrication of PBG engineered Ag/$BiVO_4$ inverse opals with stop band at ca. 415 nm (Fig. 36). Significant increments of the photocurrent density (nearly five-fold) and the visible light MB photocatalytic degradation rate in water (three-fold) were observed compared to disordered porous $BiVO_4$ films, attributed to the overlap of the stop band red edge at ~440 nm with the $BiVO_4$ absorption edge and the LSPR of the Ag NPs (size 25–30 nm).

Electrodeposition has been earlier applied by Nan et al. [202] to modify $BiVO_4$ inverse opals with carbon quantum dots as alternative, cost-effective sensitizers to metal NPs for PEC water splitting. Combination of carbon QDs' broadband optical absorption with red edge slow photons matching the $BiVO_4$ electronic absorption at ~450 nm, resulted in strong enhancement of the H_2 evolution rate and photoconversion efficiency to 0.35% (6-fold higher than that of plain spin coated $BiVO_4$ films), further assisted by the electron acceptor action of carbon QDs that suppress charge recombination at the QD/$BiVO_4$ photoelectrode.

Bismuth vanadate was further exploited as visible sensitizer of TiO_2 in order to improve charge separation and VLA photocatalytic performance. Heterojunction $BiVO_4/TiO_2$ photonic crystals were synthesized for the first time by Zalfani et al. [203] applying a hydrothermal treatment of TiO_2 inverse opal powders prepared from 350 nm PS colloidal templates with suitable metal-vanadate solutions at different molar ratios [204] leading to the dispersion of spherical $BiVO_4$ NPs

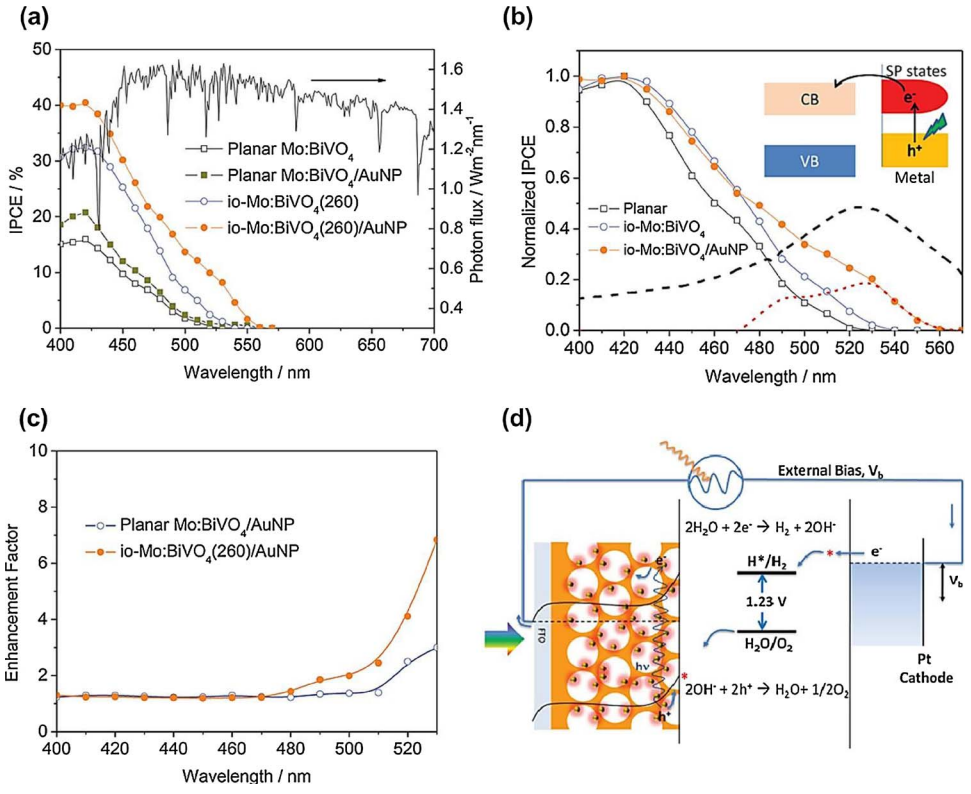

Fig. 35. Comparison of the IPCE spectra (a) before and (b) after normalization to the maximum value at 420 nm for the inverse opal (io) (260 nm PS template) and planar Mo:$BiVO_4$ electrodes modified by Au NPs, at 1.1 V vs RHE and AM 1.5 G solar light. Red and black dashed lines in (b) show the difference in the normalized IPCE after Au deposition and the 20 nm Au LSPR extinction, respectively. The inset depicts the LSPR-induced charge transfer mechanism. (c) IPCE enhancement factor for Au deposition over the unmodified inverse opal and planar photoelectrodes. (d) Schematic of solar water splitting mechanism in Au-Mo:$BiVO_4$ photoanodes [198]. Copyright © 2014 Wiley-VCH Verlag GmbH & Co. KGaA, Weinheim. (For interpretation of the references to colour in this figure legend, the reader is referred to the web version of this article.)

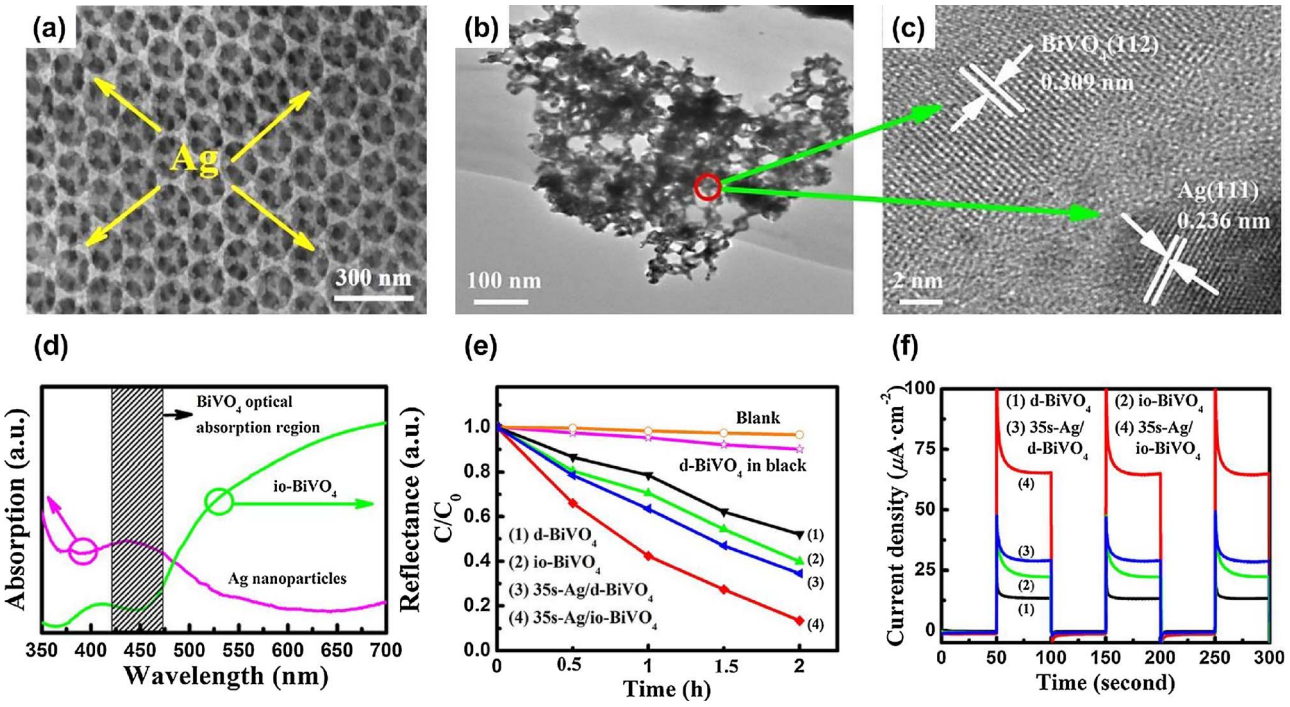

Fig. 36. (a) SEM, (b) TEM and (c) high resolution TEM images of the Ag/$BiVO_4$ inverse opals. (d) LSPR absorption of the Ag NPs electrodeposited onto FTO for 35 s and reflectance spectrum of the $BiVO_4$ inverse opal film. (e) MB photodegradation kinetics and (f) photocurrent density over the inverse opal and disordered porous $BiVO_4$ films before and after 35 s electrodeposition of Ag NPs [201]. Copyright © 2016 AIP Publishing LLC.

(70–90 nm) in the macroporous TiO_2 support. Significant enhancement has been achieved in the VLA aqueous phase RhB photocatalytic degradation for the 0.2 $BiVO_4/TiO_2$ composite due to the optimal assembly and favorably positioned band edges of the two constituent metal oxides promoting interfacial electron transfer from bismuth vanadate's conduction band to the lower energy titania's conduction band under visible light excitation.

Composite $Cr_2O_3/InVO_4$ and noble metal loaded $BiVO_4/InVO_4$ inverse opal powders with macropore sizes in the range of 100–200 nm were earlier fabricated by Dai and coworkers [205,206] leading to enhanced photocatalytic performance in the dye degradation of RhB and MB under visible light, surpassing pristine $InVO_4$ inverse opals [207]. Very recently, Zhang et al. [208] reported the modification of $BiVO_4$ inverse opal powders by iron oxide (Fe_2O_3) NPs using impregnation of ferric nitrate aqueous solution and subsequent post-annealing at 350 °C. Weak Fe_2O_3 loading of 0.97% resulted in the highest photocatalytic activity on 4-nitrophenol (4-NP) VLA photodegradation in the presence of H_2O_2 promoting ·OH radical formation via O_2 reduction by photogenerated electrons and via photo-Fenton process taking place on the iron oxide sensitizer.

Alternatively, Zhang et al. [209] reported the fabrication of a $BiVO_4$ photoanode utilizing a conductive Al-doped ZnO inverse opal network of 300 nm macropore size as electron collector to improve the inherently poor electron transport in bismuth vanadate, leading to a three-fold enhancement of the photocurrent density reaching 1.5 mA cm^{-2} at 1.23 V vs. RHE without any co-catalyst, compared to that of planar $BiVO_4$ photoanode. Very recently, a ternary nanocomposite $BiVO_4/TiO_2$/FTO core-shell inverse opal photoelectrode was fabricated by Zhang et al. [210] by the successive electrodeposition of a $BiVO_4$ film (~29 nm) over a thin (6 nm) TiO_2 layer that was deposited by ALD on a highly conductive F: SnO_2 (FTO) inverse opal of 290 nm initial macropore diameter prepared by FTO precursor infiltration in 408 nm PS colloidal opal templates, as shown in Fig. 37(a)–(d). In this innovative design, the periodically structured FTO inverse opals served as continuous porous support for the TiO_2 and $BiVO_4$ consecutive layers, affording improved light harvesting and fast electron transport, while TiO_2 acted as an electron scavenger to improve charge separation in the heterojunction with the visible light absorbing $BiVO_4$ layer, as shown in Fig. 37(e)–(g). A distinctly high photocurrent density of 4.11 mA cm^{-2} was thereby achieved at 1.23 V vs RHE under simulated AM 1.5G illumination in the presence of sodium sulphite as hole scavenger in the electrolyte. A nanocomposite $BiVO_4/WO_3$ inverse opal photoanode has been also implemented by Zhang et al. [211] using tungsten trioxide inverse opals of 300 nm average pore size and variable thickness (1.6–4.2 μm) onto which a $BiVO_4$ layer was electrodeposited leading to an increase of the wall thickness from 60 to 100 nm and a decrease of macropores size to 250 nm, while leaving intact the periodic structure. Further surface modification by the electrodeposition of cobalt-phosphate (Co-Pi) as water oxidation catalyst, resulted in a marked improvement of the AM 1.5 G photocurrent density to 4.5 mA cm^{-2} at 1.4 V versus Ag/AgCl. Although slow photons effects were hardly explored in these studies, the notably enhanced performance of these photonic materials validates the importance of the interconnected macroporous inverse opal networks in fostering highly efficient VLA photocatalysts and photoanodes for organics decomposition and water splitting.

5. Conclusions and future prospects

Based on the results reported to date (Tables 1 and 2), the establishment of photonic crystal structuring as an advanced structural modification for the development of high performance UV and more recently VLA semiconductor photocatalysts for water and air purification as well as PEC water splitting can be amply evinced. This highly promising approach can combine the unique potential for light harvesting, primarily by slow photon management, mass transport and adsorption of macroporous periodic structures like inverse opals with targeted compositional tuning of the photocatalysts' electronic properties for enhanced charge separation and visible light activation. Although the quality of materials' fabrication has been steadily increasing over the last few years, large-scale, robust synthesis especially as complexity in materials' design is continuously growing for

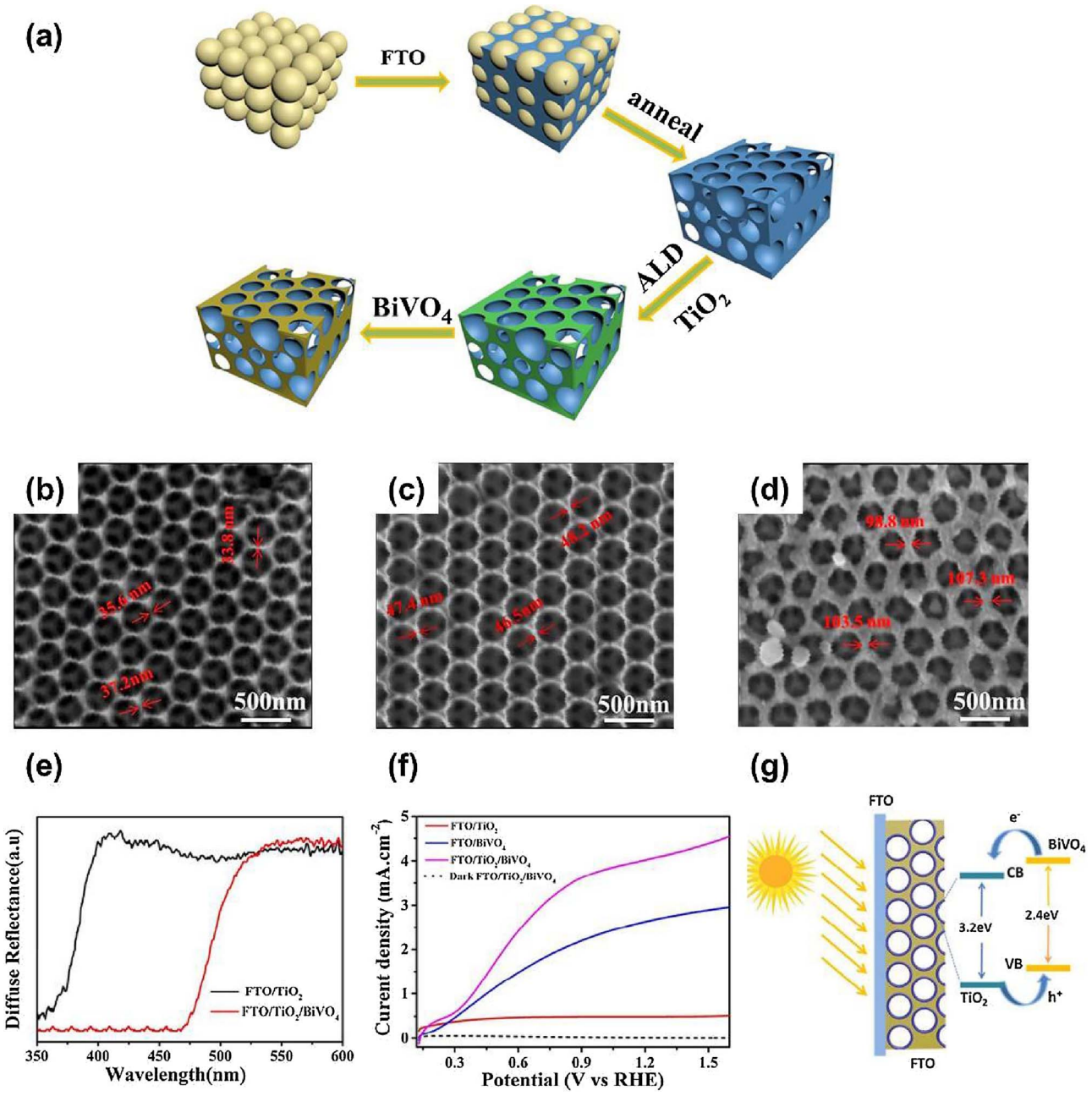

Fig. 37. (a) Schematic of the $BiVO_4/TiO_2$/FTO inverse opal photoelectrode fabrication. SEM images of (b) FTO (c) TiO_2/FTO and (d) $BiVO_4/TiO_2$/FTO inverse opals. (e) UV–vis diffuse reflectance spectra and (e) photocurrent density the ternary inverse opal and its constituent. (g) Scheme of the charge transfer mechanism for the $BiVO_4/TiO_2$/FTO composite photoanode [210]. Copyright © 2017 American Chemical Society.

heterostructured composites, remains the major challenge for the widespread use of photonic crystal photocatalysts in practical applications. The relatively limited deployment of co-assembly and co-deposition methods for the growth of large-area, crack-free and mechanically stable films, points out the need for further development and optimization of versatile deposition processes to establish firm structure-activity relations and address fabrication challenges. Furthermore, controlled synthesis of hierarchical macro/mesoporous inverse opal photocatalysts with tunable wall thickness, macropore interconnectivity and mesopore size by e.g. combinatorial colloidal crystal (hard) and surfactant (soft) template assembly [48] or multimodal colloidal crystal templates [212,213], would allow optimal synergy of morphological/photonic properties with compositional/electronic modifications and the efficient incorporation of functional materials (e.g. metals or narrow band semiconductor NPs) for tailor-designed VLA photonic catalysts.

Moreover, besides single layer inverse opals, the application of complex architectures such as multilayer stacks of 3D photonic crystals with different RI [214] and periodicity [215–218] remain largely unexplored in VLA photocatalysis. Successful implementation of the challenging fabrication of such structures with tailored photonic and electronic properties could pave the way for advanced photon management and resonant light confinement mimicking optical microcavities [219]. PBG engineering of self-ordered titania nanotubes, whose growth and modifications by electrochemical anodization of metallic Ti substrates has reached an advanced development stage [220] could also provide fertile ground for rationally designed photonic structures beyond inverse opals, featuring scalable fabrication together with high structural and optical quality [221–223].

In the last few years, there has been a rapid expansion in the

materials selected for the fabrication of non-TiO_2 photonic crystals ranging from UV activated wide band semiconductors such as ZnO, Ga_2O_3 and $ZnGa_2O_4$ to alternative VLA ones like α-Fe_2O_3, WO_3, Bi_2O_3 or ternary metal oxides e.g. Bi_2WO_6 and $BiVO_4$, where further development and performance optimization, especially with regard to the identification and exploitation of slow photon effects, can be projected in the near future. Following the distinct strategies currently pursued for VLA titania photocatalysts, significant, though not extensive, research efforts have been devoted to anion and self-doping of TiO_2 photonic crystals as well as to heterostructuring with metal NPs and visible light active nanomaterials like graphene, quantum dots and other narrow band semiconductors. Nevertheless, further work on the enhancement of visible light harvesting is still pending, especially with respect to the optimal synergy of plasmonic effects with slow photons in PBG engineered photonic crystals. In addition, a wide range of potential photocatalysts and co-catalysts for solar water splitting [224], especially earth abundant VLA materials e.g. metal sulfides, nitrides, ferrites and metallic alloys [225,226] or 2D nanoporous materials [227] that could sustain substantial RI contrasts (> 2.0) for standalone photonic structures or as VLA sensitizers and co-catalysts of titania or other photocatalytic substrates could be profitably exploited in photonic crystal-assisted VLA photocatalysis.

An important aspect for technological applications is that performance evaluation of the photonic photocatalysts has been largely conducted using dye probe molecules (Tables 1 and 2), which, except for the ease in spectrophotometric detection as well as their visible absorbance that allows identifying slow photon effects, are not well suited as model contaminants for the evaluation of photocatalytic activity of novel VLA photocatalysts due the self-sensitization effect [228]. In addition, toxicity and biocompatibility evaluation of the photonic photocatalysts as well as identification of reaction by-products has been scarcely reported. Analytical evaluation of the materials' photocatalytic efficiency, stability and reusability along with toxicity studies should be accordingly extended to classical water pollutants as well as contaminants of emerging concern in comparison with benchmark P25 films for UV–vis or solar applications in order to optimize materials performance and validate their competence on water treatment and environmental remediation.

Furthermore, rigorous electrodynamic photonic band structure calculations that include the materials's optical absorption as well as the contribution of film thickness and disorder in combination with the investigation of transport processes in the periodic porous structure and the elucidation of the ROS involved in the photocatalytic process could step up the design and fabrication of advanced VLA photocatalysts. Nonetheless, despite the existing challenges in this relatively new direction in semiconductor photocatalysis, the progress made to date, especially within the last few years, emphasizes the great potential of photonic crystal nanostructures for VLA photocatalysis and solar-to-chemical-energy conversion applications, where significant advancements could be anticipated in the near future.

Acknowledgment

The current work was funded by the Research Projects For Excellence IKY/SIEMENS.

References

[1] A. Fujishima, X. Zhang, D.A. Tryk, Surf. Sci. Rep. 63 (2008) 515–582.
[2] J. Schneider, D. Bahnemann, J. Ye, G. Li Puma, D.D. Dionysiou (Eds.), RSC Energy and Environment Series No. 14, Photocatalysis: Fundamentals and Perspectives, The Royal Society of Chemistry, 2016.
[3] V. Likodimos, D.D. Dionysiou, P. Falaras, Rev. Environ. Sci. Biotechnol. 9 (2010) 87–94.
[4] J. Schneider, M. Matsuoka, M. Takeuchi, J. Zhang, Y. Horiuchi, M. Anpo, D.W. Bahnemann, Chem. Rev. 114 (2014) 9919–9986.
[5] Y. Ma, X. Wang, Y. Jia, X. Chen, H. Han, C. Li, Chem. Rev. 114 (2014) 9987–10043.
[6] S. Loeb, R. Hofmann, J.-H. Kim, Environ. Sci. Technol. Lett. 3 (2016) 73–80.
[7] F.C. Moreira, R.A.R. Boaventura, E. Brillas, V.J.P. Vilar, Appl. Catal. B: Environ. 202 (2017) 217–261.
[8] X. Chen, A. Selloni, Chem. Rev. 114 (2014) 9281–9282.
[9] A.V. Emeline, X. Zhang, M. Jin, T. Murakami, A. Fujishima, J. Phys. Chem. B 110 (2006) 7409–7413.
[10] B.S. Liu, X.J. Zhao, C. Terashima, A. Fujishima, K. Nakata, Phys. Chem. Chem. Phys. 16 (2014) 8751–8760.
[11] M. Pelaez, N.T. Nolan, S.C. Pillai, M.K. Seery, P. Falaras, A.G. Kontos, P.S.M. Dunlop, J.W.J. Hamilton, J.A. Byrne, K. O'Shea, M.H. Entezari, D.D. Dionysiou, Appl. Catal. B: Environ. 125 (2012) 331–349.
[12] S. Banerjee, S.C. Pillai, P. Falaras, K.E. O'Shea, J.A. Byrne, D.D. Dionysiou, J. Phys. Chem. Lett. 5 (2014) 2543–2554.
[13] R. Asahi, T. Morikawa, H. Irie, T. Ohwaki, Chem. Rev. 114 (2014) 9824–9852.
[14] S. Linic, P. Christopher, D.B. Ingram, Nat. Mater. 10 (2011) 911–921.
[15] X. Zhang, Y.L. Chen, R.-S. Liu, D.P. Tsai, Rep. Prog. Phys. 76 (2013) 046401.
[16] H. Tong, S. Ouyang, Y. Bi, N. Umezawa, M. Oshikiri, J. Ye, Adv. Mater. 24 (2012) 229–251.
[17] H. Tada, Q. Jin, A. Iwaszuk, M. Nolan, J. Phys. Chem. C 118 (2014) 12077–12086.
[18] L.M. Pastrana-Martínez, S. Morales-Torres, V. Likodimos, J.L. Figueiredo, J.L. Faria, P. Falaras, A.M.T. Silva, Appl. Catal. B: Environ. 123 − 124 (2012) 241–256.
[19] S.M. Miranda, G.E. Romanos, V. Likodimos, R.R.N. Marques, E.P. Favvas, F.K. Katsaros, K.L. Stefanopoulos, V.J.P. Vilar, J.L. Faria, P. Falaras, A.M.T. Silva, Appl. Catal. B: Environ. 147 (2014) 65–81.
[20] L. Liu, X. Chen, Chem. Rev. 114 (2014) 9890–9918.
[21] D.O. Scanlon, C.W. Dunnill, J. Buckeridge, S.A. Shevlin, A.J. Logsdail, S.M. Woodley, C.R.A. Catlow, M.J. Powell, R.G. Palgrave, I.P. Parkin, G.W. Watson, T.W. Keal, P. Sherwood, A. Walsh, A.A. Sokol, Nat. Mater. 12 (2013) 798–801.
[22] V. Pfeifer, P. Erhart, S. Li, K. Rachut, J. Morasch, J. Broetz, P. Reckers, T. Mayer, S. Ruehle, A. Zaban, I. Mora-Seró, J. Bisquert, W. Jaegermann, A. Klein, J. Phys. Chem. Lett. 4 (2013) 4182–4187.
[23] V. Likodimos, A. Chrysi, M. Calamiotou, C. Fernández-Rodríguez, J.M. Doña-Rodríguez, D.D. Dionysiou, P. Falaras, Appl. Catal. B: Environ. 192 (2016) 242–252.
[24] X. Chen, L. Liu, P.Y. Yu, S.S. Mao, Science 331 (2011) 746–750.
[25] J. Tao, T. Luttrell, M. Batzill, Nat. Chem. 3 (2011) 296–300.
[26] H.G. Yang, C.H. Sun, S.Z. Qiao, J. Zou, G. Liu, S.C. Smith, H.M. Cheng, G.Q. Lu, Nature 453 (2008) 638–641.
[27] V. Likodimos, C. Han, M. Pelaez, A.G. Kontos, G. Liu, D. Zhu, S. Liao, A.A. de la Cruz, K. O'Shea, P.S.M. Dunlop, J.A. Byrne, D.D. Dionysiou, P. Falaras, Ind. Eng. Chem. Res. 52 (2013) 13957–13964.
[28] X. Chen, L. Liu, F. Huang, Chem. Soc. Rev. 44 (2015) 1861–1885.
[29] X. Liu, G. Zhu, X. Wang, X. Yuan, T. Lin, F. Huang, Adv. Energy Mater. 6 (2016) 1600452.
[30] Q. Jin, H. Yamamoto, K. Yamamoto, M. Fujishima, H. Tada, Phys. Chem. Chem. Phys. 15 (2013) 20313–20319.
[31] X. Meng, L. Liu, S. Ouyang, H. Xu, D. Wang, N. Zhao, J. Ye, Adv. Mater. 28 (2016) 6781–6803.
[32] V. Etacheri, C. Di Valentin, J. Schneider, D. Bahnemann, S.C. Pillai, J. Photochem. Photobiol. C 25 (2015) 1–29.
[33] H. Irie, Y. Watanabe, K. Hashimoto, J. Phys. Chem. B 107 (2003) 5483–5486.
[34] M. Pelaez, P. Falaras, V. Likodimos, K. O'Shea, A.A. de la Cruz, P.S.M. Dunlop, J.A. Byrne, D.D. Dionysiou, J. Mol. Catal. A 425 (2016) 183–189.
[35] L.M. Pastrana-Martinez, S. Morales-Torres, A.G. Kontos, N.G. Moustakas, J.L. Faria, J.M. Dona-Rodriguez, P. Falaras, A.M.T. Silva, Chem. Eng. J. 224 (2013) 17–23.
[36] X. Wang, Z. Li, J. Shi, Y. Yu, Chem. Rev. 114 (2014) 9346–9384.
[37] X. Zhou, Ning Liu, Patrik Schmuki, ACS Catal. 7 (2017) 3210–3235.
[38] S. Liu, J. Yu, M. Jaroniec, Chem. Mater. 23 (2011) 4085–4093.
[39] A.A. Ismail, D.W. Bahnemann, J. Mater. Chem. 21 (2011) 11686–11707.
[40] H. Choi, A.C. Sofranko, D.D. Dionysiou, Adv. Funct. Mater. 16 (2006) 1067–1074.
[41] M. Pelaez, A.A. de la Cruz, E. Stathatos, P. Falaras, D.D. Dionysiou, Catal. Today 144 (2009) 19–25.
[42] M. Pelaez, P. Falaras, V. Likodimos, A.G. Kontos, A. De la Cruz, K. O'shea, D.D. Dionysiou, Appl. Catal. B: Environ. 99 (2010) 378–387.
[43] C. Han, J. Andersen, V. Likodimos, P. Falaras, J. Linkugel, D.D. Dionysiou, Catal. Today 224 (2014) 132–139.
[44] G. Liu, C. Han, M. Pelaez, D. Zhu, S. Liao, V. Likodimos, N. Ioannidis, A.G. Kontos, P. Falaras, P.S.M. Dunlop, J.A. Byrne, D.D. Dionysiou, Nanotechnology 23 (2012) 294003.
[45] J.C. Yu, L. Zhang, Z. Zheng, J. Zhao, Chem. Mater. 15 (2003) 2280–2286.
[46] J.A. Khan, C. Han, N.S. Shah, H.M. Khan, M.N. Nadagouda, V. Likodimos, P. Falaras, K. O'Shea, D.D. Dionysiou, Environ. Eng. Sci. 31 (2014) 435–446.
[47] X. Li, J. Yu, M. Jaroniec, Chem. Soc. Rev. 45 (2016) 2603–2636.
[48] N.D. Petkovich, A. Stein, Chem. Soc. Rev. 42 (2013) 3721–3739.
[49] D. Fattakhova-Rohlfing, A. Zaleska, T. Bein, Chem. Rev. 114 (2014) 9487–9558.
[50] X.-Y. Yang, L.-H. Chen, Y. Li, J.C. Rooke, C. Sanchez, B.-L. Su, Chem. Soc. Rev. 46 (2017) 481–558.
[51] J.I. Chen, G. von Freymann, S.Y. Choi, V. Kitaev, G.A. Ozin, Adv.Mater. 18 (2006) 1915–1919.
[52] J.E. Armstrong, C. O'Dwyer, Mater. Chem. C 3 (2015) 6109–6143.
[53] M. Curti, J. Schneider, D.W. Bahnemann, C.B. Mendive, J. Phys. Chem. Lett. 6 (2015) 3903–3910.
[54] G. von Freymann, V. Kitaev, B.V. Lotschz, G.A. Ozin, Chem. Soc. Rev. 42 (2013)

2528–2554.
[55] F. Marlow, P. Muldarisnur, R. Sharifi, C. Brinkmann, Mendive, Angew. Chem. 121 (2009) 6328–6333.
[56] A. Stein, B.E. Wilson, S.G. Rudisill, Chem. Soc. Rev. 42 (2013) 2763–2803.
[57] N. Vogel, M. Retsch, C.-A. Fustin, A. del Campo, U. Jonas, Chem. Rev. 115 (2015) 6265–6311.
[58] K.R. Phillips, G.T. England, S. Sunny, E. Shirman, T. Shirman, N. Vogel, J. Aizenberg, Chem. Soc. Rev. 45 (2016) 281–322.
[59] X. Zheng, L. Zhang, Energy Environ. Sci. 9 (2016) 2511–2532.
[60] G. Collins, E. Armstrong, D. McNulty, S. O'Hanlon, H. Geaney, C. O'Dwyer, Sci. Technol. Adv. Mater. 17 (2016) 565–582.
[61] J.J. Pietron, P.A. DeSario, J. Photon Energy 7 (2016) 012007.
[62] J. Liu, H. Zhao, M. Wu, B. Van der Schueren, Y. Li, O. Deparis, J. Ye, G.A. Ozin, T. Hasan, B.-L. Su, Adv. Mater. 29 (2017) 1605349.
[63] R. Raccis, A. Nikoubashman, M. Retsch, U. Jonas, K. Koynov, H.-J. Butt, C.N. Likos, G. Fytas, ACS Nano 5 (2011) 4607–4616.
[64] E. Yablonovitch, Phys. Rev. Lett. 58 (1987) 2059–2062.
[65] S. John, Phys. Rev. Lett. 58 (1987) 2486–2489.
[66] J.D. Joannopoulos, S.G. Johnson, J.N. Winn, R.D. Meade, Photonic Crystals: Molding the Flow of Light, Princeton University Press, 2008.
[67] K.-M. Ho, C.T. Chan, C.M. Soukoulis, Phys. Rev. Lett. 65 (1990) 3152–3155.
[68] E. Yablonovitch, T.J. Gmitter, K.M. Leung, Phys. Rev. Lett. 67 (1991) 2295–2298.
[69] S.Y. Lin, J.G. Fleming, D.L. Hetherington, B.K. Smith, R. Biswas, K.M. Ho, M.M. Sigalas, W. Zubrzycki, S.R. Kurtz, J. Bur, Nature 394 (1998) 251–253.
[70] D.J. Norris, Y.A. Vlasov, Adv. Mater. 13 (2001) 371–376.
[71] A. Toumazatou, M.K. Arfanis, P.-A. Pantazopoulos, A.G. Kontos, P. Falaras, N. Stefanou, V. Likodimos, Mater. Lett. 197 (2017) 123–126.
[72] K. Busch, S. John, Phys. Rev. E 58 (1998) 3896–3908.
[73] A. Blanco, E. Chomski, S. Grabtchak, M. Ibisate, S. John, S.W. Leonard, C. Lopez, F. Meseguer, H. Miguez, J.P. Mondia, G.A. Ozin, O. Toader, H.-M. van Driel, Nature 405 (2000) 437–440.
[74] Y. Vlasov, X. Bo, J.C. Sturm, D.J. Norris, Nature 414 (2001) 289–293.
[75] B.T. Holland, C.F. Blanford, A. Stein, Science 281 (1998) 538–540.
[76] J.E.G.J. Wijnhoven, W.L. Vos, Science 281 (1998) 802–804.
[77] D. Qi, L. Lu, L. Wang, J. Zhang, J. Am. Chem. Soc. 136 (2014) 9886–9889.
[78] X. Zheng, S. Meng, J. Chen, J. Wang, J. Xian, Y. Shao, X. Fu, D. Li, J. Phys. Chem. C 117 (2013) 21263–21273.
[79] R.M. Pasquarelli, H.S. Lee, R. Kubrin, R. Zierold, A.Yu. Petrov, K. Nielsch, G.A. Schneider, M. Eich, R. Janssen, J. Eur. Ceram. Soc. 35 (2015) 3103–3109.
[80] B. Hatton, L. Mishchenko, S. Davis, K.H. Sandhage, J. Aizenberg, PNAS 107 (2010) 10354–10359.
[81] Q.B. Meng, C.H. Fu, Y. Einaga, Z.Z. Gu, A. Fujishima, O. Sato, Chem. Mater. 14 (2002) 83–88.
[82] Y.G. Seo, K. Woo, J. Kim, H. Lee, W. Lee, Adv. Funct. Mater. 21 (2011) 3094–3103.
[83] D.P. Gaillot, C.J. Summers, N. Pinna, M. Knez (Eds.), Atomic Layer Deposition of Nanostructured Materials, 1st edn., Wiley-VCH, Weinheim, 2011.
[84] J.S. King, E. Graugnard, C.J. Summers, Adv. Mater. 17 (2005) 1010–1013.
[85] G.E. Jellison, L.A. Boatner, J.D. Budai, B.-S. Jeong, D.P. Norton, J. Appl. Phys. 93 (2003) 9537–9541.
[86] T.E. Tiwald, M. Schubert, Proc. SPIE 4103 (2000) 19–29.
[87] J.-P. Jalava, V.-M. Taavitsainen, R.-J. Lamminmäki, M. Lindholm, S. Auvinen, M. Alatalo, E. Vartiainen, H. Haario, J. Quant. Spectrosc. Radiat. Transf. 167 (2015) 105–118.
[88] G.I.N. Waterhouse, M.R. Waterland, Polyhedron 26 (2007) 356–368.
[89] N. Stefanou, V. Yannopoulos, A. Modinos, Comput. Phys. Commun. 113 (1998) 49–77.
[90] N. Stefanou, V. Yannopapas, A. Modinos, Comput. Phys. Commun. 132 (2000) 189–196.
[91] R.C. Schroden, M. Al-Daous, C.F. Blanford, A. Stein, Chem. Mater. 14 (2002) 3305–3315.
[92] S. Datta, C.T. Chan, K.M. Ho, C.M. Soukoulis, Phys. Rev. B 48 (1993) 14936–14943.
[93] V. Jovic, H. Idriss, G.I.N. Waterhouse, Chem. Phys. 479 (2016) 109–121.
[94] S. Nishimura, N. Abrams, B.A. Lewis, L.I. Halaoui, T.E. Mallouk, K.D. Benkstein, J. van de Lagemaat, A.J. Frank, J. Am. Chem. Soc. 125 (2003) 6306–6310.
[95] E. Yablonovitch, Sci. Am. 285 (2001) 47–55.
[96] L.I. Halaoui, N. Abrams, T.E. Mallouk, J. Phys. Chem. B 109 (2005) 6334–6342.
[97] A. Mihi, H. Miguez, J. Phys. Chem. B 109 (2005) 15968–15976.
[98] S. Guldin, S. Huttner, M. Kolle, M.E. Welland, P. Muller-Buschbaum, R.H. Friend, U. Steiner, N. Tetreault, Nano Lett. 10 (2010) 2303–2309.
[99] A. Imhof, W.L. Vos, R. Sprik, A. Lagendijk, Phys. Rev. Lett. 83 (1999) 2942–2945.
[100] G. von Freymann, S. John, S. Wong, V. Kitaev, G.A. Ozin, Appl. Phys. Lett. 86 (2005) 053108.
[101] J.F. Galisteo-López, M. Galli, M. Patrini, A. Balestreri, L.C. Andreani, C. López, Phys. Rev. B 73 (2006) 125103.
[102] J.F. Galisteo-López, E. Palacios-Lidón, E. Castillo-Martínez, C. López, Phys. Rev. B 68 (2003) 115109.
[103] S.G. Romanov, T. Maka, C.M. Sotomayor Torres, M. Müller, R. Zentel, D. Cassagne, J. Manzanares-Martinez, C. Jouanin, Phys. Rev. E 63 (2001) 056603.
[104] J.I.L. Chen, G. von Freymann, V. Kitaev, G.A. Ozin, J. Am. Chem. Soc. 129 (2007) 1196–1202.
[105] J. Liu, M.Z. Li, J.X. Wang, Y.L. Song, L. Jiang, T. Murakami, A. Fujishima, Environ. Sci. Technol. 43 (2009) 9425–9431.
[106] J.I.L. Chen, G.A. Ozin, J. Mater. Chem. 19 (2009) 2675–2678.
[107] W. Liu, B. Zou, J. Zhao, H. Cui, Thin Solid Films 518 (2010) 4923–4927.
[108] M. Srinivasn, T. White, Environ. Sci. Technol. 41 (2007) 4405–4409.
[109] M. Wu, Y. Li, Z. Deng, B.-L. Su, ChemSusChem 4 (2011) 1481–1488.
[110] F. Sordello, C. Duca, V. Maurino, C. Minero, Chem. Commun. 47 (2011) 6147–6149.
[111] M. Wu, A.M. Zheng, F. Deng, B.L. Su, Appl. Catal. B: Environ. 138–139 (2013) 219–228.
[112] M. Wu, J. Jin, J. Liu, Z. Deng, Y. Li, O. Deparis, B.-L. Su, J. Mater. Chem. A 1 (2013) 15491–15500.
[113] M. Wu, J. Liu, J. Jin, C. Wang, S. Huang, Z. Deng, Y. Li, B.-L. Su, Appl. Catal. B: Environ. 150–151 (2014) 411–420.
[114] O. Deparis, S.R. Mouchet, B.L. Su, Phys. Chem. Chem. Phys. 17 (2015) 30525–30532.
[115] M. Ren, R. Ravikrishna, K.T. Valsaraj, Environ. Sci. Technol. 40 (2006) 7029–7033.
[116] M. Curti, C.B. Mendive, M.A. Grela, D.W. Bahnemann, Mater. Res. Bull. 91 (2017) 155–165.
[117] T. Cherdhirankorn, M. Retsch, U. Jonas, H.-J. Butt, K. Koynov, Langmuir 26 (2010) 10141–10146.
[118] S.-L. Chen, A.-J. Wang, C.-T. Hu, C. Dai, J.B. Benziger, AIChE J. 58 (2012) 568–572.
[119] S.-L. Chen, A.-J. Wang, C. Dai, J.B. Benziger, X.-C. Liu, Chem. Eng. J. 249 (2014) 48–53.
[120] P. Li, S.-L. Chen, A.-J. Wang, Y. Wang, Chem. Eng. J. 284 (2016) 305–314.
[121] E. Eftekhari, P. Broisson, N. Aravindakshan, Z. Wu, I.S. Cole, X. Li, D. Zhao, Q. Li, J. Mater. Chem. A 5 (2017) 12803–12810.
[122] A. Janotti, C.G. Van de Walle, Rep. Prog. Phys. 72 (2009) 126501.
[123] K.M. Lee, C.W. Lai, K.S. Ngai, J.C. Juan, Water Res. 88 (2016) 428–448.
[124] S. Meng, D. Li, X. Zheng, J. Wang, J. Chen, J. Fang, Y. Shao, X. Fu, J. Mater. Chem. A 1 (2013) 2744–2747.
[125] J. Liu, J. Jin, Y. Li, H.-W. Huang, C. Wang, M. Wu, L.-H. Chen, B.-L. Su, J. Mater. Chem. A 2 (2014) 5051–5059.
[126] F. Sordello, V. Maurino, C. Minero, J. Mater. Chem. 21 (2011) 19144–19152.
[127] X. Li, X. Zhen, S. Meng, J. Xian, Y. Shao, X. Fu, D. Li, Environ. Sci. Technol. 47 (2013) 9911–9917.
[128] X. Li, X. Zhang, X. Zheng, Y. Shao, M. He, P. Wang, X. Fu, D. Li, J. Mater. Chem. A 2 (2014) 15796–15802.
[129] I.K. Konstantinou, T.A. Albanis, Appl. Catal. B: Environ. 49 (2004) 1–14.
[130] D. Chatterjee, S. Dasgupta, J. Photochem. Photobiol. C: Photochem. Rev. 6 (2005) 186–205.
[131] Md.K. Nazeeruddin, E. Baranoff, M. Gratzel, Solar Energy 85 (2011) 1172–1178.
[132] K. Rajeshwar, M.E. Osugi, W. Chanmanee, C.R. Chenthamarakshan, M.V.B. Zanoni, P. Kajitvichyanukul, R. Krishnan-Aye, J. Photochem. Photobiol. C: Photochem. Rev. 9 (2008) 171–192.
[133] S. Meng, D. Li, P. Wang, X. Zheng, J. Wang, J. Chen, J. Fang, X. Fu, RSC Adv. 3 (2013) 17021–17028.
[134] V. Likodimos, M. Labardi, L. Pardi, M. Allegrini, M. Giordano, A. Arena, S. Patanè, Appl. Phys. Lett. 82 (2003) 3313–3315.
[135] J.I.L. Chen, G.A. Ozin, Adv. Mater. 20 (2008) 4784–4788.
[136] Y. Li, T. Kunitake, S. Fujikawa, J. Phys. Chem. B 110 (2006) 13000–13004.
[137] X. Zheng, D. Li, X. Li, L. Yu, P. Wang, X. Zhang, J. Fang, Y. Shao, Y. Zheng, Phys. Chem. Chem. Phys. 16 (2014) 15299–15306.
[138] C.B. Mendive, D. Hansmann, T. Bredow, D. Bahnemann, J. Phys. Chem. C 115 (2011) 19676–19685.
[139] Q. Li, J.K. Shang, J. Am. Ceram. Soc. 91 (2008) 660–663.
[140] Z. Hu, L. Xu, J. Chen, Mater. Lett. 106 (2013) 421–424.
[141] S.-J. Ha, D.H. Kim, J.H. Moon, RSC Adv. 5 (2015) 77716–77722.
[142] Z.Y. Hu, L.B. Xu, L.L. Wang, Y. Huang, L.M. Xu, J.F. Chen, Catal. Commun. 40 (2013) 106–110.
[143] J. Xu, B. Yang, M. Wu, Z. Fu, Y. Lv, Y. Zhao, J. Phys. Chem. C 114 (2010) 15251–15259.
[144] C. Di Valentin, E. Finazzi, G. Pacchioni, A. Selloni, S. Livraghi, A.M. Czoska, M.C. Paganini, E. Giamello, Chem. Mater. 20 (2008) 3706–3714.
[145] T.K. Rahul, N. Sandhyarani, Nanoscale 7 (2015) 18259–18270.
[146] D.Y. Qi, L. Lu, Z. Xi, L. Wang, J. Zhang, Appl. Catal. B: Environ. 160–161 (2014) 621–628.
[147] L. Xin, X. Liu, RSC Adv. 5 (2015) 71547–71550.
[148] O. Carp, C.L. Huisman, A. Reller, Prog. Solid State Chem. 32 (2004) 33–177.
[149] J.I.L. Chen, E. Loso, N. Ebrahim, G.A. Ozin, J. Am. Chem. Soc. 130 (2008) 5420–5421.
[150] M. Ren, K. Valsaraj, Int. J. Chem. React. Eng. 7 (2009) A90.
[151] H. Chen, S. Chen, X. Quan, Y. Zhang, Environ. Sci. Technol. 14 (2010) 451–455.
[152] J. Liu, G. Liu, M. Li, W. Shen, Z. Liu, J. Wang, J. Zhao, L. Jiang, Y. Song, Energy Environ. Sci. 3 (2010) 1503–1506.
[153] G.I.N. Waterhouse, A.K. Wahab, V. Jovic, D.H. Anjum, J. Llorca, H. Idriss, Sci. Rep. 3 (2013) 2894.
[154] F. Sordello, C. Minero, Appl. Catal. B: Environ. 163 (2015) 452–458.
[155] Z. Cai, Z. Xiong, X. Lu, J. Teng, J. Mater. Chem. A 2 (2014) 545–553.
[156] K. Awazu, M. Fujimaki, C. Rockstuhl, J. Tominaga, H. Murakami, Y. Ohki, N. Yoshida, T. Watanabe, J. Am. Chem. Soc. 130 (2008) 1676–1680.
[157] C. Clavero, Nat. Photon. 8 (2014) 95–103.
[158] X.-C. Ma, Y. Dai, L. Yu, B.-B. Huang, Light: Sci. Appl. 5 (2016) e16017.
[159] Y. Lu, H. Yu, S. Chen, X. Quan, H. Zhao, Environ. Sci. Technol. 46 (2012) 1724–1730.
[160] K. Kim, P. Thiyagarajan, H.-J. Ahn, S.-I. Kim, J.-H. Jang, Nanoscale 5 (2013) 6254–6260.
[161] X. Zhang, Y. Liu, S.-T. Lee, S. Yang, Z. Kang, Energy Environ. Sci. 7 (2014) 1409–1419.

[162] Y. Zhao, B. Yang, J. Xu, Z. Fu, M. Wu, F. Li, Thin Solid Films 520 (2012) 3515–3522.
[163] S. Meng, D. Li, X. Fu, X. Fu, J. Mater. Chem. A 3 (2015) 23501–23511.
[164] C.W. Cheng, S.K. Karuturi, L.J. Liu, J.P. Liu, H.X. Li, L.T. Su, A.I.Y. Tok, H.J. Fan, Small 8 (2012) 37–42.
[165] H. Zhao, M. Wu, J. Liu, Z. Deng, Y. Li, B.-L. Su, Appl. Catal. B: Environ. 184 (2016) 182–190.
[166] J. Lee, C.-Y. Cho, D.C. Lee, J.H. Moon, RSC Adv. 6 (2016) 8756–8762.
[167] R. Mitchell, R. Brydson, R.E. Douthwaite, Phys. Chem. Chem. Phys. 17 (2015) 493–499.
[168] S. Guo, D. Li, Y. Zhang, Y. Zhang, X. Zhou, Electrochim. Acta 121 (2014) 352–360.
[169] C. Li, X. Zhu, H. Zhang, Z. Zhu, B. Liu, C. Cheng, Adv. Mater. Interfaces 2 (2015) 1500428.
[170] Y. Chang, K. Yu, C. Zhang, Z. Yang, Y. Feng, H. Hao, Y. Jiang, L.-L. Lou, W. Zhou, S. Liu, Appl. Catal. B: Environ. 215 (2017) 74–84.
[171] K. Yu, C. Zhang, Y. Chang, Y. Feng, Z. Yang, T. Yang, L.-L. Lou, S. Liu, Appl. Catal. B: Environ. 200 (2017) 514–520.
[172] Z. Geng, Y. Zhang, X. Yuan, M. Huo, Y. Zhao, Y. Lu, Y. Qiu, J. Alloys Compd. 644 (2015) 734–741.
[173] X. Zheng, D. Li, X. Li, J. Chen, C. Cao, J. Fang, J. Wang, Y. He, Y. Zheng, Appl. Catal. B: Environ. 168–169 (2015) 408–415.
[174] M. Zalfani, B. van der Schueren, M. Mahdouani, R. Bourguiga, W.B. Yu, M. Wu, O. Deparis, Y. Li, B.L. Su, Appl. Catal. B: Environ. 199 (2016) 187–198.
[175] S.K. Karuturi, C. Cheng, L. Liu, L.T. Su, H.J. Fan, A.I.Y. Tok, Nano Energy 1 (2012) 322–327.
[176] X. Huang, X. Qi, F. Boey, H. Zhang, Chem. Soc. Rev. 41 (2012) 666–686.
[177] S. Morales-Torres, L.M. Pastrana-Martínez, J.L. Figueiredo, J.L. Faria, A.M.T. Silva, Environ. Sci. Pollut. Res. 19 (2012) 3676–3687.
[178] W.G. Tu, Y. Zhou, Z.G. Zou, Adv. Funct. Mater. 23 (2013) 4996–5008.
[179] L.M. Pastrana-Martínez, S. Morales-Torres, V. Likodimos, P. Falaras, J.L. Figueiredo, J.L. Faria, A.M.T. Silva, Appl. Catal. B: Environ. 158–159 (2014) 329–340.
[180] J. Du, X. Lai, N. Yang, J. Zhai, D. Kisailus, F. Su, D. Wang, L. Jiang, ACS Nano 5 (2011) 590–596.
[181] K.-Y. Yoon, J.-S. Lee, K. Kim, C.H. Bak, S.-I. Kim, J.-B. Kim, J.-H. Jang, ACS Appl. Mater. Interfaces 6 (2014) 22634–22639.
[182] R. Boppella, S.T. Kochuveedu, H. Kim, M.J. Jeong, F.M. Mota, J.H. Park, D.H. Kim, ACS Appl. Mater. Interfaces 9 (2017) 7075–7083.
[183] S. Lee, Y. Lee, D.H. Kim, J.H. Moon, ACS Appl. Mater. Interfaces 5 (2013) 12526–12532.
[184] G. Liao, S. Chen, X. Quan, H. Chen, Y. Zhang, Environ. Sci. Technol. 44 (2010) 3481–3485.
[185] H. Xie, Y. Li, S. Jin, J. Han, X. Zhao, J. Phys. Chem. C 114 (2010) 9706–9712.
[186] M. Sadakane, K. Sasaki, H. Kunioku, B. Ohtani, R. Abe, W. Ueda, J. Mater. Chem. 20 (2010) 1811–1818.
[187] X. Chen, J. Ye, S. Ouyang, T. Kako, Z. Li, Z. Zou, ACS Nano 5 (2011) 4310–4318.
[188] X. Li, Z. Chen, H. Quan, Y. Shao, D. Li, J. Porous Mater. (2017), http://dx.doi.org/10.1007/s10934-017-0480-4.
[189] N.J. Cherepy, D.B. Liston, J.A. Lovejoy, H. Deng, J.Z. Zhang, J. Phys. Chem. B 102 (1998) 770–776.
[190] A. Duret, M. Grätzel, J. Phys. Chem. B 109 (2005) 17184–17191.
[191] Y. Chang, K. Yu, C. Zhang, R. Li, P. Zhao, L.-L. Lou, S. Liu, Appl. Catal. B: Environ. 176–177 (2015) 363–373.
[192] Z. Yi, J. Ye, N. Kikugawa, T. Kako, S. Ouyang, H. Stuart-Williams, H. Yang, J. Cao, W. Luo, Z. Li, Y. Liu, R.L. Withers, Nat. Mater. 9 (2010) 559–564.
[193] Y.P. Liu, L. Fang, H.D. Lu, Y.W. Li, C.Z. Hu, H.G. Yu, Appl. Catal. B: Environ. 115–116 (2012) 245–252.
[194] C. Zhang, K. Yu, Y. Feng, Y. Chang, T. Yang, Y. Xuan, D. Lei, L.-L. Lou, S. Liu, Appl. Catal. B: Environ. 210 (2017) 77–87.
[195] A. Kubacka, M. Fernandez-García, G. Colon, Chem. Rev. 112 (2012) 1555–1614.
[196] L.W. Zhang, C. Baumanis, L. Robben, T. Kandiel, D. Bahnemann, Small 7 (2011) 2714–2720.
[197] M. Zhou, J. Bao, Y. Xu, J.J. Zhang, J.F. Xie, M.L. Guan, C.L. Wang, L.Y. Web, Y. Lei, Y. Xie, ACS Nano 8 (2014) 7088–7098.
[198] L.W. Zhang, C.Y. Lin, V.K. Valev, E. Reisner, U. Steiner, J.J. Baumberg, Small 10 (2014) 3970–3978.
[199] Y.X. Liu, H.X. Dai, J.G. Deng, L. Zhang, C.T. Au, Nanoscale 4 (2012) 2317–2325.
[200] K. Ji, H. Dai, J. Deng, H. Zang, H. Arandiyan, S. Xie, H. Yang, Appl. Catal. B: Environ. 168–169 (2015) 274–282.
[201] L. Fang, F. Nan, Y. Yang, D. Cao, Appl. Phys. Lett. 108 (2016) 093902.
[202] F. Nan, Z. Kang, J. Wang, M. Shen, L. Fang, Appl. Phys. Lett. 106 (2015) 153901.
[203] M. Zalfani, B. Van Der Schueren, Z.Y. Hu, J. Rooke, R. Bourguiga, M. Wu, G. Van Tendeloo, Y. Li, B.L. Su, J. Mater. Chem. A 3 (2015) 21244–21256.
[204] M. Zalfani, Z.-Y. Hu, W.-B. Yu, M. Mahdouani, R. Bourguiga, M. Wu, Y. Li, G. Van Tendeloo, Y. Djaoued, B.-L. Su, Appl. Catal. B: Environ. 205 (2017) 121–132.
[205] Y. Wang, H. Dai, J. Deng, Y. Liu, H. Arandiyan, X. Li, B. Gao, S. Xie, Solid State Sci. 24 (2013) 62–70.
[206] K. Ji, J. Deng, H. Zang, J. Han, H. Arandiyan, H. Dai, Appl. Catal. B: Environ. 165 (2015) 285–295.
[207] Y. Wang, H. Dai, J. Deng, Y. Liu, Z. Zhao, X. Li, H. Arandiyan, Chem. Eng. J. 226 (2013) 87–94.
[208] K. Zhang, Y. Liu, J. Deng, S. Xie, H. Lin, X. Zhao, J. Yang, Z. Han, H. Dai, Appl. Catal. B: Environ. 202 (2017) 569–579.
[209] L. Zhang, E. Reisner, J.J. Baumberg, Energy Environ. Sci. 7 (2014) 1402–1408.
[210] H. Zhang, C. Cheng, ACS Energy Lett. 2 (2017) 813–821.
[211] H.F. Zhang, W.W. Zhou, Y.P. Yang, C.W. Cheng, Small 13 (2017) 1603840.
[212] J. Wang, Q. Li, W. Knoll, U. Jonas, J. Am. Chem. Soc. 128 (2006) 15606–15607.
[213] Z. Zheng, K. Gao, Y. Luo, D. Li, Q. Meng, Y. Wang, D. Zhang, J. Am. Chem. Soc. 130 (2008) 9785–9789.
[214] D.-K. Hwang, H. Noh, H. Cao, R.P.H. Chang, Appl. Phys. Lett. 95 (2009) 091101.
[215] R. Kubrin, H.S. Lee, R. Zierold, A.Yu. Petrov, R. Janssen, K. Nielsch, M. Eich, G.A. Schneider, J. Am. Ceram. Soc. 95 (2012) 2226–2235.
[216] H.S. Lee, R.R. Kubrin, A.Y. Zierold, K. Petrov, G.A. Nielsch, M. Schneider, Eich, Opt. Mater. Express 3 (2013) 1007–1101.
[217] R. Kubrin, R.M. Pasquarelli, M. Waleczek, H.S. Lee, R. Zierold, J.J. do Rosário, P.N. Dyachenko, J.M. Montero Moreno, A. Yu, R. Petrov, M. Janssen, K. Eich, G.A. Nielsch, Schneider, Appl. Mater. Interfaces 8 (2016) 10466–10476.
[218] L. Passoni, L. Criante, F. Fumagalli, F. Scotognella, G. Lanzani, F. di Fonzo, ACS Nano 8 (2014) 12167–12174.
[219] H. Dotan, O. Kfir, E. Sharlin, O. Blank, M. Gross, I. Dumchin, G. Ankonina, A. Rothschild, Nat. Mater. 12 (2013) 158–164.
[220] K. Lee, A. Mazare, P. Schmuki, Chem. Rev. 114 (2014) 9385–9454.
[221] Z. Zhang, L. Zhang, M.N. Hedhili, H. Zhang, P. Wang, Nano Lett. 13 (2013) 14–20.
[222] Z. Zhang, H. Wu, Chem. Commun. 50 (2014) 14179–14182.
[223] Z. Li, Y. Xin, Z. Zhang, Nanoscale 7 (2015) 19894–19898.
[224] X. Li, J. Yu, J. Low, Y. Fang, J. Xiao, X. Chen, J. Mater. Chem. A 3 (2015) 2485–2534.
[225] J. Ran, J. Zhang, J. Yu, M. Jaroniec, S.Z. Qiao, Chem. Soc. Rev. 43 (2014) 7787–7812.
[226] B. Ren, Y. Huang, C. Han, M.N. Nadagouda, D.D. Dionysiou, Ferrites as photocatalysts for water splitting and degradation of contaminants in ferrites and ferrates: chemistry and applications in sustainable energy and environmental remediation, ACS Symposium Series vol. 1238, (2016) 79–112 Chapter 3.
[227] S. Dervin, D.D. Dionysiou, S.C. Pillai, Nanoscale 8 (2016) 15115–15131.
[228] M. Rochkind, S. Pasternak, Y. Paz, Molecules 20 (2015) 88–110.